UNIVERSITY OF CALIFORNIA

Santa Barbara

Microscale Characterization of Damage Accumulation in SiC/SiC Minicomposites via a Multi-Modal Approach

A dissertation submitted in partial satisfaction of the

requirements for the degree Doctor of Philosophy

in Materials

by

Bhavana Swaminathan

Committee in charge:

Professor Samantha H. Daly, Co-Chair

Professor Tresa M. Pollock, Co-Chair

Professor Carlos G. Levi

Professor Frank W. Zok

September 2021

The dissertation of Bhavana Swaminathan is approved.

Frank W. Zok

Carlos G. Levi

Tresa M. Pollock, Committee Co-Chair

Samantha H. Daly, Committee Co-Chair

July 2021

Microscale Characterization of Damage Accumulation in SiC/SiC Minicomposites via a Multi-Modal Approach

by

Bhavana Swaminathan

To all my loved ones

Acknowledgements

I thank my advisors, Professors Samantha Daly and Tresa Pollock, for their endless support of my scientific endeavors and professional growth. Sam, I am reminded almost daily how lucky I am to have a mentor who has always supported my dreams, ceaselessly pushed me to be better, and never let me believe in the limits of my own potential. Tresa, you have been a much-needed source of perspective and insight as I carved out a space for myself in this field; I am a better scientist because of you. To my mentors at NASA GRC, Doug Kiser and Dr. Amjad Almansour, I am eternally grateful for your friendship and guidance these past years. You made GRC feel like a home away from home. Thank you to Dr. Kathy Sevener, who has been a constant voice of reason as I developed my understanding of CMCs.

I thank the NASA Space Technology Research Grants Program for funding my studies and giving me unforgettable opportunities to present my research around the world. Thank you to Dr. Wayne Jennings and Pete Bonacuse at NASA GRC for your kindness, camaraderie, and "reconnoitering" during my nights at the SEM. This work would not have been possible without you both.

Thank you to my colleagues for your encouragement, feedback, and help, especially my group-mates Caelin Muir, Abed Musaffar, and Nolan McCarthy, who supported me in all my intellectual pursuits. I will remember graduate school as a time full of laughter and resilience because of you all.

And finally, thank you to my parents, my brother, my grandparents, my family around the globe, and my dearest friends Virginia Collier, Katie Rose, and Caitlynn Weston, who believed in me even when I did not believe in myself. This PhD is for you.

Curriculum Vitæ

Bhavana Swaminathan

Education

2021	Ph.D. in Materials, University of California, Santa Barbara.
2016	B.S. in Materials Science & Engineering, Case Western Reserve University.

Publications

1	**B. Swaminathan**, N. R. McCarthy, A. S. Almansour, K. Sevener, J. D. Kiser, T. M. Pollock, S. Daly, "Microscale Characterization of Damage Accumulation in CMCs." *Journal of the European Ceramic Society* (2020).
2	C. Muir, **B. Swaminathan**, A. S. Almansour, K. Sevener, C. Smith, M. Presby, J. D. Kiser, T. M. Pollock, S. Daly, "Damage Mechanism Identification in Composites via Machine Learning and Acoustic Emission." *npj Computational Materials* (2021)
3	**B. Swaminathan**, N. R. McCarthy, A. S. Almansour, K. Sevener, A. K. Musaffar, J. D. Kiser, T. M. Pollock, S. Daly, "Interpreting Acoustic Energy Emission in SiC/SiC Minicomposites through Modeling of Fracture Surface Areas." *Journal of the European Ceramic Society* (2021).

In Preparation

1	C. Muir, **B. Swaminathan**, K. Fields, A. S. Almansour, K. Sevener, C. Smith, M. Presby, J. D. Kiser, T. M. Pollock, S. Daly, "A Machine Learning Framework for Damage Mechanism Identification from Acoustic Emissions in Unidirectional SiC/SiC Composites." *In Review* (2021)
2	**B. Swaminathan**, A. K. Musaffar, N. R. McCarthy, A. S. Almansour, K. Sevener, J. D. Kiser, T. M. Pollock, S. Daly, "In-SEM Characterization of Crack Opening Displacements in SiC/SiC Minicomposites." *In Preparation* (2021)

Abstract

Microscale Characterization of Damage Accumulation in SiC/SiC Minicomposites via a Multi-Modal Approach

by

Bhavana Swaminathan

The characterization and understanding of damage initiation and evolution in SiC/SiC ceramic matrix composites is critical to improve modeling efforts and design guidelines for these high impact materials. In this dissertation work, microscale damage accumulation was investigated in two systems of SiC/SiC minicomposites of different architectures. A combination of mechanical testing with acoustic emission (AE) inside a scanning electron microscope was used to map surface damage at high spatial resolution and compare it to bulk damage accumulation. This combination of *in situ* damage monitoring enabled the characterization of the evolution of matrix crack density and crack opening displacements and enabled accurate mapping of local damage events to their generated AE. It was found that AE is a strong predictor of transverse matrix crack density, and also likely captures small contributions from secondary mechanisms such as debonding and sliding. The sensitivity of AE was examined using a modeling framework that leveraged simplifications of specimen geometry and assumptions of damage progression to compare point-by-point AE accumulation with estimations of damage accumulation in unidirectional CMCs. This framework resulted in an AE-based estimate of fiber failure evolution that agreed with micromechanics-based predictions when the AE contributions of secondary mechanisms were included. Finally, *in situ* matrix crack opening displacements (CODs) were characterized, and variations within specimens and across minicomposite systems were related to key microstructural and damage accumulation differences. Ex-

perimentally obtained CODs were compared to COD predictions from the literature, and it was found that the accuracy of the model predictions principally depended on consideration of the (i) progressive nature of fiber failure prior to specimen failure; and (ii) variations between the initial crack opening rate (upon matrix crack formation) and the subsequent crack opening rate (upon continued axial loading).

Contents

List of Figures

List of Tables

Chapter 1

Introduction

1.1 Ceramic Matrix Composites

Ceramic matrix composites (CMCs) are high-performance materials wherein a ceramic material matrix is reinforced by another phase (fibers), which may or may not also be ceramic. While there are a multitude of systems that are considered CMCs, this dissertation focuses on a subset of CMCs composed of a silicon carbide (SiC) matrix reinforced by continuous silicon carbide fibers that are coated with a boron nitride (BN) interphase. SiC/SiC CMCs are attractive candidates for extreme environment applications for a number of reasons: they exhibit low weight and porosity (depending on processing conditions), stability and strength at elevated temperatures, advantageous creep and oxidation resistance, high thermal conductivity and relatively low thermal expansion [6, 7]. As a result, SiC/SiC CMCs are increasingly being employed in a range of applications including high-pressure turbine (HPT) shrouds in the hot section of aircraft engines, HPT vanes, combustor liners, and are being considered for fuel cladding in generation IV nuclear reactors [6, 8, 9]. They are also under consideration for use in applications including ground transportation, power generation, and the nuclear sector

[10, 11, 12].

In CMCs, the order in which damage develops leads to a composite of brittle constituents having non-linear deformation and improved toughness over monolithic ceramics. In a monolithic ceramic, a critically sized flaw under sufficient load will initiate a crack that grows unstably through the material, leading to catastrophic failure. In CMCs, however, consecutive cracks can initiate throughout the matrix bulk due to load transfer at the fiber-matrix interface in the vicinity of each matrix crack; this behavior enables stable crack growth until the point at which any remaining intact region of the matrix can no longer reach the critical stresses needed to initiate further cracks. This stage, when the matrix can no longer sufficiently support load, is called matrix crack saturation [13, 1, 14].

The primary driver of the non-linear deformation behavior of SiC/SiC CMCs is the fiber-matrix interface. The interphase coating has an elastic modulus and ultimate tensile strength approximately an order of magnitude lower than the SiC matrix and fiber [15]. A weak and compliant interphase coating facilitates matrix crack deflection at and around fiber surfaces rather than crack propagation through them. This is a result of the lower fracture toughness of the interface relative to that of the fibers [16]. When fibers in the matrix crack wake remain intact and continue bearing load by way of crack deflection, fibers can continue exerting bridging tractions that prevent unstable crack growth. In the vicinity of the matrix crack plane, crack deflection at the fiber-matrix interface leads to debonding along some length of the fibers (i.e. the debond length). Under continued loading, fiber extension results in frictional sliding of fibers against the matrix, which dissipates energy through shear in the debonded region. In conjunction with the ability to form multiple matrix cracks, secondary mechanisms of interfacial debonding and sliding in the vicinity of matrix cracks drive the advantageous toughness behavior characteristic of CMCs. In the scenario that an interface coating is strongly bonded between the fibers

and matrix, the composite material will exhibit similar fracture behavior to that of a monolithic ceramic and fail by way of unstable crack growth.

Though CMCs have been materials of interest for decades, two critical areas that are still not well understood are the influence of the local constituent landscape (which includes factors such as constituent properties and geometry, loading conditions, porosity, processing choices, environmental effects, etc.) on microscale damage mechanisms, and the evolving interactions of these mechanisms up to failure. These microscale events dictate the earliest damage evolution in CMCs and influence final failure behavior [17, 18, 13, 15, 19, 20, 1]. While previous *in situ* observations of CMCs have provided valuable insights about early damage and its evolution [21, 4], the limited fields of view (FOVs) in these studies may not represent damage phenomena across the composite. Experimental characterization of evolving damage phenomena across broader FOVs is needed to clarify the interactions between damage mechanisms and their relationships with the local CMC landscape. In even simple laminate structures [21], the size on which damage accumulates (matrix crack widths of 100s of nanometers [22]) and the FOVs needed to resolve that damage are small relative to the size of the specimen. As such, capturing large regions of the specimen as damage accumulates can range from time-consuming to infeasible.

As an alternative for studying damage behavior in CMCs, minicomposites are utilized in this work. These specimens are idealized, unidirectional elements of CMCs, as shown in via computed tomography (CT) in Figure 1.1. Minicomposites have well-suited, simplified architectures that enable the evaluation of a few fundamental damage mechanisms (i.e. matrix cracking, fiber bridging, and fiber breakage). Previous studies have used SiC/SiC minicomposites with continuous fiber reinforcement to examine and characterize the initiation and evolution of damage in CMCs [5, 23, 4, 24, 25], as they exhibit analogous stress-strain behaviors to macrocomposites. Almansour et al. [5] related the experimental matrix cracking strength of minicomposites to well-established models

[26, 27] in order to predict the stress on the matrix at the onset of matrix cracking. Chateau et al. [4] captured microscale damage progression in minicomposites using CT measurements and tensile testing in-SEM (scanning electron microscope), to develop and validate a 1D probabilistic model of damage evolution based on matrix and fiber failure probability laws. Maillet et al. [23] clustered various minicomposite damage modes using multivariate analysis of acoustic emission information produced during tensile and cyclic loading. Such studies have shown that the experimental damage behavior of minicomposites can be directly compared to micromechanical models [26, 27, 28, 17, 14] and have validated their continued use for the characterization of damage evolution in CMCs. The remainder of this chapter summarizes existing micromechanical models, testing methods for small-scale damage characterization, and analytical approaches for studying damage evolution *in situ*. Outstanding questions in the field that are explored herein are highlighted.

1.2 Micromechanical Models

Modeling the damage chronology in unidirectional CMCs has been the subject of extensive study. These models typically consider a fundamental damage chronology in which matrix cracking is followed by toughening phenomena at interfaces, leading to fiber and composite failure; these studies have shed considerable light on the micromechanics of damage accumulation [19, 27, 1, 18, 17].

However, due to complex and interacting factors of the CMC constituent landscape (microstructure, processing choices, constituent properties, and more), many studies use simplifying assumptions about the CMC and the damage accumulation within it to predict the material response. For example, the widely-used ACK model [26] assumed a fully debonded interface to relate matrix crack spacing to both the stress at the onset of

matrix cracking and the interfacial shear strength. The ACK model was later expanded by Budiansky et al. [27] to include an initially weak bond at the fiber-matrix interface. This work relied on the assumptions of initially bonded, debonding fibers *or* frictionally constrained, sliding fibers; however, it is well-established that debonding and sliding occur concurrently [29, 30]. In another approach, Lamon et al. [18] modeled the ultimate strength of CMCs using Weibull statistics to characterize multiple matrix cracking as a function of the matrix fragment length and fiber bundle failure. The model assumed that once broken, fibers no longer participate in load bearing. However, Chateau et al. [4] showed via *in situ* x-ray microtomography (XCT) that fibers can continue bearing load after an initial break, instead breaking several times along their length through fiber sliding and bridging. Since these foundational studies, improvements in predictive modeling using micromechanical considerations [31, 32, 33, 25, 34, 35, 36, 24] have mandated an analysis of constituent landscape effects on damage evolution. Continued progress in modeling CMCs, therefore, relies on statistically-significant experimental insights on how damage accumulates in these high impact materials, of which there has been limited reported data [34, 22, 25]. A key objective of the investigations described in this dissertation is to characterize *in situ* damage evolution in minicomposites as a function stress to evaluate the efficacy of well-established micromechanical models for capturing the experimentally-observed damage behavior.

1.3 Acoustic Emission for Damage Characterization

Non-destructive structural health monitoring techniques are well-suited for the experimental characterization of damage accumulation in CMCs. While many approaches have been employed, including electrical resistance measurements, ultrasonic testing, and radiography [37, 38, 23, 39, 40], this dissertation focuses on the use of acoustic emission

(AE) due to its widespread use and suitability for CMCs.

When damage occurs in CMCs, rapidly accumulated strain energy is released, generating elastic waves that propagate into the surround medium. The analysis of these waves as AE is a well-established approach for evaluating damage in SiC/SiC CMCs and can be used to locate event sources and characterize damage in the bulk [5, 23, 41, 42, 43, 44, 45, 46, 47, 48, 34]. It has been shown that the cumulative energy of acoustic emission is a good predictor of the transverse matrix crack density evolution [49, 5], and that concentrated regions of AE events correlate with final failure locations in CMCs [48]. AE has been captured for CMC structures ranging from simple, unidirectional geometries [5, 23], to laminates [34], fabrics [50], and braids [51]. Successful capture of AE activity in more complex geometric structures primarily requires an appropriate number of AE sensors for the geometry of interest and their placement sufficiently close to damage sources.

Previous efforts have used AE to quantify matrix cracking and other damage mechanisms in relation to time, stress, and environment in a suite of CMC materials and structures. Morscher et al. showed that acoustic emission activity can occur well below the material proportional limit (PL) [41]. This finding leads to the possibility that acoustic emission correlates with some variation of threshold stress, below which the strain accumulation can be attributed to noise, but above which something measurable exists. Though researchers have demonstrated such instances of early AE for decades [52, 53, 54], these signals were either disregarded as potential noise or only hypothesized to correspond to matrix microcracking; rather, *in situ* observations of early microscale damage accumulation in CMCs are relatively recent [21].

In combination with modern computing, the potential of AE to identify damage mechanisms in composites, by correlating damage sources to specific features of their AE signals (waveform characteristics, frequency spectra, etc.) has been recently explored [23, 42, 55, 56, 57]. Maillet et al. [42] used the frequency centroids (weighted average of

the frequency spectra) of AE events to locate transverse matrix cracks in the thickness of multi-layer composites and subsequently grouped signals related to surface and interior cracking. Their work concluded that if every AE event is projected in terms of frequency content and distance with high accuracy, a range of frequency spectra associated with a damage mode can be identified that takes into consideration the effects of waveform attenuation. In a different study [23], Maillet et al. used wavelet packet decomposition to extract relevant features from AE waveforms and employed subsequent unsupervised clustering to discriminate what they hypothesized to be the SiC cracking (including both the matrix and fiber cracking) and the interfacial phenomena. Continued and future investigations in the area of damage-mechanism identification by AE are described in Chapter 5 and explored in recent investigations by Muir et al. [58, 59, 60], which are co-authored by the author of this dissertation.

Establishing correspondence between AE signals and damage mechanisms would have significant ramifications for structural health monitoring under operating conditions of interest. It would allow for the non-destructive, *in situ* identification of damage sources, enable researchers to bypass expensive high-resolution methods (such as SEM and XCT [61, 62, 34]), and produce information-rich datasets for large-scale statistical analyses of the effects of small-scale damage in full composite structures.

1.4 in-SEM Measurements of Damage Evolution

Scanning Electron Microscopy (SEM) has become an increasingly popular method for studying *in situ* damage evolution in CMCs. Initially for CMCs, SEM observations were limited to postmortem analysis, which was reliable for quantifying mechanistic information such as fiber pull-out lengths and matrix crack density near the rupture zone [52, 63, 46, 64]. In more recent years, *in situ* testing wherein CMC specimens are deformed

using mechanical testing rigs installed within SEMs, provides high-resolution insights on damage initiation and accumulation at the material surface. In-SEM mechanical testing has been previously used [22, 21, 65, 31] in conjunction with digital image correlation (DIC), which enables full-field deformation measurement across multiple length scales. Tracy et al. [21, 65] investigated crack initiation both at the constituent and laminate length scales at ambient and elevated temperatures by SEM-DIC. Sevener et al. [22] characterized the *in situ* crack opening displacement in laminate SiC/SiC CMCs using SEM-DIC. For such experiments, interrupted loading has been compulsory at the microscale due to the raster-scan nature of microscopy, which prevents real-time capture of crack propagation. As a result, macroscale DIC using high-speed cameras or high-resolution videography has also been utilized to capture dynamic crack propagation [48], in order to leverage insights from SEM-DIC experiments.

1.5 Objectives and Dissertation Outline

In this dissertation, a multi-modal approach of in-SEM mechanical testing of SiC/SiC minicomposites for the high-resolution capture of surface damage accumulation is combined with AE measurements for real-time monitoring of damage evolution in the material bulk. These investigations focus on the quantitative characterization of damage initiation and propagation in two systems of SiC/SiC minicomposites, involving experimental and analytical investigation of damage across lengths scales. Testing protocols for SEM-AE approaches and analysis methods to obtain high-fidelity experimental information were developed.

Chapter 2-4 focus on methods for characterizing and modeling damage initiation and progression in SiC/SiC CMCs. Chapter 2 discusses the insights gained from combining bulk AE measurements with in-SEM tensile testing. A method for correlating cracks

tracked *in situ* and the corresponding AE they generate is developed and used to assess the variations in the manner of damage accumulation across specimens of two systems of SiC/SiC minicomposites.

In Chapter 3, point-by-point AE information is investigated using assumptions of damage accumulation in SiC/SiC CMCs. The use of AE data is typically limited to analysis of global damage accumulation trends. Here, the possibility that any one *real*, in-gage AE event provides insight into the damage mechanism which produced it is explored. It is hypothesized that four damage mechanisms are predominantly responsible for generating AE in minicomposites: matrix cracking, interfacial debonding, sliding, and fiber breakage (shown schematically in Figure 1.2. Through a modeling effort combining geometric simplifications of minicomposites with assumptions of how damage progresses, the accumulated AE is related to the modeled creation of new surfaces from damage; by this approach, the size of the damage source which generated each AE event is estimated. This model also includes the fiber break evolution as predicted from AE, and compare these findings with estimates of the total number of fiber breaks at rupture given by [3].

Chapter 4 combines experimental measurements of damage progression with relevant modeling from the literature. In this chapter, crack opening displacements (CODs) across a large quantity of cracks at multiple load states are characterized in two systems of SiC/SiC minicomposites. There are limited *in situ* measurements of the COD in CMCs [22]. An image processing algorithm is developed to precisely measure the COD at hundreds of locations across the crack length, and group COD data at the same crack observed across multiple load states. The experimental measurements of COD are compared with modeling predictions from Marshall et al. [66, 1], which expands our understanding of how well available models reflect the observed damage behavior.

Finally, conclusions and broader impacts of this research, as well as recommendations for future investigations are presented in Chapter 5.

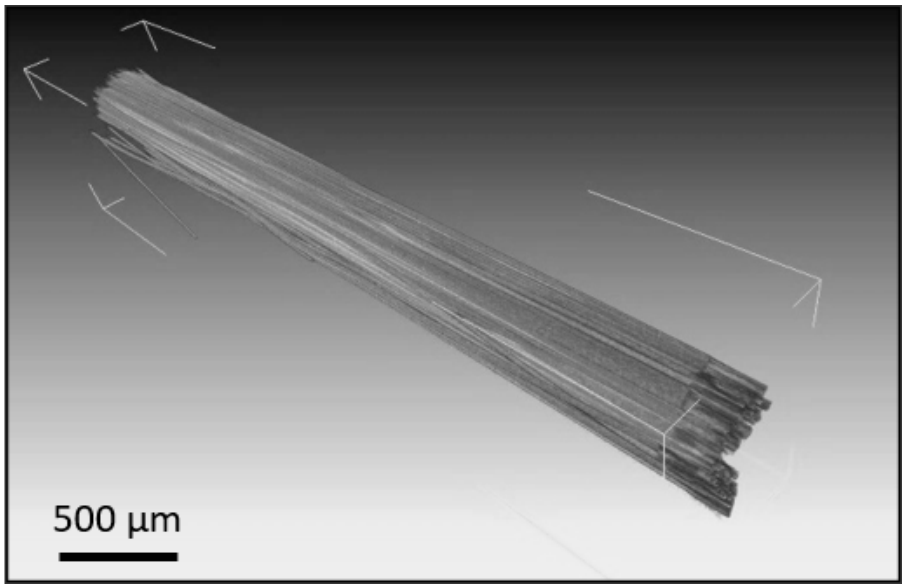

Figure 1.1: Region of the SiC/SiC minicomposite gauge captured via CT. Courtesy of Richard Rauser at GRC.

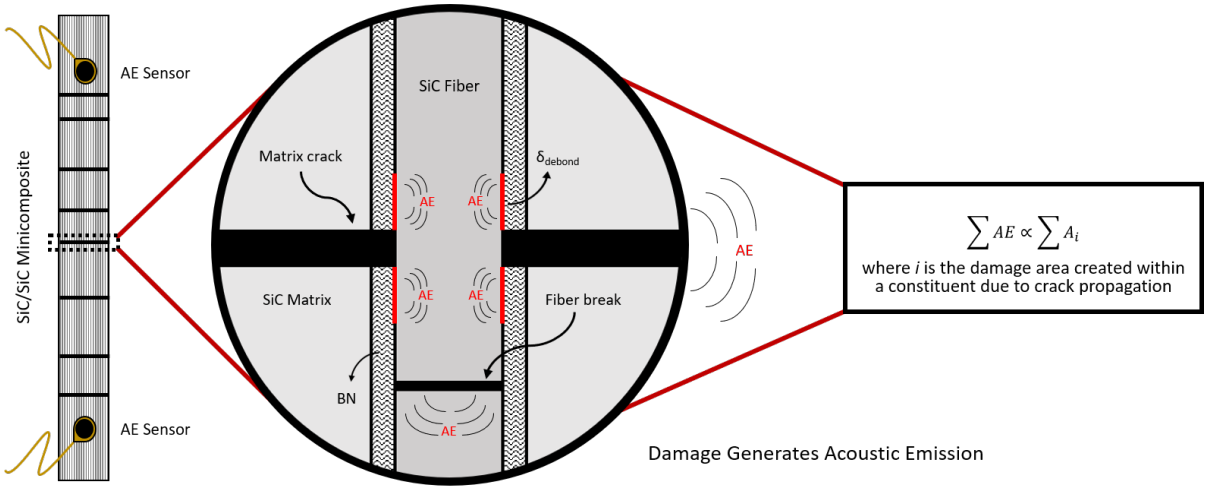

Figure 1.2: It is hypothesized that four damage mechanisms are responsible for the production of AE: matrix cracking, interfacial debonding, fiber sliding, and fiber breakage, where the AE produced by each instance of damage formation is related to the area created by that active mechanism. Therefore, the total AE produced by the specimen is related to the total area created by all occurrences of damage.

Chapter 2

Microscale Characterization of Damage Accumulation in SiC/SiC Minicomposites

2.1 Scope

In this chapter, a multi-modal approach combining in-SEM tensile testing for high-resolution surface analysis with AE measurements for bulk damage analysis was used to characterize early damage initiation and its evolution to failure in SiC/SiC minicomposites. Surface damage was captured at incremental loads via in-SEM imaging, and AE was continuously monitored throughout loading. An alignment scheme was developed to correlate SEM-observed surface damage with corresponding AE events to a high spatial resolution ($\pm$100 µm of cracks). AE events were divided based on their contribution to failure as either: (i) high-energy AE, presumed to be the result of dominant damage mechanisms (e.g. matrix cracking and fiber breakage); and (ii) low-energy AE, presumed to be the result of non-dominant damage mechanisms (e.g. interfacial debonding and

sliding) or small dominant damage mechanisms [54, 67]. While fiber sliding and pullout were active at all crack locations (as a result of fiber elastic deformation and bridging), these non-dominant mechanisms likely accounted for only a small number of the AE events generated in these minicomposites. This was because they likely produced waveforms that had both low energies and low frequencies, which made them difficult to discern independently by the experimental configuration [68, 69, 70].

AE-generating mechanisms were correlated to the failure response. This included investigating how damage (for example, spatially distributed matrix cracks) evolved with respect to architectural features, through observations and analyses of the relationships between AE signals attributed to each damage event and their proximity to the failure location. Building on previous studies, which have either relied exclusively on AE waveform characteristics or statistical tools to determine damage mechanisms [42, 71, 72], this chapter lays a foundation for characterizing surface damage accumulation in CMCs at a high spatial resolution (with the validation of *in situ* monitoring) with a simultaneous framework to analyze point-by-point AE information, which is discussed further in Chapter 5. The fundamental characterization of microscale damage described in this chapter is a building block towards a comprehensive understanding of the relationships between microstructure and damage.

2.2 Methods

2.2.1 Materials

SiC/SiC minicomposite specimens were manufactured by Rolls-Royce High Temperature Composites (Cypress, CA). These specimens consisted of a single tow of 500 Hi-Nicalon Type S^{TM} (HNS) (Nippon Carbon, Tokyo, Japan) SiC fibers, coated with a

chemical vapor infiltrated (CVI) boron nitride (BN) interphase and an overlayer of CVI SiC matrix. Fiber (V_f), interphase (V_i), and matrix volume fractions (V_m) were determined for each specimen and were used to calculate the nominal cross-sectional area of each specimen following a procedure developed by Almansour et al. [5], in which the nominal fiber, interphase, and matrix densities (3.1 g/cm^3, 1.5 g/cm^3, and 3.2 g/cm^3, respectively) were utilized.

Two minicomposite systems were studied and are referred to in this dissertation as high fiber content (HFC) and low fiber content (LFC) (shown in Figure 2.1). HFC specimens had BN interphase thickness of 1.9 µm ± 0.6 µm (determined via image analysis) and fiber loading of 34.1% ± 1.3% (estimated via [5]). LFC specimens had a thicker overlayer of SiC matrix, interphase thicknesses of 0.30 µm ± 0.08 µm, and fiber loading of 22.8% ± 1.0%. Cross-sectional areas of HFC specimens measured ≈34% less than LFC specimens. Constituent volume fractions of four HFC and LFC specimens are provided in Table 2.1. As observed in Figure 2.1b, LFC minicomposites had a characteristically compact fiber tow wrapped in a continuous overlayer of SiC matrix. In contrast, HFC minicomposites were less uniform; the fiber distribution was more heterogeneous with lower matrix volume content around and within the tow (shown in Figure 2.1a). As described in greater detail in Section 2.3.2, the HFC minicomposite configuration can be thought of as a series of parallel microcomposites, where pillars of densely-packed fibers are bonded along the specimen length by limited matrix content. The effects of these microstructural characteristics are explored in Chapter 4.

As further discussed in Sections 2.3.1-2.3.3, characterizing the damage progression and resultant AE in two minicomposite systems with constituent variations enabled a comparison of the observed damage response to known differences in microstructure. Certain insights were made possible by comparing a standard CMC system (LFC SiC/SiC minicomposites) to a non-standard CMC system (HFC SiC/SiC minicomposites). The

absolute effect of the interphase content (V_i) on the mechanical behavior of LFC and HFC SiC/SiC minicomposites could not be determined as the fiber and matrix volume fraction also vary in the two minicomposite systems, however, this is a subject of future investigations described in Chapter 5.

2.2.2 Fiber Push-in Testing

Fiber push-in tests were performed on mounted and polished LFC and HFC specimens using an iMicro Nanoindenter (Nanomechanics, Inc., Oak Ridge, TN). SiC/SiC minicomposites were mounted in epoxy that was subjected to an overpressure of 7.6 MPa. The cross-sections of the minicomposites were polished down to a 0.5 µm diamond finish. In each fiber push-in, the sphero-conical indenter contacted a single fiber. The debond toughness (Γ) and sliding stress (interfacial shear stress) τ for the HFC and LFC systems were determined (Table 2.2) following a procedure developed by [73], which modified the established fiber push-in test of Marshall et al. [74]. The approach detailed in [73] induced only fiber elastic deformation by use of a blunt indenter and utilized quantified hysteresis loop widths for analysis of interfacial properties rather than absolute displacements. The use of this approach to calculate interfacial parameters in SiC/SiC minicomposites has been extensively described by Callaway et al. [75]. Standard deviation values are also provided in Table 2.2. Between 40-50 fibers were indented in each specimen, accounting for 8-10% of the fibers in the tow in the estimation of these interfacial parameters.

For the LFC system, the determined interfacial values were in good agreement with prior reported values [46, 75, 76]. An average LFC Γ of 1.2 $\pm$ 0.5 J/m^2 was calculated. The measured interfacial properties and BN thickness in the LFC system reflected the interfacial conditions of standard macrocomposites [77] In the HFC system, a bimodal

distribution for Γ was initially found with: $\Gamma < 0.05$ J/m^2 or $\Gamma \geq 1.5$ J/m^2. The negligible Γ values observed at some fiber locations in HFC specimens were attributed to either: (i) partial debonding of fibers prior to push-in resulting from either processing (given the low matrix content) or the polishing process that subsequently debonded with little resistance, or (ii) the propagation of debond cracks to nearby fibers during push-in testing, which were then already partially debonded when subsequently tested. Dark interfacial regions were observed in the HFC cross-section prior to push-in testing (shown in Figure 2.2a), likely indicating pre-existing longitudinal cracking. While these cracks potentially formed as a result of thermal residual stresses from either processing or the mounting and polishing procedure, this observation indicated how readily such cracking could occur under tensile loading conditions. In untested areas of the cross-section (imaged post fiber push-in testing), longitudinal crack formation along the fiber length was evident as networks of partially debonded fibers from cracking along the fiber-BN interface (on the order of tens of fibers) (Figure 2.2b). The lower end of the HFC Γ distribution was attributed to these fibers. This extended debond cracking was not an issue in the LFC system, where the debond cracks from fiber push-in were limited to the immediate vicinity of tested fibers as a result of a compliant BN interphase. Thus, only the debond toughness of isolated, initially fully bonded fibers in HFC specimens were considered in the computation of Γ listed in Table 2.2, which gave an average Γ of 5.5 $\pm$ 3.9 J/m^2 based on 20 measurements.

The fiber sliding mechanism acted independently of the debond condition, whether the fiber was bonded to its interphase or not. The average interfacial sliding stress (τ) was higher for fibers tested in HFC specimens (34.5 $\pm$ 13.0 MPa) compared to LFC specimens (18.1 $\pm$ 4.8 MPa).

2.2.3 in-SEM Tensile Testing

Tensile testing was performed at room temperature in-SEM (MAIA3, Tescan, Kohoutovice, Czech Republic) using an *in situ* DDS-3 controlled tensile stage (Kammrath Weiss, Dortmund, Germany) with a 500 N load cell. The ends of 45-50 mm long minicomposites were mounted using 12 mm × 10 mm aluminum tabs with a centerline groove for aligning the sample. They were secured using a high temperature epoxy-resin system (Duralco 133 two-part epoxy and resin) and cured at 121^{o}C ± 2^{o}C for 4 hours. The tabbed specimens were clamped into custom gripping fixtures (Kammrath & Weiss MSZ-3 grips) that then interfaced with the tensile stage. The in-SEM experimental setup is shown in Figure 2.3. Global stresses were determined by dividing the applied loads by the calculated cross-sectional area. The crosshead displacement of the tensile stage was compliance-corrected using a titanium bar of similar geometry and known properties, which exhibited only elastic behavior for loads exceeding those tolerated by the SiC/SiC minicomposites.

Minicomposites were incrementally loaded and imaged at load holds until failure in order to capture damage initiation and progression. The sample was first imaged in the unloaded state (0 N); it was subsequently loaded until AE activity was first captured, and afterward in 20 N increments until specimen failure (this was equivalent to approximately 75-90 MPa increments in LFC specimens and approximately 110-130 MPa increments in HFC specimens). Samples were loaded under a globally-applied uniaxial displacement rate of 2 µm/second, corresponding to a strain rate of 6.7×10^{-5} - 8×10^{-5} s^{-1} for gage lengths ranging from 25-30 mm. SEM images were captured at 8-10 loading increments, depending on the failure load. Each panoramic image captured the sensor-to-sensor sample gage of approximately 15-20 mm. The results of this process are depicted in Figure 2.4. Stress relaxation, resulting in load drop, was observed at load holds above

the proportional limit (PL), which was approximately 250 MPa in the LFC system and 400 MPa in the HFC system. Initially, this relaxation resulted in small load drops on the order of 1-2 N, but at higher load state, load drops on the order of 3-5 N were observed. AE events were occasionally detected during load holds; therefore, the sample was only imaged after a lack of AE activity and load stabilization was observed over the span of a few minutes.

SEM micrographs with 1:1 aspect ratios were captured using an accelerating voltage of 5 kV at a working distance of nominally 17 mm. Image size was maintained at either 8192 × 8192 pixels or 4096 × 4096 pixels, depending on time availability on microscopy equipment, while magnification and field of view (FOV) were varied to accommodate variations in the specimen width. Panoramas of the gage were generated with a 12% overlap between FOVs, using the Image Snapper correlated stitching feature of the SEM. The resolution limit was approximately 150-200 nm/pixel, depending on the FOV (micrograph axis length 1200-1500 µm).

2.2.4 Acoustic Emission

AE was captured in-SEM during specimen loading using a four-channel fracture wave detector acquisition system (Digital Wave Corporation, Centennial, CO). AE waveforms were recorded using two miniature S9225 piezoelectric AE transducers (Physical Acoustics, Princeton, NJ) with 300-1800 kHz sensitivity, that were coupled to the minicomposite surface using Dow Corning high vacuum grease; a medium which links the AE transducer surface to the specimen surface is required for waveform preservation [78]. Each sensor was connected to a custom-built electrical feed-through flange on the SEM chamber, through which signals were transmitted to the Digital Wave system. Commercial software from Digital Wave Corporation was used to analyze the recorded waveforms.

Each AE signal was recorded at a sampling rate of 10 MHz with a pre-trigger length (the time length preceding the AE signal hit) of 256 data points (corresponding to ≈25 µs) (recorded before the first threshold crossing) and an overall length of 1024 data points (corresponding to 102.4 µs). Setting an adequate pre-trigger was critical. It was shown that early elements of the signal can be clipped when sensors are synchronized if there is no set pre-trigger [46]. In comparison, the length of an AE event signal is only on the order of several hundred microseconds and is typically contained in its entirety within the single waveform.

AE events were filtered by a 2-sensor location analysis approach to constrain AE activity to the SEM-captured specimen gage (and the length between the two AE sensors). The location of each event was determined as [46]:

$$\text{location} = \frac{x}{2}\left(\frac{\Delta t}{\Delta t_x}\right) \tag{2.1}$$

where x was the distance between the two sensors, Δt was the difference in the arrival times of waveforms at each sensor, and Δt_x was the maximum difference in arrival times determined from AE events that occurred outside the sensors. The Δt_x parameter took into account the decreasing wave speed through the material as damage was accumulated and the specimen cross-section was degraded [79]. This enabled normalization for waveforms emitted from damage sources at approximately the same location, wherein the waveforms emitted by the later-occurring source had larger differences in arrival times. The arrival times for two waveforms emanating from the same damage source in a 2-sensor configuration are shown schematically in Figure 2.5.

The location analysis method of Eqn. 2.1 has been used extensively in macroscale AE studies of damage accumulation [67, 41, 57, 49]. However, the spatial inaccuracy when mapping AE events to local damage using this approach can be ± 1 mm [41]. One

contributor to this error is the use of a threshold voltage, where a minimum voltage is set to define the generation of a real AE event (interpret signal arrival time). If this voltage is set too low, the arrival time determined may be within the pre-trigger noise regime; if set too high, the onset of the real signal may be missed. Misinterpreting the arrival time of a signal (on the order of a few µs) can skew the location of that AE event by several millimeters.

For these experiments, each parameter for location analysis (Eq. 2.1) was measured to a high resolution. The sensor separation distance (x) was measured to a sub-millimeter resolution in-SEM; this is an improvement to the separation distance measured in *ex situ* testing, which is often to the nearest millimeter resolution. The difference in waveform arrival times for each event (Δt) was measured by manually determining the first peak of the extensional wave. As a note, there are other methods that are also more accurate than the threshold voltage method for measuring waveform arrival times, such as the Akaike Information Criterion (AIC) approach described in [42]. The initial maximum difference in arrival times (Δt_x) was measured by using Hsu-Nielsen sources [80] (i.e. lead breaks) to determine the transmission time across the AE window (from sensor to sensor) in the unloaded, and presumably undamaged, state. As the sample was loaded, matrix crack formation and fiber breaks degraded the specimen cross-section, decreasing the acoustic waveform velocity and increasing the transmission time for waveforms to reach the sensors. Therefore, as the sample was loaded, AE events generated outside of the AE window were selected to determine the maximum difference in arrival times as a function of the stress. Waveforms generated within the AE window were similarly impacted by specimen degradation, so a reliable measure of the maximum waveform propagation time across the AE window was needed to triangulate AE events accurately.

To minimize for the effects of energy attenuation, signal energies from both sensors of a single event were averaged and considered to be the energy of that AE event [41].

For AE energy characterization, each average AE event energy was normalized by the maximum average AE event energy for that specimen. This normalization was performed in order to compare specimens within and between each minicomposite system. AE event energies were calculated and provided by the Digital Waveform software, where the energy was considered to be the area under the curve of waveform amplitude (V) as a function of time (µs) [81]. Waveform event energy was also considered to be proportional to the square of the waveform amplitude [82].

The AE-estimated crack density evolution (CDE) was determined by multiplying the rupture state crack density ($CD_{rupture}$) by the normalized energy accumulation (as a function of event number) up to matrix crack saturation [49]:

$$CDE(N) = CD_{rupture} \times \frac{Cumulative\ AE\ (N)}{Cumulative\ AE\ at\ crack\ saturation} \tag{2.2}$$

where N was the event number, and *CDE(N)* was the predicted transverse matrix crack density at that event. Eq. 2.2 enabled estimation of the number of cracks/mm that had formed up to the point when a particular AE event (N) was recorded. AE signals generated beyond crack saturation were not taken into consideration in the AE-estimated CDE, as they were presumed to be the result of fiber-dominated damage. As further described in Section 2.3.3, the state of matrix crack saturation was estimated by a decrease or plateau in AE activity (shown in Figure 2.6). This was experimentally verified by the typically static population of surface matrix cracks observed in-SEM at stress beyond matrix crack saturation. The experimental CDE was calculated by counting the through-width cracks in panoramic micrographs from each loading increment and dividing by the total number of cracks in the imaged sample length near rupture. As further described in Section 2.3.3, the AE-estimated CDE was in good agreement with the *in situ* measured matrix crack density.

2.2.5 Correlated AE Response and in-SEM Damage Evolution

The accurate correlation of in-SEM surface damage with its corresponding AE activity was critical for: (i) tracking the relative AE activity of transverse matrix cracks along the sample gage up to failure; and (ii) characterizing the relationships between the local evolution of damage and the underlying mechanisms responsible. An alignment protocol (depicted schematically in Figure 2.7) was developed that significantly improved the alignment of surface damage observed in-SEM with global AE (the total AE accumulated by the specimen during loading up to some stress) data to $\pm$ 0.10 mm, and showed the sensitivity of AE for capturing small-scale and early damage phenomena, as further described in Section 2.3.1.

The need for this alignment scheme stemmed from image distortions caused by the vacuum grease charging. The vacuum grease served as a needed coupling agent between AE transducers and the specimen, but limited imaging of the full sensor-to-sensor gage in-SEM due to charging. The positions of the top and bottom edges of this reduced window were unknown relative to the sensors. As described below, the developed alignment scheme shifted the in-SEM maps to their absolute positions in order to directly correlate observed surface damage in-SEM with the corresponding AE events.

In Figure 2.7, the AE generated by a minicomposite under load was mapped to the observed surface damage accumulation using the developed alignment scheme. On the left in each subfigure, the sample and sensor orientation are shown (vacuum grease is shown as the circles around each sensor). On the region of the minicomposite surface that could be imaged, a series of SEM micrographs were taken, forming a panoramic image of the surface (depicted in Figure 2.7a); this can be thought of as the sample reference frame. On the right in each subfigure, the AE generated up to the current globally-applied stress of the specimen was mapped for the full sensor-to-sensor distance;

this can be thought of as the AE reference frame. In Figures 2.7a and 2.7b the stress on the sample was the same, and in Figures 2.7c and 2.7d, the sample was loaded further, generating additional damage and producing more AE. The alignment scheme proceeded as follows:

- **STEP 1**: AE events were located to a high spatial resolution following the measurement protocol detailed in Section 2.2.4.
- **STEP 2**: The SEM-mapped damage was correlated to its corresponding AE. In Figure 2.7a, surface cracks were initiated and/or propagated during loading to σ_1. While the sample was held at that load, a panoramic micrograph of the gage was created, documenting the damage present on the top surface of the minicomposite. The spatial distribution of this early, visible damage measured on the sample reference frame was correlated to the equivalent positional spacing of AE events that had been detected during the initial loading, in order to shift the sample reference frame to its absolute position relative to the AE reference frame and align the two (Figures 2.7a and 2.7b).
- **STEP 3**: This alignment was validated at each loading increment up to failure as follows: AE activity generated between two loading increments was used to map both the formation of new, observable surface damage and to track activity in the vicinity of existing cracks (Figures 2.7c and 2.7d).

While all accumulated surface damage within the reference frame of interest could be directly mapped to AE activity, it was not uncommon at early stresses to detect AE activity that could not be directly mapped to damage observed in-SEM. In such instances, it was assumed that either (i) this AE was generated by damage initiating subsurface or on the opposite specimen surface, or (ii) such damage, if occurring the surface, formed

below the imaging resolution of the micrographs. In either case, at higher loads, surface damage was observed in these AE-generating regions. In addition, the formation of short, thin matrix cracks near the specimen ends often could not be detected in AE. It is likely that the emitted signals produced by these cracks, which did not propagate or open under continued loading, fell below the sensitivity of the experimental configuration used here; furthermore, failure never occurred at these axial position. It is possible that a more sensitive AE configuration may be able to capture such events.

2.3 Results Discussion

2.3.1 Early Cracking Behavior

In earlier investigations, AE activity was readily captured below the material PL in SiC/SiC CMCs [49, 41], as well as in both systems of minicomposites studied in this dissertation (shown in Figure 2.8). In these studies, excellent agreement was found between the minicomposite PL and the globally-applied stress when the first "loud" AE event occurred, which corresponded to the first recorded event within the specimen gage with an event energy among the highest order magnitude of all recorded events for that specimen [5]. Given the correlation between the first "loud" AE event and the PL, it was assumed that such AE events also indicated the onset of major cracking in the material [53]. This measure of the AE-estimated PL was employed herein. Given the low energy of AE events that were captured below the material PL, these events were often historically disregarded as non-significant.

Through the multi-modal approach used in this dissertation, early AE activity was mapped to the earliest microscale surface damage (shown in Figure 2.9). Microcracking that occurred at stresses below the PL was assumed to be due to the propagation of

preexisting flaws. Small surface cracks, such as those shown in the unloaded state in Figure 2.9, were observed in some samples prior to loading and propagated at low stresses. In general, early AE events were low-energy (below 10% of the maximum energy event for a given specimen). When these microcracks first propagated, they were typically arrested; rarely did such cracking traverse the horizontal specimen dimension at these low stresses. This indicated that early damage was limited to partial cracking of the transverse plane.

2.3.2 Global Damage Response

For the purpose of this discussion, the CMC damage chronology was considered in terms of two domains: Domain I, dominated by matrix cracking, and Domain II, dominated by fiber failure. The transition between these domains occurred at the matrix crack saturation, which was approximately 600-650 MPa for the LFC system and 800-850 MPa for the HFC system, where there was a lull or plateau in the AE energy accumulation curve, as fibers were being elastically strained (Figure 2.6). In Domain I, the AE energy release rate initially increased when significant matrix cracking occurred. This rate remained steady through the matrix-dominated regime and tapered at matrix crack saturation. Beyond matrix crack saturation, the AE energy release rate again increased as fibers broke. From the onset of AE generation up to specimen failure, nearly twice the number of AE events were produced in similarly sized HFC specimens compared to LFC specimens. The majority of this difference in AE occurred within the matrix-dominated regime, as is shown in Figure 2.10.

Prior to matrix crack saturation, matrix crack initiation and propagation, interfacial debonding and fiber sliding, and some quantity of early fiber failures [62] were all responsible for the generation of AE activity. In the HFC system, the greater number

of AE events detected before matrix crack saturation was attributed to its lower matrix content, which led to the presence of pseudo-discrete pillars of smaller, closely spaced sub-minicomposites that effectively acted as microcomposites (shown in Figure 2.1a). The presence of these microcomposite pillars obstructed through-thickness, continuous cracking. As a result, matrix crack propagation likely occurred in increments across pillars as a function of the globally-applied stress. It is possible that when matrix cracks propagated through a minicomposite but lacked a subsequent in-plane matrix pathway to propagate through the cross-section, these cracks then deflected and propagated along the fiber length until a new matrix pathway emerged. In general, load transfer to other regions of the minicomposite due to the initiation of a crack likely occurred out of plane of the original matrix crack. Such discontinuous cracking was observed in-SEM (Figure 2.12a). In HFC specimens, each crack propagation step likely resulted in a distinct AE event. In contrast, the higher CVI SiC matrix content in the LFC system provided a more continuous matrix pathway for cracking. As observed in Figure 2.12b, when the CMC cross-section was connected by a coherent matrix network, a single crack could readily initiate and propagate through-thickness. In the LFC system, this through-plane matrix network for cracking was responsible for the generation of fewer AE events associated with matrix crack propagation.

Beyond matrix crack saturation, AE was predominantly generated by the dominant mechanism of fiber failure (though the contribution of other damage mechanisms beyond matrix crack saturation are investigated in Chapter 3). Both minicomposite systems shared fiber characteristics (the same fiber tow was used to fabricate samples), but the distribution of fibers was more heterogeneous in the HFC versus the LFC system (as shown in Figure 2.1). While the initial mechanism of fiber breaks was likely the same between systems (i.e. fibers were strained elastically in the vicinity of a matrix crack until they broke based on a Weibull distribution [83, 84]), the subsequent response varied. In

HFC specimens, the fiber-dominated regime up to failure took place at higher globally-applied stresses (from approximately 850-1150 MPa), whereas this regime occurred in LFC specimens from approximately 650-850 MPa. In part, this was an effect of the higher fiber content of the HFC system, which was in agreement with previous findings by Almansour et al. [5]. However, the fiber tow distribution may have also played a role. In LFC systems where fibers were more closely packed, the stress profile in each fiber under a globally-applied stress was likely more similar; here, where a compliant BN interface promoted effective load transfer, the impact of a fiber break would shed load to all fibers in the cross-section, with subsequent fiber breaks following the initial ones. In contrast, the individual pillars in the HFC system likely experienced unique stress profiles under the same globally-applied stresses throughout loading, as further evidenced by the staggered propagation of transverse matrix cracking (Figure 2.12a). In the HFC system, fiber breaks likely locally shed load (in-plane) within the microcomposite where the initial break occurred. It is possible that there was a weaker effect of the initial fiber break on the HFC system's continued ability to bear load compared to the LFC system. As a result, the range in stresses over which fiber breaks occurred (i.e. the stresses the specimen withstood beyond matrix crack saturation) was larger in HFC specimens, as shown in Figure 2.13.

The improved correlation of AE with in-SEM observed microscale damage was used to analyze AE activity in the vicinity of spatially distributed transverse matrix cracks, which led to several key observations.

For both LFC and HFC specimens, the highest density of AE events was generated within $\pm$ 1 mm of the failure location at stresses immediately prior to specimen failure (Figures 2.11 and 2.10), consistent with findings by Whitlow et al. [48]. Within this $\pm$ 1 mm region, AE was consistently generated in the vicinity of one or more matrix cracks throughout the loading profile, indicating that clustered local dynamic events (i.e. matrix

cracking, interfacial debonding, early fiber breaks, etc.) strongly correlated with failure. In both systems, a number of matrix crack locations away from the eventual failure plane became inactive (stopped generating AE) prior to the matrix crack saturation stress. These trends suggested that some cracks accumulated more damage (generated a greater number of AE events) and evolved as more probable failure locations.

The relatively weaker interfacial properties in LFC minicomposites (Table 2.2) enabled the increased activity of non-dominant mechanisms such as interfacial debonding, fiber sliding and pullout (described in greater detail in Chapter 3). Matrix crack opening resulted from elastic deformation and sliding of fibers during fiber bridging and load sharing (described in greater detail in Chapter 4); such mechanisms were active at all evolving cracks. In the vicinity of and away from the eventual rupture plane, it was observed that some matrix crack locations did not generate AE at intermediate stresses (typically 450-600 MPa), as shown in Figure 2.11. This trend suggested that crack opening at intermediate stresses was driven by non-dominant sliding and pullout mechanisms in the LFC system, which if independently occurring, may not produce sufficient AE energy to be captured.

In HFC minicomposites, stronger interfacial properties impeded these non-dominant phenomena (i.e. fiber sliding to relieve locally high stresses in the vicinity of matrix cracks). Initially, incremental transverse matrix crack growth resulted in a series of AE events at approximately the same axial locations, sometimes with multiple AE events occurring over the course of a single load increment. Once transverse cracks were observed as through-width (at which point, they were presumed through-thickness), continued crack opening was observed (as described in Chapter 4). At intermediate stresses (650-800 MPa), AE was often generated by matrix cracks other than the failure crack to a higher degree than observed in the LFC system. These AE events may be a result of early, local fiber failure due to the lack of debonding and sliding, in addition to progressive

cracking. As a result, there was no apparent drop-off in AE activity away from the failure plane, or dominance of the failure crack (in terms of coalescence of AE generated) prior to matrix crack saturation (Figure 2.10).

Finally, there was a correlation between high-energy AE (HEAE) events, those which exceeded 10% of the maximum energy event, and proximity to failure location in both HFC and LFC specimens. The highest density of HEAE occurred at cracks within ± 3 mm of the failure location (Figure 2.14). Outside of this range in HFC specimens, AE produced in the vicinity of matrix cracks was mostly low-energy AE (LEAE) events (below 10% of the maximum energy event). In LFC specimens, HEAE occurred outside the eventual failure location, where it was likely the result of large matrix crack formation. LEAE events were observed in both systems throughout loading. Often, LEAE occurred in the vicinity of already-formed, observable matrix cracks, likely due to subsurface matrix crack propagation and interfacial mechanisms. Furthermore, AE events generated during load holds always qualified as LEAE, although it is currently unclear if these AE events arose from the same non-dominant mechanisms captured during loading. Sevener et al. [22] observed that the matrix crack opening progressively decreased during unloading and reloading up to the same stress; they theorized that this was due to wearing of the interface, where fiber sliding enabled crack closure. Further work is needed to determine if there are differentiating characteristics of LEAE that correlate to different non-dominant damage mechanisms or small, dominant damage mechanisms, which are described in Chapter 5.

HEAE was typically observed at: (i) stresses near and at specimen failure, where these events were assumed to be the result of significant quantities of near-simultaneous fiber breaks, and (ii) stresses prior to the matrix crack saturation stress, where these events were assumed to be the result of large matrix crack formation. Ultra-high-energy AE (UHEAE) events, which exceeded 30% of the maximum energy event for a given

specimen, were more frequently observed in the LFC system. Considering that fewer AE events were generated in LFC specimens compared to HFC specimens, and taking into account the stress domain over which these were observed, it is like that the propensity for UHEAE observed in LFC specimens is the result of in-plane matrix crack initiation and propagation to through-thickness. In HFC specimens, a large quantity of HEAE was also observed during the matrix-dominated regime (Domain I), which was assumed to be the result of partial-width matrix cracking events across the HFC cross-sections. As shown in Figure 2.14, the highest energy event in HFC specimens was typically observed at the fracture location where rupture of the fiber tow occurred. In LFC specimens the majority of UHEAE events occurred at stresses in the matrix-dominated regime, including the highest energy event, which was also typically generated at the matrix crack location where the specimen eventually failed. As further explored in Chapter 3, one hypothesis for this trend was that the relative magnitude of these UHEAE and HEAE signals correlated with the surface area created by the formation of matrix cracks and the quantity of fiber breaks.

2.3.3 Crack Density Evolution

Two independent measurements of the transverse matrix crack density evolution (CDE) as a function of the globally-applied stress, made by in-SEM and AE characterization, showed a strong correlation for both LFC and HFC specimens (Figure 2.13). In past efforts, the characteristic S-shape of both the CDE curve [17] and the AE energy accumulation curve [41] has been used to justify the use of AE in the characterization of transverse matrix cracking [49]. However, this is the first time that these two curves have been generated simultaneously and compared.

For the HFC system, the two CDE measurements strongly correlated throughout

specimen loading, indicating that matrix cracking was the dominant damage mechanism (and source of AE emission) until the matrix crack saturation state. This is consistent with the hypothesis that the interfacial conditions enabled limited non-cracking phenomena, and non-dominant toughening phenomena critical to the composite response were restricted. High sliding stresses limited fiber mobility once cracks had propagated to the interfacial region, and crack deflection at strongly bonded interfaces was impeded by the high debond toughness.

Higher crack densities also were observed in the HFC (3.5 ± 0.1 mm^{-1}) versus LFC specimens (2.5 ± 0.1 mm^{-1}). This was attributed to higher sliding stresses in the HFC system, which led to smaller sliding zone lengths around matrix cracks and shorter regions over which load could be recovered in the matrix away from the crack plane; this corresponded to a smaller observed matrix crack spacing [28]. Typically, a higher crack density was observed near the rupture zone in LFC specimens, which is consistent with observations from [5], while the matrix crack spacing was fairly periodic in HFC specimens.

In the LFC system, larger variations were observed between the two CDE measurements, likely as a result of non-matrix cracking phenomena. While a strong correlation was observed at low stresses (< 400 MPa), indicating that matrix crack formation was the dominant *initial* mechanism generating AE, small overestimations in AE-estimated CDE compared to the cracking response of specimens were observed at intermediate stresses (450-600 MPa). This suggested that after major matrix cracking, some portion of other damage phenomena (such as interfacial debonding, early fiber failure, etc.) generated AE, and these signals were incorporated in the CDE calculation because of an inability to decouple them from the global AE data. At these intermediate stresses, AE data mostly consisted of low-energy AE (as shown in Figure 2.14) generated in the vicinity of already-formed matrix cracks, consistent with non-dominant phenomena and early fiber

breaks.

An alternate visualization of the key findings of Figures 2.14 and 2.13 is shown in Figures 2.15 and 2.16. In these schematics, the sizes of spatially-mapped AE events for four HFC and LFC specimens are related to their event energies. In LFC specimens, where the matrix crack density is lower, there is a distribution in UHEAE events across several cracks, where the UHEAE is often generated at the initiation of the crack and subsequently followed by lower-energy AE near the crack plane. This is consistent with the formation of large or through-width matrix cracks in LFC specimens, and indicates that there is subsequent damage accumulated from other phenomena in the plane of the crack that generate AE throughout the specimen lifetime. Whereas in HFC specimens, UHEAE events are more often generated *after* the matrix crack initiation. One explanation of this trend is that matrix cracks initiate in the smaller, isolated regions of the cross-sections that experience locally high-stresses; from there they propagate into the larger, connected regions of the cross-section upon increased loading where relatively larger matrix crack surface areas are created, producing higher energy AE. In both LFC and HFC specimens, UHEAE events are also observed in the plane of the failure crack at rupture stresses, which indicates that the catastrophic nature of rupture (cracking of the fiber tow in conjunction with additional local cracking of the matrix) is captured by AE, consistent with [48]. These observations suggest that the energy released by AE events may shed insight on the size and nature of the damage mechanism which generated it, motivating the investigation described in Chapter 3.

2.4 Summary

In this chapter, a multi-modal approach combining in-SEM tensile testing for the high-resolution mapping of surface damage with AE measurements for damage charac-

terization in the bulk was used to quantify the initiation and evolution of damage in two systems of SiC/SiC minicomposites: (i) a high fiber content (HFC) system with low, discontinuous CVI SiC matrix content and BN interphase thicknesses on the order of ≈2 µm; and (ii) a low fiber content (LFC) system with a continuous overlayer of SiC matrix and BN interphase thicknesses of ≈ 300 nm. These two SiC/SiC systems were used to compare variations in damage progression in terms of known microstructural differences and the experimentally-measured AE generated during loading. The following findings resulted from this work:

- In both systems, early surface microcracking emanating from preexisting flaws could be correlated with its resultant AE. Additionally, all observed surface damage could be directly mapped onto corresponding AE events. When AE could not be readily correlated with observable damage, damage was likely initiating subsurface or on the opposite surface, but at these axial locations, damage progressed to the surface at higher stresses.

- LFC specimens generated fewer AE events than similarly sized HFC specimens. This behavior was attributed to: (i) through-thickness matrix crack formation in fewer steps as a result of an interconnected in-plane matrix network, (ii) lower interfacial properties that enabled non-dominant damage mechanisms (e.g. debonding, sliding, and pullout), some of which likely were not detected by AE, (iii) larger sliding zones around matrix cracks leading to larger matrix crack spacing, and (iv) fewer early fiber failures, given that higher debond lengths were needed to accommodate crack opening, leading to large quantity, near-simultaneous fiber failures at stresses beyond crack saturation.

- In both systems, the highest density of AE events was generated near the failure location throughout loading by one or more evolving cracks, indicating that clus-

tered local damage mechanisms (i.e. matrix cracking, interfacial debonding, early fiber breaks, etc.) strongly correlate with failure. In the LFC system, sliding and pullout were likely the drivers for crack opening at intermediate stresses (450-600 MPa), where opening cracks generated little to no AE. In the HFC system, AE was often generated by opening cracks at intermediate stresses (650-800 MPa) and was not exclusive to the failure location. These AE events may be a result of local fiber failure due to the lack of debonding and sliding.

- After the onset of observable matrix cracking in both systems, low-energy AE was mostly generated in the vicinity of matrix cracks. In the LFC system, these were likely a result of debonding and sliding; in the HFC system where such phenomena were obstructed by high interfacial properties, these low-energy AE events were likely a result of incremental matrix crack propagation and local fiber failure. High-energy and ultra-high-energy AE in LFC and HFC specimens occurred at either: (i) stresses near failure, where they were assumed to be the result of near-simultaneous, large quantity fiber failure, and (ii) at earlier stresses, where they were linked to matrix crack initiation events. In both systems, there was a correlation between high-energy AE and the eventual failure location, suggesting that these events may provide an early indication of areas of concern.

- A stronger correlation between AE-estimated CDE and experimental CDE was observed in HFC specimens versus LFC specimens, indicating that transverse matrix cracking was the dominant damage mechanism generating AE up to crack saturation in the HFC system. In LFC specimens, it appears that some non-dominant mechanisms enabled by globally lower interfacial properties generated AE, accounting for the over-prediction of the AE-estimated CDE compared to the cracking response.

This investigation shows that CMC damage mechanisms and the manner in which they evolve may be more predictive than previously thought. Early cracks form as a result of preexisting flaws [1]; subsequent transverse matrix crack locations are determined by the interactions of key microstructural and constituent features (in-plane matrix content, local stresses, interphase characteristics, etc.) and evolving local damage mechanisms with stress. These initial conclusions highlight a need to characterize the AE signatures generated by individual damage mechanisms and to develop novel multimodal approaches and statistical frameworks to understand the effects of the surface and subsurface architecture on damage. These investigation are described in the following chapters.

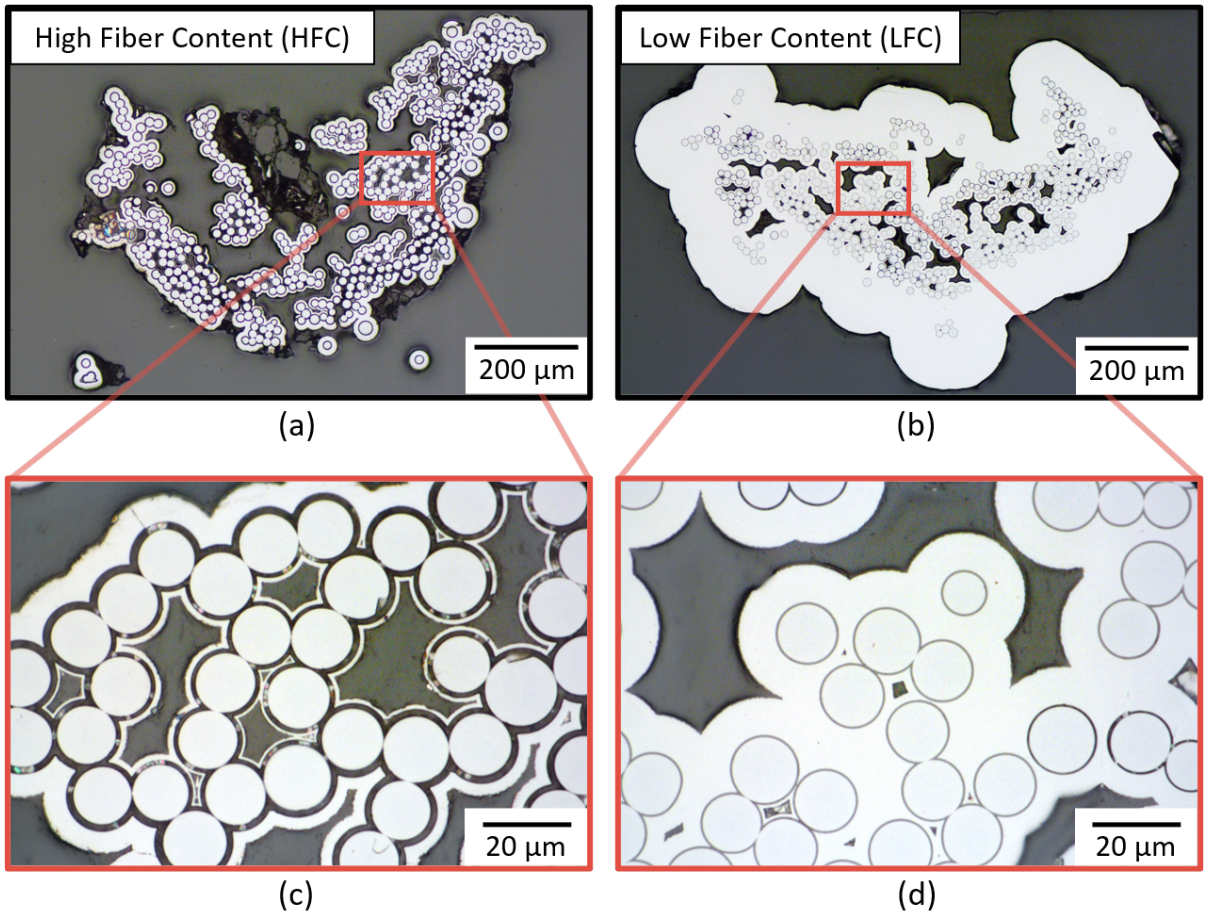

Figure 2.1: Cross-section of **a)** HFC minicomposite, **b)** LFC minicomposite, **c)** and **d)** close-ups of the cross-section showing the interphase thicknesses and matrix coating.

Specimen ID	V_f (%)	V_m (%)	V_i (%)	Area (mm^2)
1-1	33.5	41.8	24.6	0.169
1-2	38.9	37.7	26.4	0.157
1-3	32.5	43.6	23.9	0.174
1-4	34.4	40.3	25.3	0.164
2-1	22.7	74.9	2.3	0.249
2-2	21.3	76.5	2.2	0.266
2-3	24.2	73.3	2.5	0.233
2-4	23.0	74.7	2.4	0.246

Table 2.1: Constituent properties of two minicomposite systems studied in-SEM. From specimen cross-sections (Figure 2.1), average BN thicknesses and fiber diameters were measured and used to determine nominal cross-sectional areas following [5].

	Sliding Stress (τ)	Debond Toughness (Γ)
HFC	34.5 ± 13.0 MPa	5.5 ± 3.9 J/m^2
LFC	18.1 ± 4.8 MPa	1.2 ± 0.5 J/m^2

Table 2.2: Properties of minicomposite systems determined from fiber push-in testing.

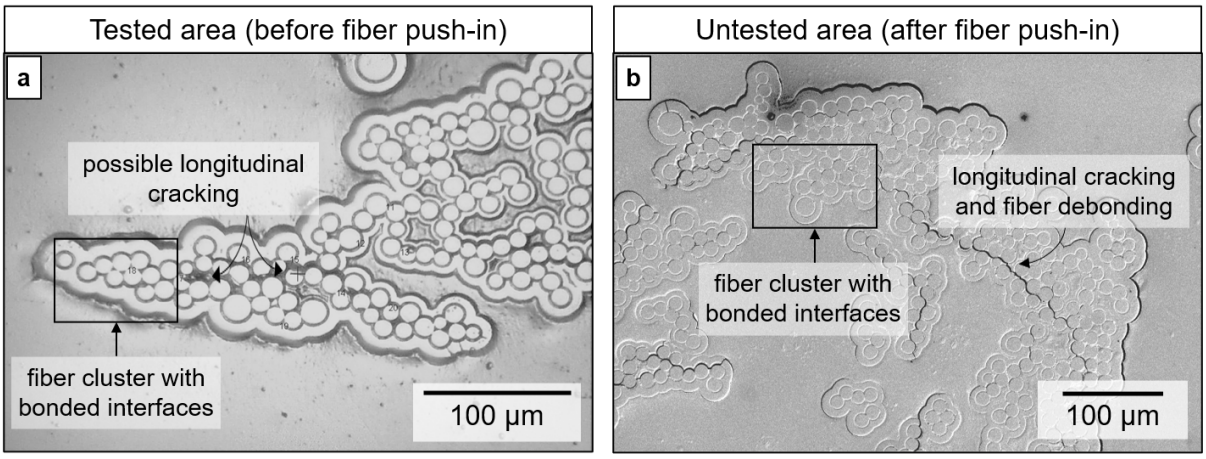

Figure 2.2: **a)** Dark interfacial regions were observed in pre-tested areas of HFC specimens, correlating with possible longitudinal cracks (micrograph via nanoindenter objective). **b)** Longitudinal cracking was observed in untested areas of the cross-section after fiber push-in testing, leading to debonded fibers which exhibited near-zero debond toughness (micrograph via SEM)

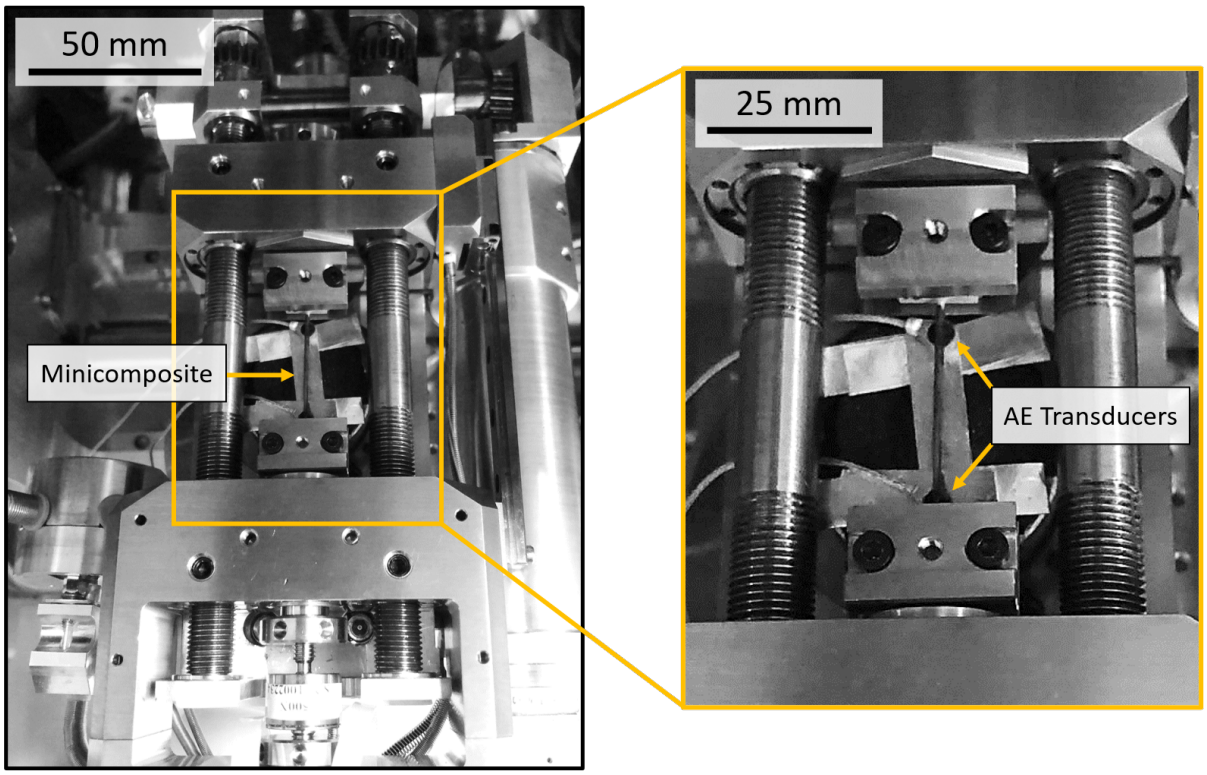

Figure 2.3: Tensile load frame mounted in-SEM. AE sensors were coupled with vacuum grease underneath the sample and located near the grips. The area investigated with SEM was the largest observable length of the gage not obscured by vacuum grease.

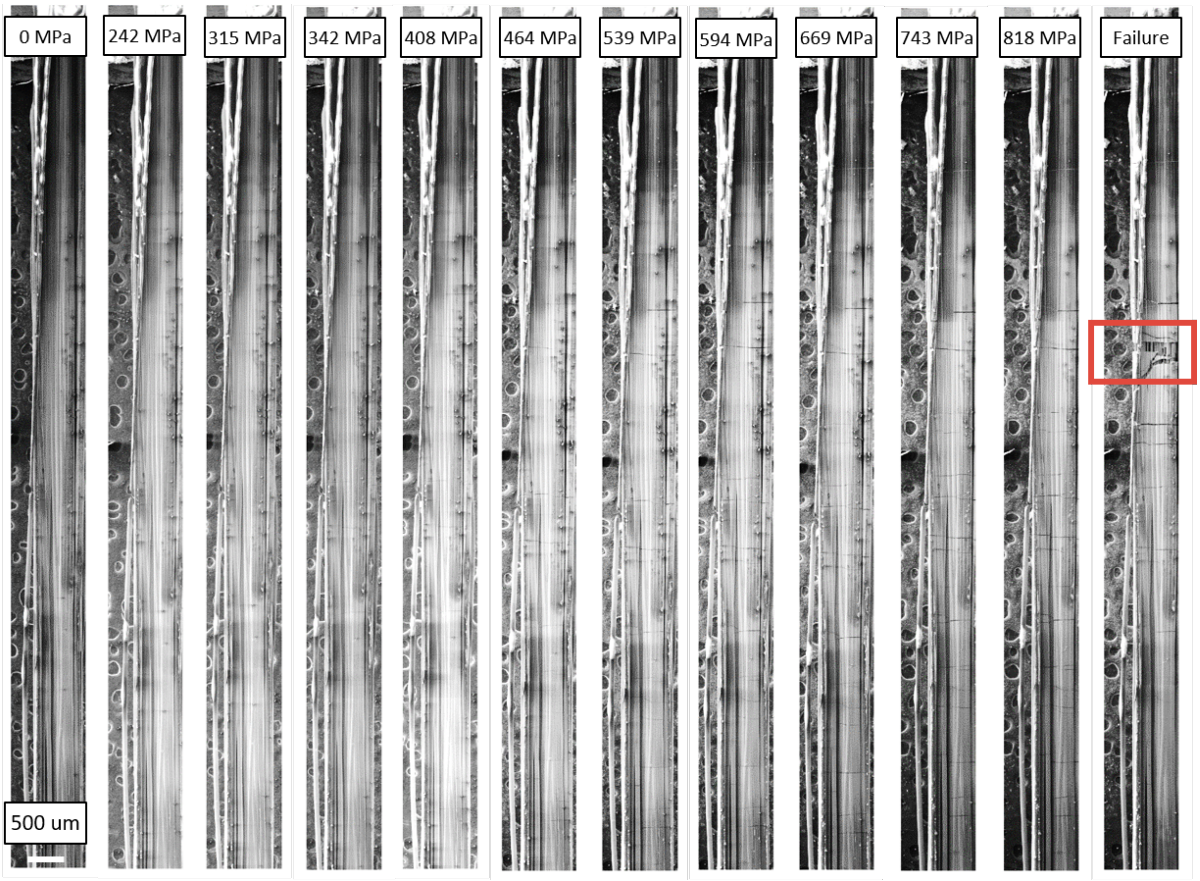

Figure 2.4: Incremental loading of minicomposites enables capture of the damage accumulation at the specimen surface, and primarily the evolution of matrix cracking. Combined with acoustic emission monitoring, this method allows for a resolved capture of the damage evolution both at the specimen surface and in the material bulk.

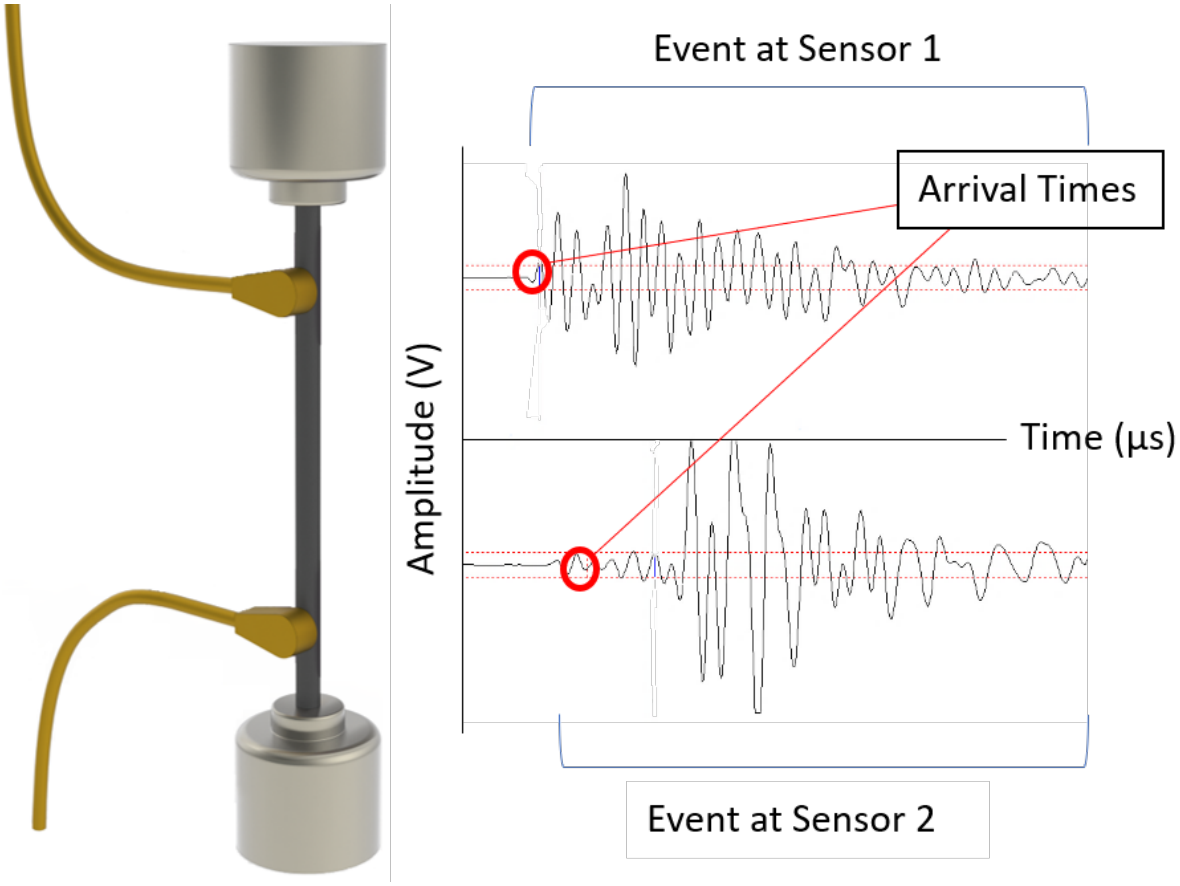

Figure 2.5: A schematic of two waveforms captured via AE. The arrival time of the waveform is determined as the first peak of the extensional wave, or the peak immediately after the pre-trigger noise component.

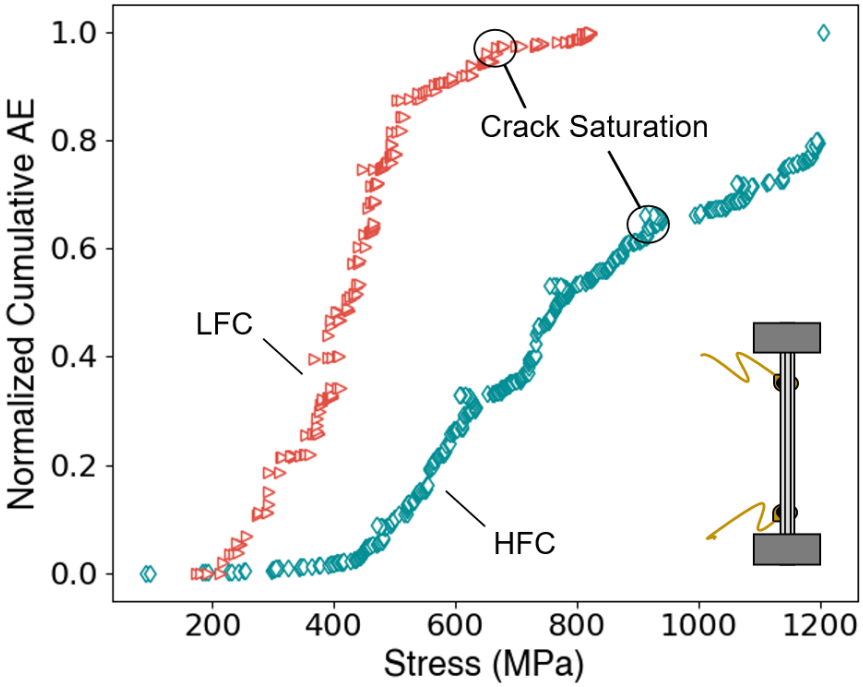

Figure 2.6: Normalized cumulative AE versus stress curves for an LFC and HFC specimen. Crack saturation was approximated by a plateau in AE activity, due to elastic fiber loading prior to fiber breakage, and occurred at approximately 600-650 MPa in the LFC system and 800-850 MPa in the HFC system.

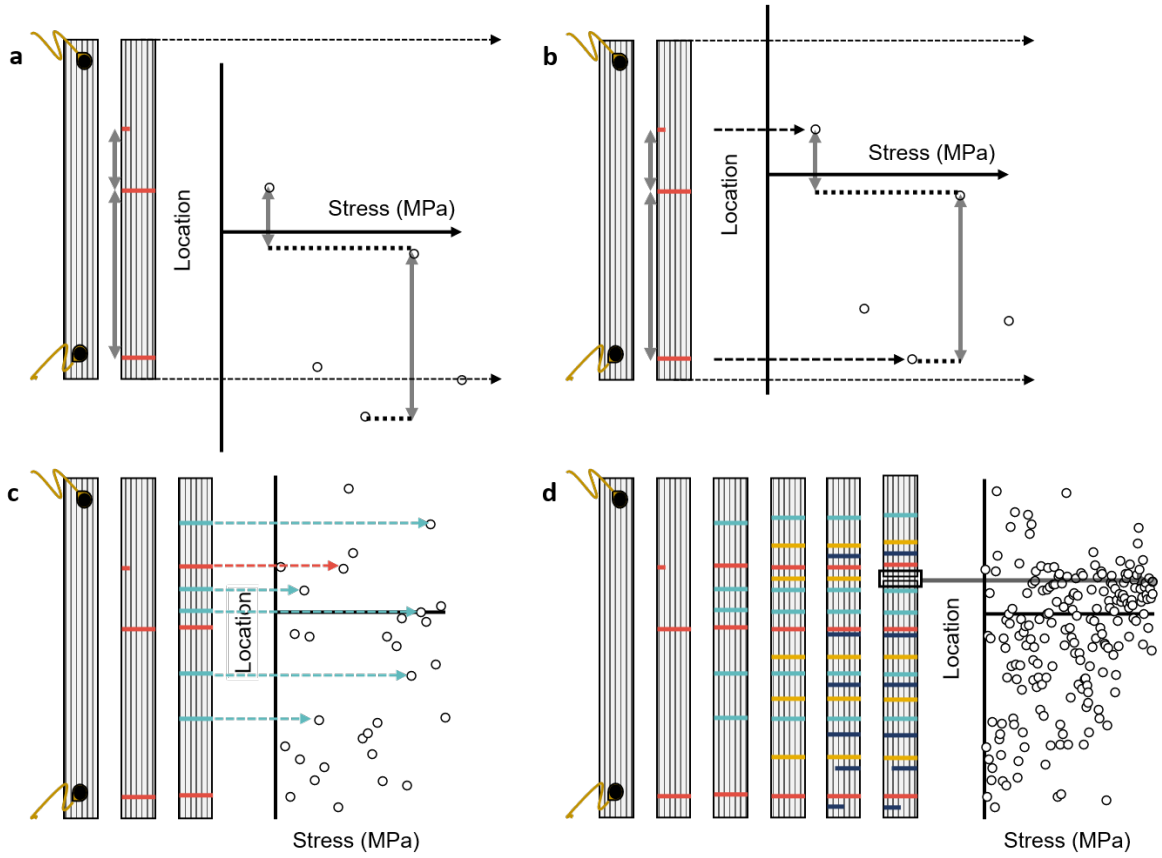

Figure 2.7: A framework for improved spatial alignment of in-SEM observed damage and AE information: **a)** AE activity was generated by loading a specimen to stress σ_1; in the sample reference frame, observed surface damage at σ_1 produced AE. Grey arrows indicate the distance between the surface damage, which correlates with the spatial distribution of some AE events. **b)** The matching spatial distribution between surface damage in the sample reference frame and AE events in the AE reference frame, are used to shift the sample reference frame to its absolute position. There is a direct mapping of the surface damage onto the corresponding AE. **c)** This alignment was validated with continued loading; at stress σ_2, new surface damage was correlated to its AE events and AE generated in the vicinity of existing damage was tracked. **d)** Alignment was validated at failure, where a high density of AE activity was observed near the final failure location (boxed in black).

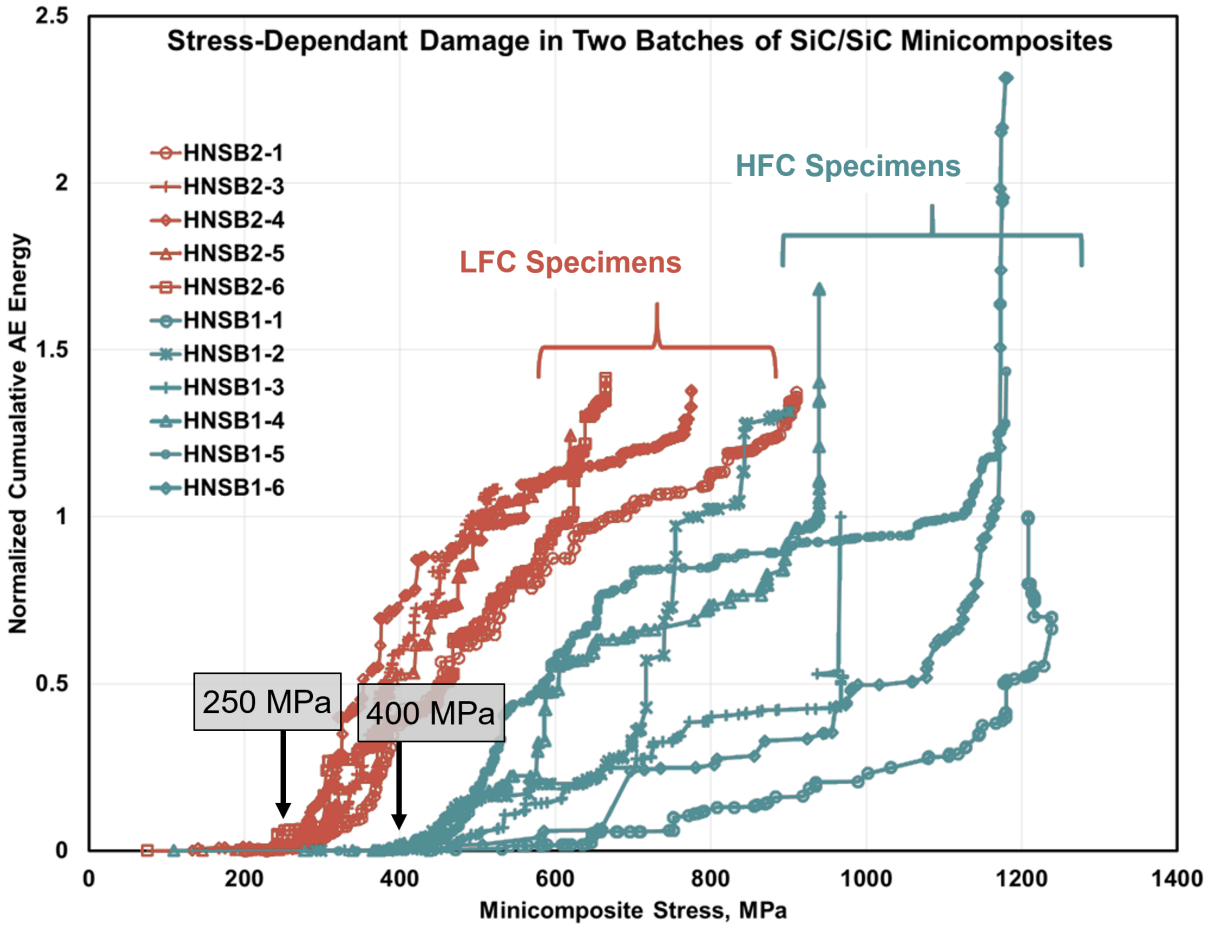

Figure 2.8: In both systems of SiC/SiC minicomposites investigated herein, low-energy AE has been captured below the PL, in agreement with prior studies. Here, Batch 1 is equivalent to the HFC system, and Batch 2 equivalent to the LFC system. Courtesy of Almansour, Gorven, and Swaminathan (unpublished).

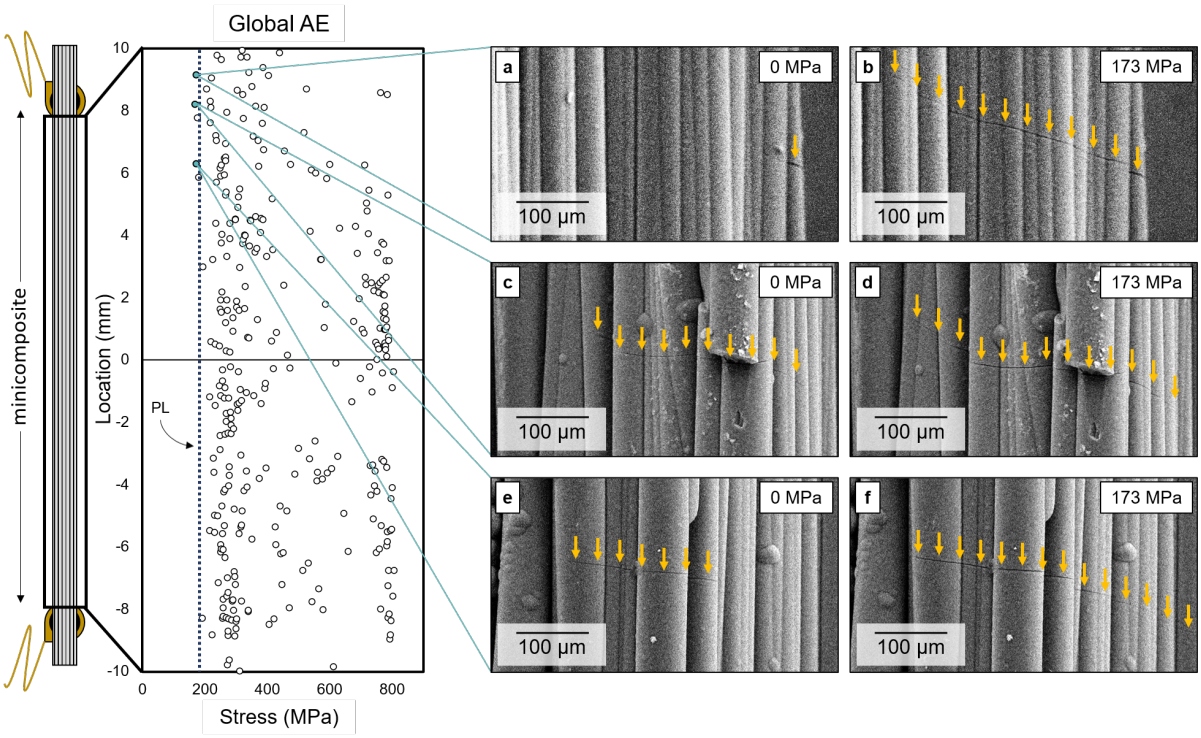

Figure 2.9: High resolution mapping of AE activity enabled correlation of early AE with observable surface damage in-SEM for an LFC specimen. **Left)** Global AE activity mapped along the sample gage as a function of stress, where the PL was approximately 190 MPa. Three AE events generated below the PL are highlighted. Right) Unloaded state surface defects (a, c, e) and microcrack propagation observed by increasing stress to 173 MPa (b, d, f), respectively, correlated with the early AE events

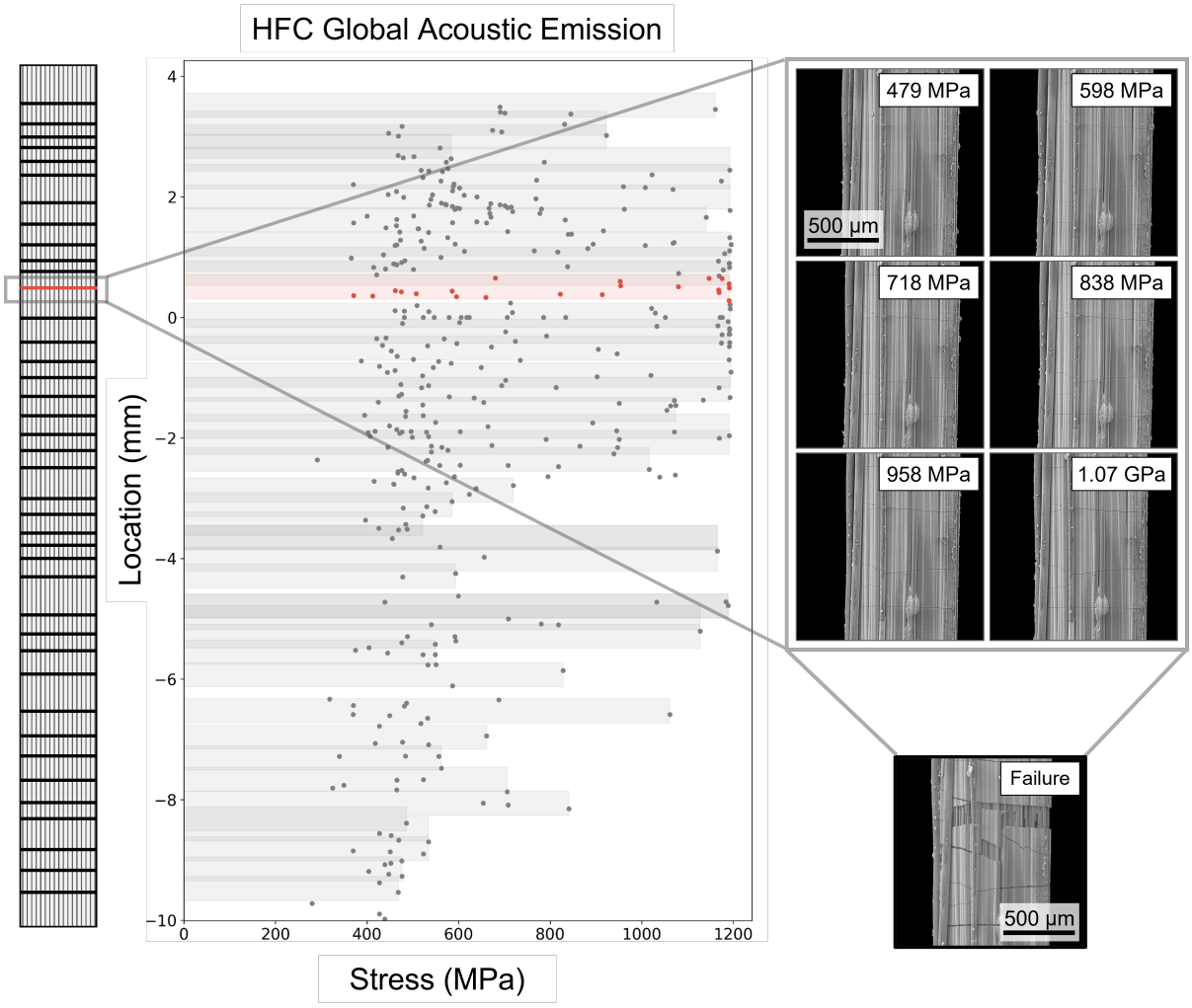

Figure 2.10: Global AE data for an HFC specimen aligned with a map of transverse matrix cracks observed in-SEM. A much greater quantity of AE is produced in HFC specimens compared with similarly-sized LFC specimens, predominantly during the matrix-dominated response. This is likely due to differences in the initiation and evolution of matrix cracking.

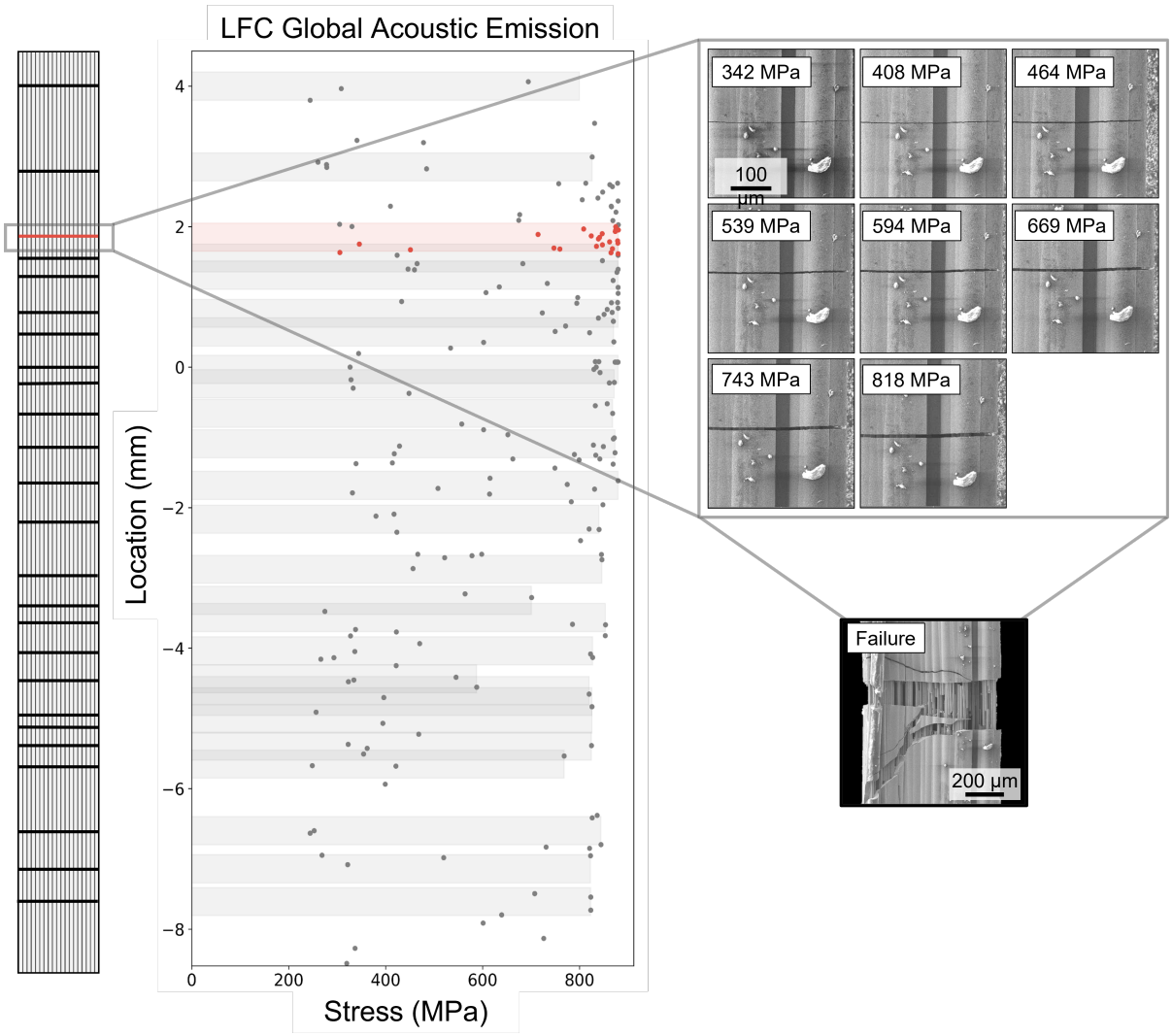

Figure 2.11: Global AE data for an LFC specimen HFC specimen aligned with a map of transverse matrix cracks observed in-SEM. The failure location (indicated by the red box) correlated with the last AE event, and the progressive surface cracking at and near the failure location is shown by the micrographs. The correlation of the two maps showed that cracks near the failure location typically generated a greater quantity of AE than cracks away from the failure location.

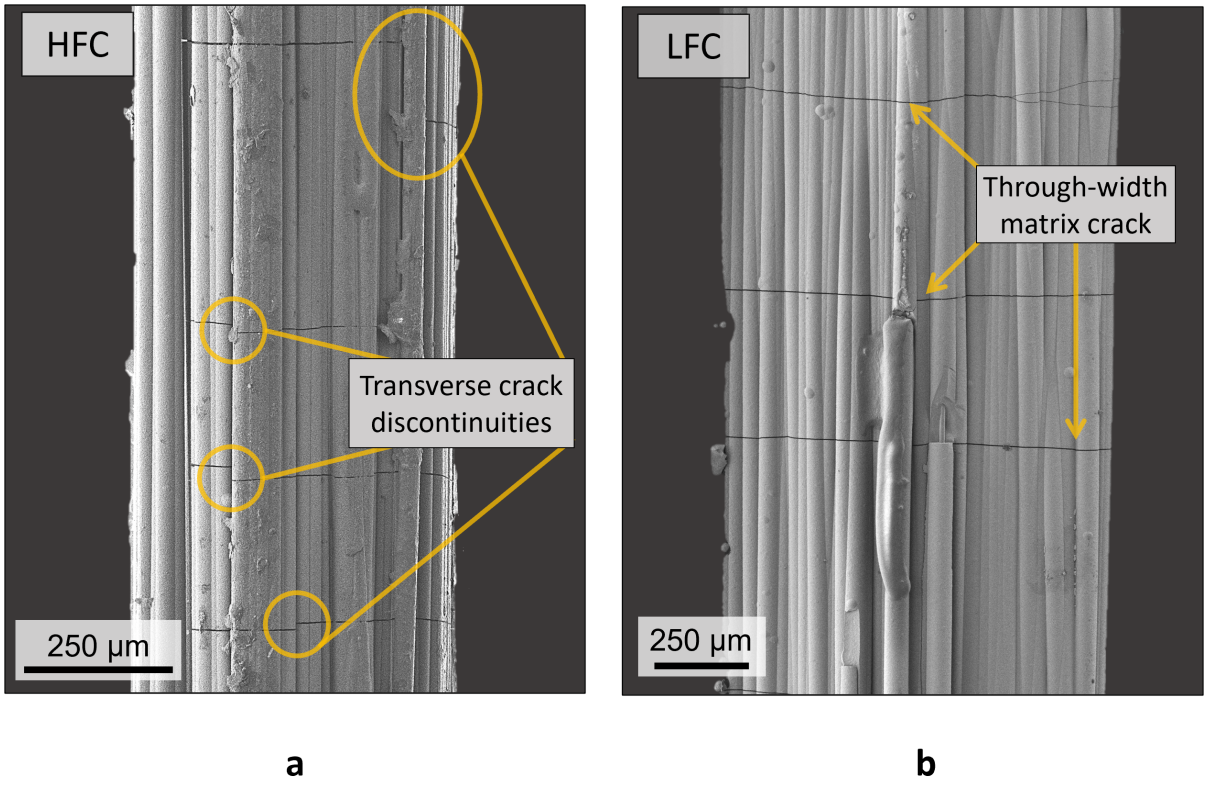

Figure 2.12: Matrix cracking was captured prior to failure in an **a)** HFC specimen and **b)** LFC specimen. In **a)** discontinuous transverse matrix cracking was a result of incremental crack propagation. Cracks initially propagated through one or more isolated portions of the CMC cross-section (i.e. microcomposites). When no further in-plane matrix pathway existed for propagation to through-thickness, these cracks deflected along the specimen length until a pathway emerged for continued transverse cracking. In **b)** an interconnected matrix network facilitated crack propagation to through-thickness. These cracks bypassed small areas that were disconnected from the bulk, as shown by the disconnected fiber in (b).

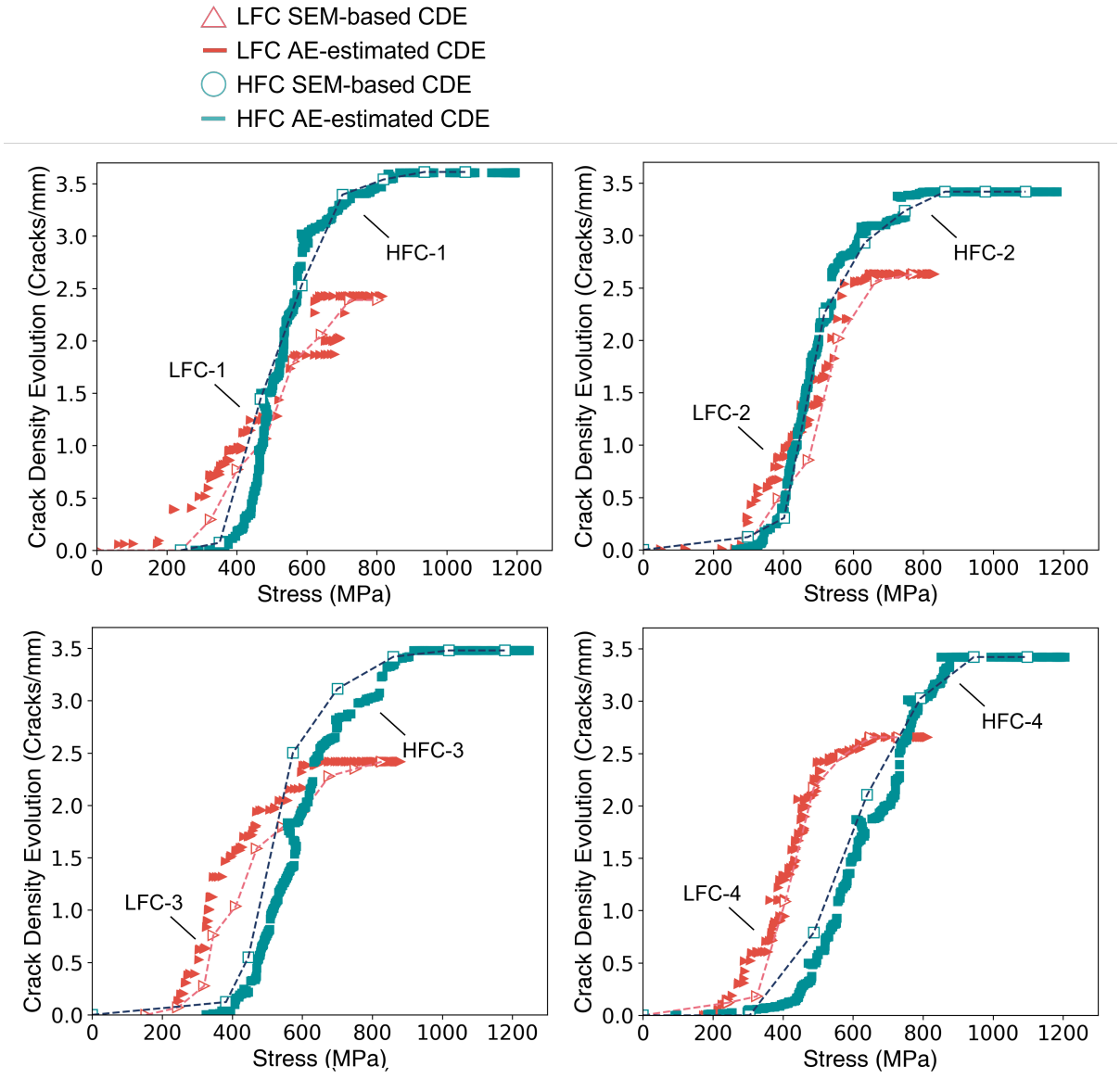

Figure 2.13: Agreement between two independent measurements of crack density evolution (CDE), made by in-SEM and AE characterization, shown for four LFC and four HFC SiC/SiC minicomposites.

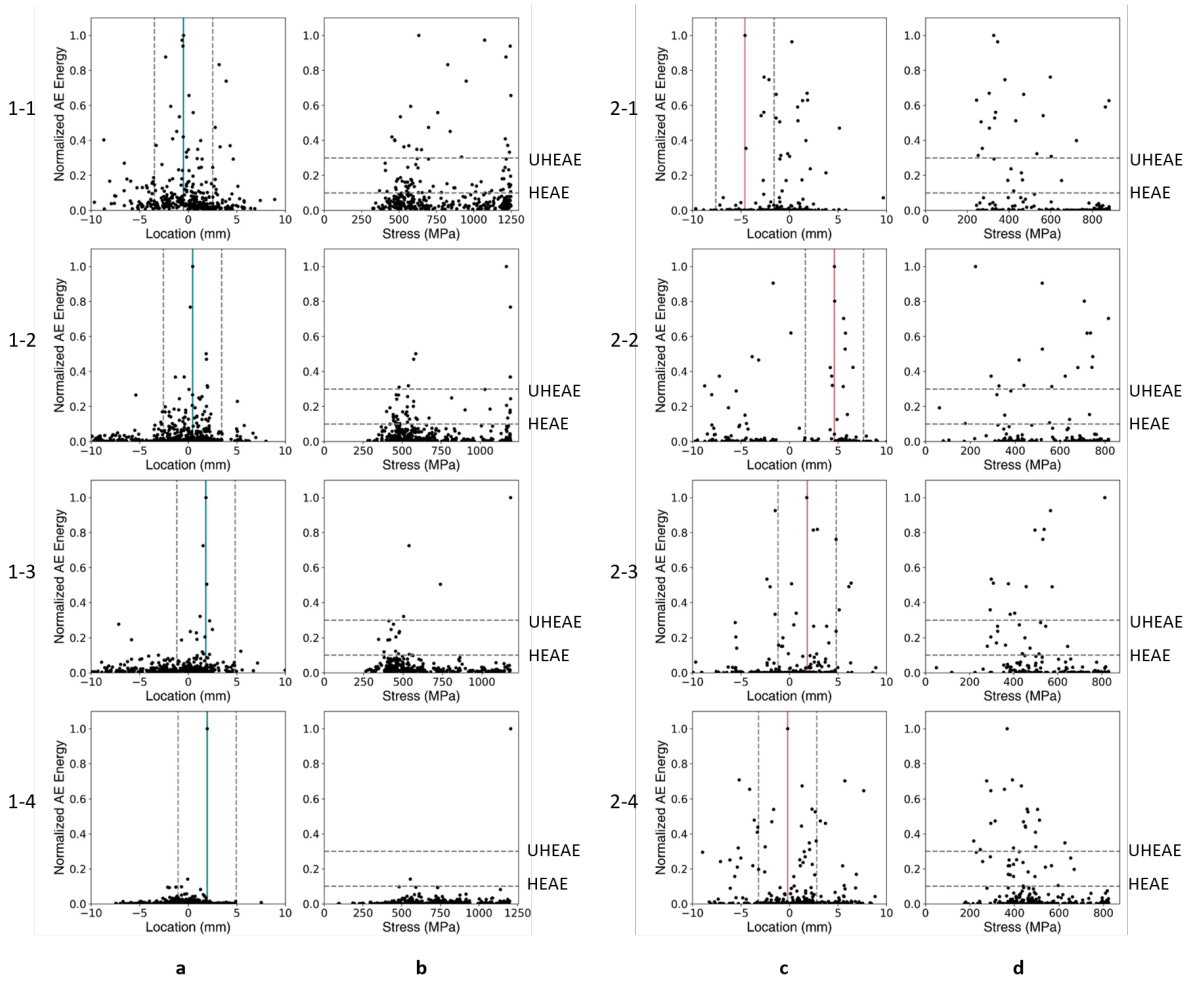

Figure 2.14: **a)** and **c)** A correlation was observed between high-energy AE (HEAE) activity (exceeding 10% of the maximum energy event) and the failure location for all HFC specimens (left, shown in blue) and three of four LFC specimens (right, shown in red). The majority of these events typically occurred within ± 3 mm of the failure location (boundaries shown with dotted gray lines in Normalized AE Energy versus Location curves). HEAE was generated throughout the stress profile, shown by **b)** and **d)**. Ultra-high-energy AE (UHEAE) events (exceeding 30% of the maximum energy event) were more commonly observed in LFC specimens compared to HFC specimens. The highest energy event is highlighted for each sample.

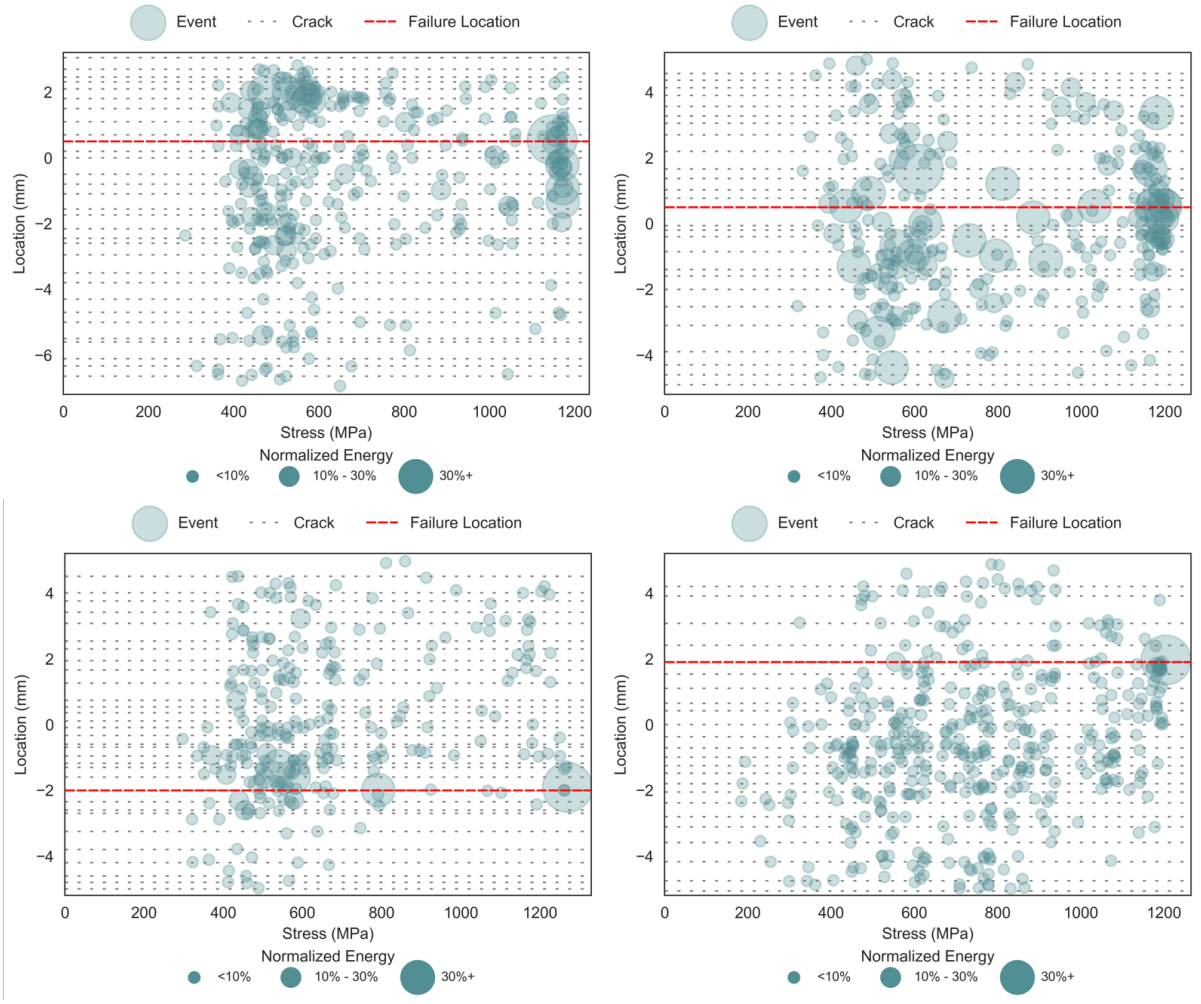

Figure 2.15: Distribution of AE events with respect to their signal energies for HFC specimens. Primarily, we find that damage (presumably matrix cracking) in HFC specimens initiates with lower energy AE events producing high energy AE at later stages of crack growth.

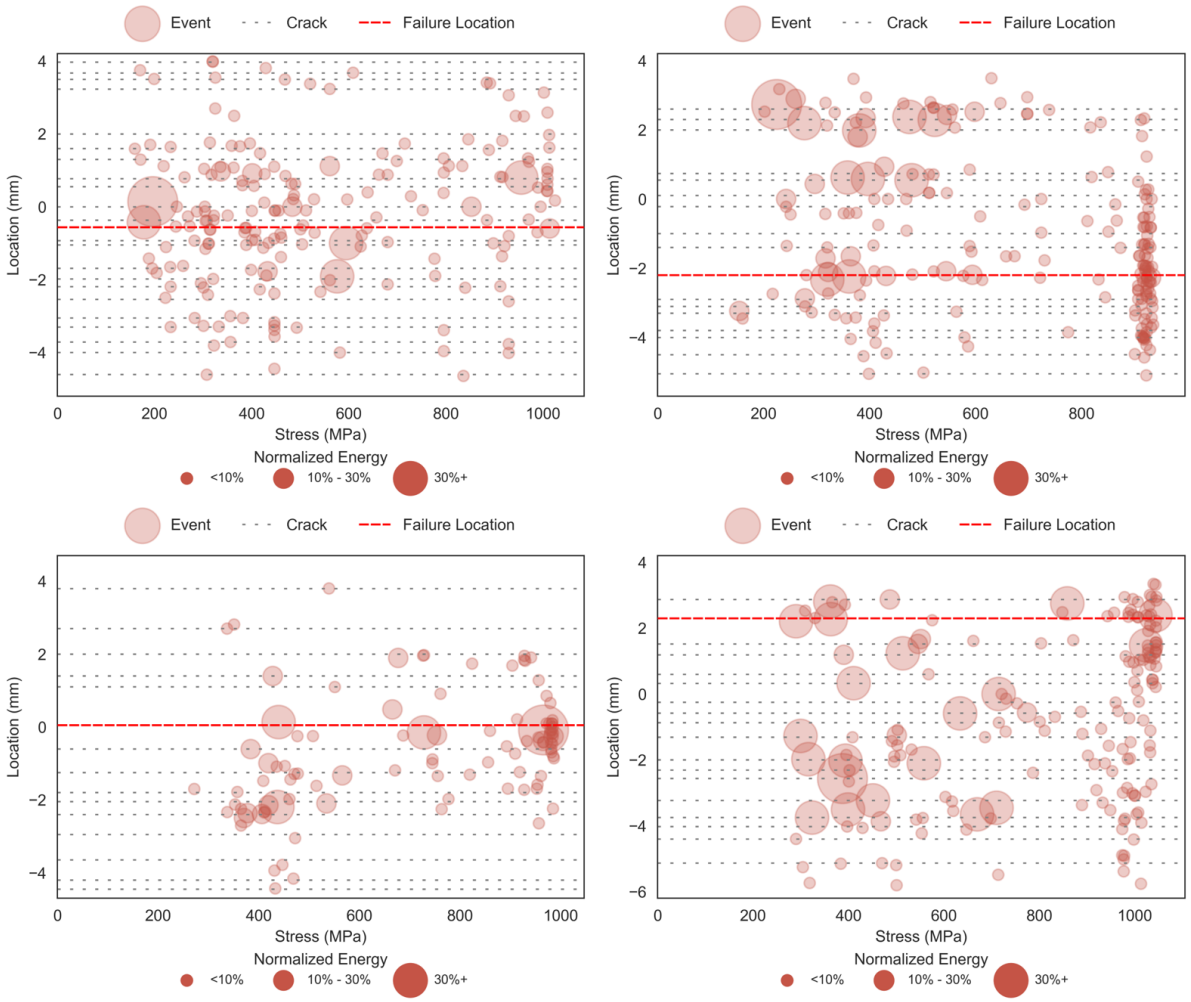

Figure 2.16: Distribution of AE events with respect to their signal energies for LFC specimens. Primarily, we find that damage (presumably matrix cracking) in LFC specimens initiates with high energy AE events, with lower energy AE subsequently accumulated in the vicinity of the crack planes.

Chapter 3

Correlation of Acoustic Emission Energy with Damage Accumulation in SiC/SiC Minicomposites

3.1 Scope

In this chapter, the fracture area created by each damage event in SiC/SiC minicomposites under uniaxial loading was estimated by relating predicted damage accumulation to experimentally-measured AE energy accumulation. This investigation used insights gained from combining AE measurements with in-SEM mechanical testing [61] and certain assumptions on specimen geometry and damage mechanisms. This investigation was based on the hypothesis that the 'loudness' of an AE event (i.e. its energy or amplitude) corresponds to the surface area created by its damage source [41]. As such, the total AE energy generated by a mechanism is related to the total surface area created by its occurrences, a hypothesis that is supported by a recently observed relationship between AE energy accumulation and measured crack surface area in SiC/SiC composites [34].

The current understanding of damage accumulation in unidirectional SiC/SiC is that when a matrix crack initiates, it is accompanied by simultaneous debonding of the fibers from the matrix and subsequent frictional sliding in the vicinity of the matrix crack. These three mechanisms occur near-simultaneously (strictly over finite, but very short time scales that are dictated by the wave speeds). Following the formation of a single crack and upon further loading, the slip zone (i.e. the region over which the interface has debonded and slid) increases approximately linearly with applied stress. Beyond the slip zone, the matrix stress remain unaffected, which allows for additional cracks to form. Debonding and sliding occur adjacent in the vicinity of each crack plane in identical fashion, such that the slip length adjacent to a crack is the same for all cracks at a given stress. Eventually, the slip zones overlap. This point, where the stress in the matrix cannot increase, corresponds to the matrix crack saturation state. At matrix crack saturation, it is often assumed that the entire interface is debonded. Thereafter, as loading continues, fibers begin and continue to break; sliding over longer length scales occurs adjacent to each break. Between matrix crack saturation and specimen failure, the active mechanisms are fiber breaks combined with additional sliding [3, 85, 16].

While there is consensus that the dominant damages mechanisms like matrix cracking and fiber breakage are captured in AE, whether non-dominant mechanisms such as debonding and sliding are (as they are expected to emit lower frequencies), remains in dispute [71]. In this chapter, the sensitivity of AE to capture both dominant and non-dominant mechanisms in SiC/SiC minicomposites throughout the material lifetime was explored. Two scenarios were considered where either (i) AE was only sensitive to the occurrence of dominant damage mechanisms, or (ii) AE was sensitive to the occurrence of both dominant and non-dominant mechanisms. Thereby, in (i) the energies of captured AE events were only the result of surfaces created by the dominant damage mechanisms, and (ii) the energies of captured AE events were the result of surfaces created by the

simultaneous occurrence of dominant and non-dominant damage mechanisms. To investigate these possibilities, a set of boundary conditions were developed that bisect the lifetime of the material in the stress domain. First, the damage area accumulated *up to* the matrix crack saturation stress (Domain I) was assessed considering two scenarios: a **lower bound**, where AE was only sensitive to the dominant mechanism of matrix cracking; and an **upper bound**, where AE was sensitive to the occurrence of matrix cracking combined with simultaneous interfacial debonding and sliding. In the stress region between the matrix crack saturation state and rupture, two scenarios were used to assess the AE produced, which are complementary to the conditions described in Domain I. In **Condition 1**, AE was only sensitive to the dominant damage mechanism of fiber fiber failure (corresponding to the lower bound in Domain I), and in **Condition 2**, AE was sensitive to the simultaneous occurrence of fiber failure and additional frictional sliding (corresponding to the upper bound in Domain I). These Domain II conditions resulted in an estimation of the fiber break evolution, which was compared with estimations from relevant models in the literature [3].

3.2 Methods

Two systems of CVI (chemical vapor infiltrated) SiC/SiC minicomposite systems described as LFC and HFC specimens in Section 2.2 were incrementally loaded following the same protocol described in Section 2.2.

AE activity was monitored using the same configuration as described in Section 2.2. The signal energy of an event was calculated as the average of the energies at both AE sensors to (i) account for energy attenuation due to waveform propagation, and (ii) allow comparison of damage mechanisms of the same estimated size. In regard to (i), Morscher et al. found that waveforms in a CMC could lose over half their signal

energy when propagating to the sensor farthest from the source; this loss only increased with damage accumulation [79]. To better clarify the importance of (ii), consider the example of a through-thickness crack forming near one sensor. This crack would have a greater difference in waveform amplitude compared to a similar crack forming in the center of the specimen gage, whose waveforms propagate a similar distance. Use of the maximum recorded waveform energy between sensors would suggest that the crack that forms near one sensor creates more surface area than the crack that forms in the gage center. Whereas, the average energy of these damage events would be similar, in correspondence with their similar crack areas. Prior to analysis, each AE event was manually checked for wave clipping (saturation), and no clipping was observed.

3.3 Results

Relating the total surface area created by all damage mechanisms (hereafter referred to as the *damage area*) to the accumulated AE energy is currently prevented by limitations in resolving subsurface damage mechanisms. Here, the occurrence of visible matrix cracks on a specimen surface was used to estimate the damage area up to matrix crack saturation. This was motivated by prior results [34] that demonstrated a linear relationship between the accumulated surface area created by damage and the accumulated AE energy. This assumption was maintained in the scenario that non-dominant or secondary mechanisms (i.e. fiber debonding and sliding) are captured by AE, as it was assumed that these mechanisms occur simultaneously with the dominant damage mechanisms in a similar manner (i.e. at a fixed stress, the slip length adjacent to a crack was the same for all cracks), though the strain energy released by these secondary mechanisms was lower than that released by SiC fracture [61, 5, 86]. As described in Section 2.3.3, a strong correlation was observed between the crack density evolution (CDE) estimated

from the AE energy accumulation and experimental observations of matrix crack density in-SEM, with small overestimates of the AE-predicted CDE (<5%), particularly in LFC specimens [61]. These discrepancies likely resulted from independently occurring secondary mechanisms, which generated small AE energies. In this investigation, the small contribution from the possible independent occurrence of non-dominant mechanisms was neglected but the impact of their simultaneous occurrence with matrix cracking and fiber breaks was considered.

3.3.1 Modeling Damage up to Matrix Crack Saturation

The cumulative AE energy up to matrix crack saturation (AE^T_{sat}) was calculated as the sum of the energies created by N events ($E(N)$) up to N_{sat} that preceded matrix crack saturation:

$$AE^T_{sat} = \sum_{N=1}^{N_{sat}} E(N) \tag{3.1}$$

In determining AE^T_{sat}, matrix crack saturation was taken as the point in the AE energy accumulation curve where a plateau or lull in activity was observed, as shown for SiC/SiC minicomposites in [87]. The total damage area at matrix crack saturation and its relationship to AE^T_{sat} is difficult to estimate. Some cracks do not propagate through-width, and some through-width cracks do not propagate perfectly normal to the loading direction. It is difficult to estimate the portion of debonded fibers along the plane of a crack due to a non-uniform fiber distribution. The slip zone length also varies with local stress, and thus likely varies along the gage [16]. Currently, experimental capabilities are unable to visually observe all of these activities in the specimen bulk. Therefore, simplifying assumptions on specimen geometry and damage progression were made to relate AE signals to the activity of damage mechanisms and creation of damage surfaces.

Each minicomposite was simplified as a cylinder with uniform fiber distribution and

no porosity (Figure 3.1). The radius of the circular minicomposite cross-section (R) was estimated by relating πR^2 to the average cross section area (A_c) calculated using [5] and tabulated in Table 2.1.

The accumulated damage surface area *prior* to matrix crack saturation was estimated in relation to the accumulated AE energy, using a lower and upper bound assumption:

1. **Lower Bound**: Cracks initiated in the matrix and deflected around fiber surfaces with subsequent fiber debonding and sliding in the vicinity of each crack plane. It was hypothesized that AE was sensitive to *only* the dominant mechanism of matrix cracking. Therefore, only its occurrence contributed to the accumulation of AE energy. Each crack created two surfaces (i.e. crack faces) such that the total area accumulated at the matrix crack saturation stress was the sum of the estimated areas of these surfaces.

2. **Upper Bound**: Cracks initiated in the matrix, leading to debonding and sliding of fibers from the interphase over some averaged length (l_m) in the cross-sectional area propagated by the crack, where AE was sensitive to all three of these mechanisms. In addition to the two surfaces created by each crack, the surfaces created by the slip zones on each side of the crack plane contributed to the accumulated AE energies.

The following section describes a framework that was built to assess the relationship between the AE energy at matrix crack saturation (AE^T_{sat}) and the corresponding damage area at each of these bounds.

Lower Bound

The average surface area created by a through-thickness matrix crack (A_m) that deflected around all fibers was estimated by:

$$A_m = 2 \cdot V_m \cdot A_c \tag{3.2}$$

where V_m was the matrix volume fraction and the factor of two accounted for the formation of two crack faces. As BN interphases are significantly more compliant than SiC (elastic modulus $\approx$ 20 GPa for BN versus $\approx$ 410 GPa for SiC [88, 12]), it was assumed that the AE contribution of BN fracturing was negligible compared to that of the SiC cracking. Based on A_m, the total area generated by through-thickness matrix cracks (A_m^{tt}) was calculated as:

$$A_m^{tt} = A_m \cdot n_{tt} \tag{3.3}$$

where n_{tt} was the number of through-thickness cracks.

The areas created by cracks that were partially propagated through-width at matrix crack saturation were also considered, as these cracks generated AE. It was assumed that the surface progression of a crack reflected its through-thickness progression. For instance, in Figure 3.1, the sample shown in Figure 3.1a (Orientation 1) was rotated to obtain the view shown in Figure 3.1b (Orientation 2); the crack initially observed as partial-width now appears nearly through-width. The in-SEM view of minicomposite systems was susceptible to this orientation-dependent crack area measurement. Partial cracks made up $< 15\%$ of all cracks observed in-SEM at matrix crack saturation. As a result, there remained the possibility that some cracks that appeared to be through-width, and were thereby assumed to be through-thickness, were also orientation-dependent partial cracks. It was assumed that the different possible sample rotations had an averaging

effect, which was reasonable given that these minicomposites were not designed with any orientation-dependent anisotropy. For a partial crack of length l (Figure 3.1a), the crack area ($A(l)$) was calculated as the area of the arc ABC (A_{ABC}) multiplied by V_m, which was the portion of the crack front area containing matrix. A_{ABC} was calculated as:

$$A_{ABC} = \frac{R^2\theta}{2} - R\sin\left(\frac{\theta}{2}\right)(R-l) \tag{3.4}$$

$$\theta = 2\cos^{-1}\left(\frac{R-l}{R}\right) \tag{3.5}$$

where R was the radius of the sample cross-section, and θ was the angle swept out by the arc ABC in radians (Figure 3.1). The matrix crack surface area $A(l)$ was:

$$A(l) = 2V_m R^2\left(\cos^{-1}(1-x) - x(1-x)\sqrt{\frac{2}{x}-1)}\right) \tag{3.6}$$

where $x = 1/R$. The lower boundary on total surface area generated by cracks at matrix crack saturation (A_{sat}^{lower}) was calculated as the sum of the surface areas created by each through-thickness crack plus the surface areas created by p partially through-width cracks, each with an individual length l:

$$AE_{sat}^{lower} = A_m^{tt} + \sum_{i=1}^{p} A(l_i) \tag{3.7}$$

The value of A_{sat}^{lower} was calculated for each specimen. The relationship between A_{sat}^{lower} and the AE energy accumulated up to matrix crack saturation (A_{sat}^{T}) was then determined based on a coefficient for the AE energy per unit area released from matrix cracking (λ^c):

$$AE_{sat}^{T} = \lambda^c A_{sat}^{lower} \tag{3.8}$$

The variable λ^c was calculated for each specimen and varied between 9.1 - 27.1 $V^2\mu s/mm^2$ and 4.5 - 23.7 $V^2\mu s/mm^2$ for the LFC and HFC specimens, respectively. At matrix crack saturation, nearly twice the AE energy was accumulated in LFC (62 - 218 $V^2\mu s$) compared to HFC specimens (21 - 118 $V^2\mu s$). This increase could be attributed to the greater damage surface area created by matrix cracking in the LFC specimens at matrix crack saturation, with $\approx 6.74\ mm^2$ and $\approx 3.98\ mm^2$ for LFC and HFC specimens, respectively. Using the λ^c parameter, Eq. 3.8 was modified:

$$A^{lower}(N) = \frac{E(N)}{\lambda^c} \tag{3.9}$$

where $A^{lower}(N)$ is the calculated area of event N and *E(N)* is the energy of that event. The estimated damage area created by each AE event up to the matrix crack saturation stress based on the lower bound is shown in Figure 3.2.

Upper Bound

In the upper bound, the surface area of an AE event was assumed to be caused by the simultaneous occurrence of matrix cracking, interfacial debonding, and frictional sliding in the vicinity of the crack plane. The slip zone length was calculated using [89]: $l_m = \frac{(1-V_f)r\sigma}{2V_f\tau}$ where r was the fiber radius and τ was the interfacial shear stress (Table 2.2). For LFC specimens, this measure of l_m led to overlapping slip zones. Therefore, it was assumed that at the matrix crack saturation stress, fibers were fully debonded from their interphases (given a thin, weakly-bonded interphase that sufficiently promoted load transfer). By this, l_m equaled half of the matrix crack spacing, $l_m \approx 200\mu m$, based on the crack densities presented in Figure 2.13. It was assumed that $l_m = l_d = l_s$, where l_d was the debond length and l_s was the sliding length, as the slip zone encompassed the region in which the interphase had debonded and slid in the vicinity of a single matrix crack. For

HFC specimens, it was not assumed that the interface was fully debonded at matrix crack saturation. This was a non-standard material, where the microstructure characteristics did not reflect industry standard practices, and where models which considered thin, weakly-bonded interphases were not readily applicable. In HFC specimens the interfacial parameters were high, and the strong bond between the interface and fibers prevented sufficient load transfer and load sharing [90]. High interfacial shear stresses resisted frictional sliding and extension of the slip zone once cracks were formed. Moreover, the slip zone lengths predicted by the assumption of fully-debonded interphases (by way of the crack density), exceeded the fiber pull-out lengths seen at the fracture surface in the HFC system (Figure 3.3) by a factor of $\approx 2x$. This contradicted the work of [91]. These behaviors stemmed from the BN interphase thicknesses ($\approx 3\mu m$ in HFC specimens), which accounted for an interphase volume fraction of over 25%, and the reduced volume fraction of the matrix ($\approx 33\%$) compared to the matrix volume fraction in LFC specimens $\approx 70\%$.

Although these stipulations rendered the results for HFC specimens more speculative, this exercise was useful for measuring the efficacy of the developed modeling framework in the more model material system in comparison. To quantify the length over which the interface is debonded and sliding occurs, the following calculations were performed, based on the work of Goldberg et al. [92]. The slip zone length l_m was estimated by the function:

$$l_m = \frac{r}{2\tau}\left(\sigma\frac{V_m E_m}{V_f E_c} - \sigma_f^T - \sigma_{deb}\right) \tag{3.10}$$

where σ_f^T was the thermal residual stress on the fiber, σ_{deb} was the critical debond stress, and σ was considered to be the matrix crack saturation stress for HFC specimens $\sigma = \sigma_{sat}$. For this approximation, the matrix volume fraction comprised the combined volume

fractions of the matrix and interphase, while the composite modulus followed a rule of mixtures calculation for the matrix and fiber constituents. It was shown experimentally [76] that debonding primarily occurred at the fiber-interphase surface, which was also observed during fiber push-in testing (Figure 2.2). Consolidation of the interphase into the volume fraction of the fiber or matrix was also applied in the model of [92] to simplify model development.

The critical debonding stress (σ_{deb}) was calculated following the model of Hutchinson and Jensen [16], in which the stresses needed to initiate and propagate the fiber-matrix debonding in the vicinity of a crack were given as:

$$\sigma_{deb} = \frac{1}{c_1}\sqrt{\frac{E_m \Gamma}{r}} \tag{3.11}$$

where Γ was the debond toughness and c_1 was given as:

$$c_1 = \frac{\sqrt{(1-\nu^2)(1-V_f)}}{(2V_f)} \tag{3.12}$$

The thermal residual stress was calculated using the method developed as Chulya et al. [93] as:

$$\sigma_f^T = \frac{-V_m}{V_f}\left[\left(E_m \frac{\Phi_2}{\Phi_1}\right)\left(\frac{E_f}{E_c}\right)\left(\frac{V_f}{1-\nu}\right)(\alpha_f - \alpha_m)\Delta T\right] \tag{3.13}$$

$$\Phi_1 = 1 - \frac{1}{2}\left(\frac{1-2\nu}{1-\nu}\right)\left(1 - \frac{E_c}{E_f}\right) \tag{3.14}$$

$$\Phi_2 = \frac{1}{2}\left(1 + \frac{E_c}{E_f}\right) \tag{3.15}$$

where the Poisson's ratio ν was assumed to be ≈ 0.2 [92], and α_m and α_f were the coefficients of thermal expansion of the matrix and fibers, given as 4.6 x 10^{-6} $^{\circ}C^{-1}$ [86]

and 4.5 x 10^{-6} $^{\circ}C^{-1}$ [94], respectively. The temperature difference during cooling (ΔT) was considered to be 1000 $^{\circ}C$ for all minicomposite systems [5]. The parameters Φ_1 and Φ_2 were elastic parameters obtained from [93]. By Eqs. 3.10 - 3.15, the slip zone length, l_m for HFC specimens was $\approx 80\mu m$, which was later used to compute the slip zone area.

To estimate the area contributions of interfacial debonding and sliding, these areas were first approximated for a single through-thickness crack. It was assumed that all fibers were debonded and slid by l_m along the plane of a through-thickness crack at matrix crack saturation. The slip zone area along the crack plane ($A_{tt}^{l_m}$) was calculated as the fiber circumference (2πr) multiplied by the slip zone length (l_m) and the number of fibers in the tow ($n_{FT} = 500$):

$$A_{tt}^{l_m} = 2(2\pi r \; l_m \cdot n_{FT}) \tag{3.16}$$

where the factor of two accounted for the slip zone area on both sides of the crack.

In the plane of a partial-width crack, it was assumed that the surface progression of the crack reflected its through-thickness progression (as was done for the lower bound). It was also assumed that the fraction of fibers that debonded and slid reflected the specimen global volume fractions (i.e. uniformly distributed fibers). At matrix crack saturation, it was assumed that the slip zone length of the partially-cracked region was also l_m. Slip was expected to occur adjacent to each crack in an identical fashion, such that the slip length adjacent to a crack was the same for all cracks at a given stress. For a crack of length l (Figure 3.1a), the fiber area within the crack front surface area was calculated by multiplying the area of arc ABC (Eqs. 3.4 and 3.5) by the fiber volume fraction (V_f):

$$A_f(l) = V_f R^2 \left(\cos^{-1}(1-x) - x(1-x)\sqrt{\frac{2}{x} - 1)} \right) \tag{3.17}$$

where $x = l/R$. The number of fibers in the partial-width crack wake ($n_f(l)$) was estimated as:

$$n_f(l) = \frac{A_f(l)}{\pi r^2} \tag{3.18}$$

which was the total fiber area in the partial-width crack wake divided by the cross-sectional area of a single fiber (πr^2). This gave the slip zone area in the plane of a partial-width crack at the matrix crack saturation stress ($A^{l_m}(l)$) as:

$$A^{l_m}(l) = 2(2\pi r l_m \cdot n_f(l)) \tag{3.19}$$

where the factor of two accounted for the slip zone area on both sides of the crack plane. The total slip zone area generated at matrix crack saturation ($A_{sat}^{l_m}$) was the sum of the slip zone areas along the plane of all through-thickness cracks (n_{tt}) (Eq. 3.16) plus the sum of the slip zone areas along the plane of p partial-width cracks (Eq. 3.19), each of an individual crack length l:

$$A_{sat}^{l_m} = n_{tt} \cdot A_{tt}^{l_m} + \sum_{i=1}^{p} A^{l_m}(l_i) \tag{3.20}$$

where $A_{sat}^{l_m}$ was assumed to be equivalent to the area of both the debonded region (such that $l_m = l_d$) and sliding region (such that $l_m = l_s$).

The upper bound estimate of the total damage area generated at matrix crack saturation was then:

$$A_{sat}^{upper} = A_{sat}^{lower} + A_{sat}^{l_d} + A_{sat}^{l_s} \tag{3.21}$$

where the region of interfacial debonding and the fiber sliding were equivalent, but were considered separately.

The relationship between the AE energy accumulated up to matrix crack saturation

(AE_{sat}^{T}) and the surface area created using the upper bound calculation was:

$$AE_{sat}^{T} = \lambda^{c} A_{sat}^{lower} + \lambda^{d} A_{sat}^{l_d} + \lambda^{s} A_{sat}^{l_s} \tag{3.22}$$

In the above description, λ^d was the specimen-dependent parameter for AE energy released per unit area from fiber debonding, and λ^s was the specimen-dependent parameter for AE energy released per unit area from fiber sliding. These mechanisms were considered separately as variations in the strain energy released for an instance of each mechanisms were expected (i.e. it was expected that debonding was "louder" than sliding).

It was infeasible to directly quantify λ^d and λ^s for a number of reasons, foremost being that it is not possible to decouple interfacial AE events from the SiC cracking when these mechanisms occur simultaneously over very short time scales and are superimposed onto the same AE waveform. Instead, λ^d and λ^s were indirectly quantified for each specimen. It was hypothesized that the ratio between the cracking coefficients for the matrix cracking and interfacial debonding were equivalent to the ratio of the fracture toughness of the two mechanisms. For CVI SiC, the fracture toughness, $\Gamma_m \approx 14.1\ J/m^2$ [5]. For the debonding mechanism, the average interfacial debond toughness was used, with $\Gamma = 1.2\ J/m^2$ and $\Gamma = 5.5\ J/m^2$ for LFC and HFC specimens, respectively (Table 2.2). For the fiber sliding, it was hypothesized that the ratio between the energy density coefficients for the fiber sliding versus matrix cracking was equivalent to the ratio of the interfacial shear stress and the matrix cracking stress (σ_{cr}^{m}). The matrix cracking stress was estimated using [5, 27]:

$$\sigma_{cr}^{m} = \sigma_o \frac{E_c}{E_m} \left[\frac{1 + \frac{4V_f l_d \Gamma}{(1-V_f) r \Gamma_m}}{1 + \frac{\rho l_d}{r}} \right]^{1/2} - \sigma_m^T \tag{3.23}$$

where σ_o was the composite cracking stress in the no-slip condition:

$$\sigma_o = B\left[\frac{6E_c^3V_f^2E_f}{(1-V_f)^2(1+\nu_m)}\right]^{1/4}\left[\frac{\Gamma_m}{E_m r}\right]^{1/2} \tag{3.24}$$

$$B = \left[\frac{2(1-V_f)^2}{-6\ln(V_f)-3(1-V_f)(3-V_f)}\right]^{1/4} \tag{3.25}$$

ρ was an elastic parameter given as [27]:

$$\rho = \frac{B^2}{V_f}\left[\frac{6E_c}{E_f(1+\nu_m)}\right]^{1/2} \tag{3.26}$$

σ_m^T was the thermal residual stress on the matrix given as:

$$\sigma_m^T = \left[\left(E_m\frac{\Phi_2}{\Phi_1}\right)\left(\frac{E_f}{E_c}\right)\left(\frac{V_f}{1-\nu}\right)(\alpha_f-\alpha_m)\Delta T\right] \tag{3.27}$$

and l_d was the slip zone length calculated for LFC and HFC specimens.

Eq. 3.22 was then rewritten as:

$$AE_{sat}^T = \lambda^c A_{sat}^{lower} + \left(\lambda^c\frac{\Gamma}{\Gamma_m}\right)A_{sat}^{l_d} + \left(\lambda^c\frac{\tau}{\sigma_{cr}^m}\right)A_{sat}^{l_s} \tag{3.28}$$

where λ^d and λ^s were now estimated in terms of λ^c. The expression in Eq. 3.28 was simplified by pulling out the λ^c terms, by which the relationship between AE_{sat}^T and a specimen-dependent parameter that captured the AE energy per unit area released from matrix cracking, debonding, and fiber sliding was derived. For this reason, the term λ^c was replaced with $\lambda^{c,d,s}$ for clarity:

$$AE_{sat}^T = \lambda^{c,d,s}\left(A_{sat}^{lower} + \frac{\Gamma}{\Gamma_m}A_{sat}^{l_d} + \frac{\tau}{\sigma_{cr}^m}A_{sat}^{l_s}\right) \tag{3.29}$$

The $\lambda^{c,d,s}$ term varied between 1.5 - 4.2 $V^2\mu s/mm^2$ and 0.3 - 1.8 $V^2\mu s/mm^2$ for LFC and HFC specimens, respectively. The surface area created by each AE event N based on the upper bound ($A^{upper}(N)$) *up to* the matrix crack saturation stress was calculated as:

$$A^{upper}(N) = \frac{E(N)}{\lambda^{c,d,s}} \tag{3.30}$$

Comparison of Lower and Upper Bound Surface Area Estimates

The estimated surface areas created by each AE event in four LFC and HFC specimens are shown in Figures 3.2 and 3.4 for the lower and upper bound, respectively. The surface area of an average through thickness matrix crack (A_m) is labeled in each plot and shown as a dashed line on the y-axis. Consistently, A_m was calculated to be larger in LFC specimens, due to their $\approx 40\%$ larger cross sections and 100% larger matrix volume fractions.

LFC specimens predominantly generated fewer AE events under tension than similarly sized HFC specimens; thereby, on average, individual events were estimated to create larger surface areas. Assuming only matrix cracking (lower bound), $< 2\%$ of HFC events prior to matrix crack saturation had estimated surface areas exceeding A_m versus $\sim 5\%$ of LFC events (Figure 3.2). In HFC specimens, $< 50\%$ of such large area AE events exceeded 120% of A_m. In contrast, $\sim 65\%$ of such AE events in LFC specimens exceeded 120% of A_m. This observation was corroborated by previous findings that *larger*, through-thickness cracks formed in *fewer* stages in LFC specimens versus HFC specimens (described in Section 2.3.2). The estimates of constituent volume fractions and cross-sectional area in Table 2.1 relied on weighted averages. However, in-SEM observations indicated differences in matrix volume content, and variations in specimen width along the gage in 40-50 μm were common; here, 120% of A_m was used as an upper bound approximation of matrix volume fraction in any local area. As such, AE

events that corresponded to area sizes between A_m and 120% of A_m may have resulted from through-thickness cracking at positions with higher local matrix content (and correspondingly, lower local matrix content for events with estimated size between A_m and 80% of A_m).

The smallest AE events ($\sim 0.0005mm^2$ and $\sim 0.0008mm^2$ for LFC and HFC specimens, respectively), which are also shown for these specimens in Figure 3.2, indicated that the lower bound under-represented the surface areas created by damage events. If AE was only sensitive to the matrix cracking damage mechanism, one would expect to estimate larger damage areas in LFC specimens, as their higher matrix content and 'continuous' matrix microstructure created a more coherent in-plane pathway for crack propagation [61]. Additionally, the smallest AE events were on the order of the surface area created by a few fiber breaks. If one considers the average matrix crack area A_m in terms of fiber size, by dividing A_m by the surface area created by a single fiber break, A_m was equivalent to ∼400 and ∼1100 fiber breaks in HFC and LFC specimens, respectively. While early fiber breaks have been observed in CMCs prior to matrix crack saturation [34] and potentially account for some of these small AE events, it was unlikely that a significant number of matrix cracks would propagate to create areas on the order of a few fibers. Furthermore, given that LFC specimens generated ≈50% fewer AE events than HFC specimens *and* produced twice the crack area, finding smaller events in LFC specimens appeared even more unlikely. These trends motivated the upper bound investigation, where mechanisms other than matrix cracking were considered in order to explain these small AE events.

In the upper bound, the calculated surface areas of AE events in LFC specimens exceeded their lower bound estimates by a factor of ≈ 6x. The difference between HFC specimens was much larger at ≈ 15x the lower bound estimates. The main contributor to this trend in HFC specimens was the high debond toughness (nearly 5x that of LFC

specimens). The potential to overestimate the AE contribution per unit area of debonding in HFC specimens was also a likely factor that requires further investigation. Another factor that contributed to this trend in HFC specimens was the potential to overestimate the slip zone area at matrix crack saturation. If relevant modeling from the literature did not reflect the real debonding and sliding behavior in HFC specimens, this potentially inflated estimate of the slip zone area also skewed the upper bound estimate of the damage accumulation. The largest areas estimated by the upper bound were ∼20x the average through-thickness matrix crack (A_m) in LFC specimens and ∼40x of A_m in HFC specimens. It was likely that some events whose calculated areas exceeded A_m were a result of large matrix crack formation, with significant simultaneous interfacial debonding and sliding captured by AE, the assumed chronology of the upper bound condition. In an analogous approach to Eq. 3.29, the formation area size of an average through-thickness crack whose slip zone extends to its critical limit was approximated by:

$$A_{max}^{upper} = A_m + \frac{\Gamma}{\Gamma_m} A_{deb} + \frac{\tau}{\sigma_{cr}^m} A_{sliding} \tag{3.31}$$

Using the area estimates for the slip zone region found in Eq. 3.16 for the debonding and sliding area, this maximum for a single through-thickness crack was ≈6-7x of A_m in LFC specimens and ≈9-10x of A_m in HFC specimens. While this accommodated most AE events larger than A_m, there were still a portion of events exceeding even these limits. One possibility was that these events reflected multiple matrix crack formation, where near-simultaneous cracking within a small timeframe amplified a waveform's energy. However, more often such high-area AE events were predicted in HFC specimens compared to LFC specimens, which was inconsistent with the understanding that HFC specimens exhibited both smaller accumulated matrix crack areas and slip zone areas at each matrix crack compared to LFC specimens. This finding indicated that the upper bound overestimated

the size of the AE events and therefore the state of damage accumulation. Another potential source of error, however, was that while this model focused on the geometric evolution of damage, it did not take into consideration more nuanced effects. Here, where it was assumed that only damage size dictated the energy of the emitted signal, the simplifying assumption was made that the minicomposite geometry had a fully-densified matrix with no preexisting flaws. However, the size, shape, and distribution of flaws are driven by processing choices, and ultimately those flaws of a critical size that reach a critical stress dictate when and where damage forms [28, 18]. Variations in this nucleation barrier for crack formation may have contributed to differences in energy. This possibility becomes increasingly important when considering that the potential size of flaws in the matrix are much larger than those in the fibers. It was previously hypothesized that the frequency characteristics of fiber breaks were higher than those of matrix cracks [95]. While one supporting explanation for this was that these heightened frequency characteristics came from fiber breaks occurring at higher accumulated strains, another contributor may be that fiber breaks resulting from a distribution of *small* flaws result in high frequencies. A corollary of this possibility is that the lower frequencies that are characteristic of the matrix cracking mechanism are driven by cracks initiating from larger flaws. These hypotheses are the subject of future investigations described in Chapter 5.

In the lower bound, the assumption that only matrix cracking could be captured by AE was used to explore the sensitivity of AE to non-dominant mechanisms, of which there has been limited work [96, 53, 71, 23]. By this assumption, it was found that a significant portion of the produced AE events corresponded to crack areas on the order of a few fiber breaks. It was unlikely, especially given the LFC microstructure, that a significant portion of the matrix cracking AE events would occur in such small propagation steps. Rather, it was hypothesized that these small events were emitted by non-dominant mechanisms that released lower strain energies and created smaller

surface areas, indicating that AE is sensitive to such mechanisms even when they are captured simultaneously with the dominant damage mechanism. It was assumed in this investigation that AE was sensitive either to matrix cracking only, or was sufficiently sensitive to capture simultaneous matrix cracking and interfacial phenomena. However, there remains the possibility that these mechanisms may act independently to generate AE during the specimen lifetime. Future work in this area, described in greater detail in Chapter 5, must aim to either distinguish these mechanisms or confirm their simultaneous occurrence; for modeling purposes, factors such as variations in the slip zone length, non-uniform fiber distribution, and more representative geometries of the minicomposite cross-section and volume must be considered for modeling the damage area. By this preliminary investigation, it is very likely that an accurate measure of the accumulated damage in SiC/SiC minicomposites lies in the envelope between these bounds.

3.3.2 Modeling Damage Beyond Matrix Crack Saturation

Based on the lower bound described in Section 3.3.1, the surface areas ($A^{lower}(N)$) created by AE events in LFC and HFC specimens between matrix crack saturation and failure were estimated as:

$$A^{lower}(N) = \frac{E(N)_{(N>N_{sat})}}{\frac{\Gamma_f}{\Gamma_m}\lambda^c} \tag{3.32}$$

Here, the effect of the variation in fracture toughness between the CVI SiC matrix (reported as 14.1 J/m^2 [5]) and the HNS SiC fibers (calculated as 10.2 J/m^2 from values reported in [97]) was considered. The value approximated for HNS fibers fell within the expected range computed in [75]. The same value for λ^c determined in Domain I was used, as it was expected that the AE was only sensitive to the dominant mechanisms in this scenario. By incorporating the ratio of the fracture toughness, the relationship

found in Domain I was extrapolated to Domain II.

The lower bound on the total damage area generated up to failure (A_T^{lower}) was calculated as the sum of the areas created by all AE events, where N_f was the event at failure:

$$A_T^{lower} = \sum_{N=1}^{N_f} A^{lower}(N) \tag{3.33}$$

For the upper bound, fibers were considered to be debonded (with fully debonded interfaces for LFC specimens and partially debonded interfaces for HFC specimens) by the matrix crack saturation stress. As loading continued beyond matrix crack saturation, it was assumed that fiber breaks were accompanied by fiber sliding adjacent to each break, with this sliding being bounded by the slip zone lengths estimated at the matrix crack saturation stress.

Based on the upper bound described in Section 3.3.1, a relationship similar to Eq. 3.28 was derived for the active mechanisms. However, unlike the relationship in Domain I, it was not feasible to estimate the areas created in Domain II between saturation and failure (given that the number of fiber breaks in the material was unknown). As an indirect solution, the relationship *up to* matrix crack saturation for the two mechanisms active *beyond* this state (SiC cracking and fiber sliding) was instead found, and that estimate for $\lambda^{c,s}$ was applied to events in Domain II:

$$AE_{sat} = \frac{\Gamma_f}{\Gamma_m}\lambda^c A_{sat}^{upper} + \left(\lambda^c \frac{\tau}{\sigma_{cr}^f}\right) A_{sat}^{l_f} \tag{3.34}$$

It was assumed that the ratio of the strain energy release rates between the interface and fiber was approximately equal to the ratio of the interfacial shear stress and the critical fiber cracking stress (σ_{cr}^f). Again the fracture toughness ratio between the fiber breakage and the matrix cracking was included in Eq. 3.34. Callaway et al. [98] found

lubricated bundle strengths of ≈ 2.0 GPa for lubricated bundles of HNS fibers; this value was employed for the critical fiber cracking stress in this approximation.

In this computation, the sliding zone area at the matrix crack saturation stress $A_{sat}^{l_s}$ was calculated by considering the sliding length of fibers once they were broken. For LFC specimens, based on [3], the sliding length adjacent to a fiber break was calculated as:

$$l_f = \frac{r\sigma}{2\tau} \tag{3.35}$$

where σ was considered to be the stress at rupture to estimate the maximum fiber sliding length. This was approximately 160 μm for LFC specimens (or 80% of the sliding zone length estimated in Domain I). For HFC specimens, the sliding zone length of a fiber after fracture (l_f) was considered to be upper bounded by the slip zone length ($l_s \approx$ 80 μm) found in Domain I (Section 3.3.1. It was assumed that there was no extension of the slip zone beyond the matrix crack saturation stress. This was due to both high interfacial parameters that inhibited slip zone extension and the mitigation of stresses at the interface by fiber fracture within the debonded region around cracks. The fiber sliding lengths were taken to be shorter than the slip length l_f in HFC specimens as well, given their higher interfacial shear stress and partially bonded interface; it was therefore approximated in HFC specimens that $l_f \approx 80\%$ of l_s μm, or $l_f \approx 65 \mu m$. These values were applied to compute the sliding zone area following Eqs. 3.16-3.20.

In Eq. 3.36, the difference in contribution for a unit area between the fiber breakage the frictional sliding was again considered. From the previous equation, the λ^c term was pulled, which now was related to the area created both by the SiC cracking and the frictional sliding. For clarity, λ^c was replaced with $\lambda^{c,s}$:

$$AE_{sat}^{T} = \lambda^{c,s}\left(\frac{\Gamma_f}{\Gamma_m}A_{sat}^{lower} + \frac{\tau}{\sigma_{cr}^{f}}A_{sat}^{l_f}\right) \tag{3.36}$$

We find that $\lambda^{c,s}$ varied between 10.1 - 24.0 $V^2\mu s/mm^2$ and 4.3 - 21.0 $V^2\mu s/mm^2$ for LFC and HFC specimens, respectively. The surface area created by each AE event N based on the upper bound ($A^{upper}(N)$) *beyond* the matrix crack saturation stress was calculated as:

$$A^{upper}(N) = \frac{E(N)_{N>N_{sat}}}{\lambda^{c,s}} \tag{3.37}$$

However, it was not particularly useful to estimate the accumulated damage in Domain II in terms of surface area alone. Rather, the following two conditions were considered to describe the damage evolution captured by AE between the matrix crack saturation stress failure to contextualize these areas in terms of the fiber break evolution:

Condition 1: Based on the lower bound (Section 3.3.1), in which it was assumed that AE was only sensitive to the dominant damage mechanisms, it was considered that AE events were only produced by fiber breaks beyond matrix crack saturation. Each break was assumed to produce an area A_f calculated as:

$$A_f = 2\pi r^2 = 0.00027mm^2 \tag{3.38}$$

where the fiber radius (r) $\approx 6.5\mu m$ and two surfaces were created when a fiber failed. The number of fiber breaks that corresponded to the area of each AE event ($N > N_{sat}$) using $A^{lower}(N)$ (Eq. 3.32) was estimated as:

$$N^{lower}_{f,break} = \frac{A^{lower}(N)}{A_f} \tag{3.39}$$

Condition 2: Based on the upper bound (Section 3.3.1), it was assumed that AE events recorded beyond matrix crack saturation captured the energies produced both by fiber breaks and subsequent frictional sliding of fibers. From this, the area created by a

single fiber break was calculated as:

$$A_{f,s} = 2\pi r^2 + 2(2\pi r l_f) \tag{3.40}$$

where the first term accounted for two fracture surfaces created by the fiber break and the second term accounted for the slip zone area on both sides of the fiber break as it pulled out. The number of fiber breaks created by each AE event ($N > N_{sat}$) was approximated then as:

$$N_{f,break}^{upper} = \frac{A^{upper}(N)}{\frac{\Gamma_f}{\Gamma_m} 2\pi r^2 + \frac{\tau}{\sigma_{cr}^f} 2(2\pi r l_f)} \tag{3.41}$$

Again, the effect of the varying AE energy contributions of the two mechanisms relative to the matrix cracking was considered. This is because the sliding zone area around a fiber break was an order of magnitude larger than the surface area created by the break itself, but it was not expected that the strain energy released by the frictional sliding to followed this relationship. By these two conditions, the damage areas created beyond matrix crack saturation were estimated for each specimen in terms of the number of fiber breaks.

Comparison of Fiber Break Distribution Estimates

The trends observed at all conditions indicated that most AE events beyond matrix crack saturation were small relative to the size of the AE event(s) generated at failure. This finding was consistent with the current understanding of how fiber bundles fail [99, 84, 25, 22]. Often, failure occurred not at the ultimate tensile stress (UTS), but upon further applied displacement that led to a short cascade of fiber breaks, resulting in a slightly lower stress prior to the full tow rupture.

The evolution of fiber breaks per AE event as a function of stress is shown in Figure 3.5 for Conditions 1 and 2 described above. It was found that most AE events were generated by several fiber breaks occurring in small quantities prior to tow rupture. The dashed horizontal line in each sub-figure represents the fiber tow size (500 fibers). Over 500 fiber breaks were predicted for all specimens at both conditions, in agreement with [25], who found that fibers failed more than once by sliding to recover previously carried stress via x-ray microtomography (μCT) and estimated a total break count of $\sim$750 fiber breaks per specimen. The specimens in [25] had the same fiber type and number of fibers as those in this dissertation, with different interfacial properties. The fiber break count of [25] should be considered a substantial under-prediction due to the high potential for undetected fiber breaks, such as from the μCT resolution of $\sim 1\mu m$. Chateau et al. [25] also demonstrated that fibers may break multiple times near the fracture zone, as a decay in fiber break density was observed away from the fracture plane; high-densities of near simultaneously occurring fiber breaks in the rupture zone would be infeasible to capture due to the spatial and temporal resolution limitations of current experimental capabilities.

For each specimen at both conditions, at minimum one event (or multiple, closely spaced events with a similar combined size) was found that corresponded to a fiber fracture estimate exceeding the tow size. This was expected given that at the rupture state, broken fibers can rapidly be reloaded and break again in the time window of a single AE event.

For Condition 1, where it was assumed that AE was only sensitive to the fiber failure mechanism, the higher fiber break count was estimated, with $\sim$8200 (corresponding to $\approx$16 breaks/fiber) and $\sim$7800 ($\approx$15 breaks/fiber) fiber breaks in LFC and HFC specimens, respectively. For Condition 2, where it was assumed that AE was sensitive to the simultaneous occurrence of fiber breaks and subsequent sliding, $\sim$5200 (corresponding

to ≈10 breaks/fiber) and ∼5900 (corresponding to ≈12 breaks/fiber) were estimated in LFC and HFC specimens, respectively.

It was useful to compare the outcomes of the aforementioned conditions to modeling predictions of the total number of fiber breaks at the ultimate tensile strength (UTS). This helped to contextualize the validity of the modeling outputs. Curtin [3] approximated the fraction of broken fibers in the wake of a crack at the UTS as: *q = 2/(m+2)*, where m was the Weibull modulus describing the variability in fiber strengths. From [3], the total number of fibers broken was estimated as:

$$f_{broken} = (q \cdot n_c + (1 - q)) \cdot n_{ft} \tag{3.42}$$

where $n_{ft} = 500$ fibers, and n_c referred to the total number of matrix cracks. The first term in Eq. 3.42 accounted for the portion of the tow broken at each matrix crack prior to failure, and the second term accounted for the portion of unbroken fibers near the plane of the failure crack breaking at the rupture stress. For Hi-Nicalon Type S^{TM} SiC fibers, there were reported measurements of the Weibull modulus in the range of m = 4.49 – 8.42 [100, 98, 101]. If this range was considered as the bounds for q, it was found that q = 0.22 - 0.31. This led to an estimated range for the total number of fibers broken at the UTS for LFC specimens as 3250 – 5000 fibers and for HFC specimens as 4400 – 6800 fibers. While Condition 1 (in which it was assumed that AE was only sensitive to fiber breaks) starkly overestimated the predicted total based on [3], the estimates by Condition 2 overlaid well with these ranges.

A primary conclusion is that AE *is* sensitive enough to capture the combined effects of dominant and non-dominant mechanisms. Moreover, when a reasonable estimate of the accumulated damage area is inputted, a predicted fiber break evolution matching the micromechanics-predicted evolution results. That is, point by point AE information likely

contains meaningful information both indicative of the damage mode, as well as the size of that damage source. However, one factor to consider to consider in future investigations is that a small portion of fiber breaks occur below the matrix crack saturation stress [34], which was not accounted for in this model.

It is also important to note that though these conditions only consider the fiber break and sliding activity in Domain II, other mechanisms were active. In-SEM, mixed-mode rupture events (where fragments of the matrix fractured when the tow failed, shown in Figure 3.6) were often observed. Fiber tow rupture in conjunction with this additional matrix cracking would near-certainly contribute to the creation of $\geq$500 fiber fracture surfaces. Therefore, it is possible that AE events pre-rupture, which occurred with estimated areas exceeding the tow size, also captured additional subsurface matrix cracking. Quantifying the areas created by the additional matrix cracking, whether the damage mechanism was surface observed (as in Figure 3.6) or subsurface, is infeasible by SEM measurements alone and requires further exploration.

One possible source of error to consider in future investigations is waveform attenuation, which increases as damage accumulates, and is related to elastic material parameters, number of cracks, and the degree of crack opening [79, 57, 102]. Maillet et al. [57] found an increase in peak frequencies and frequency centroids with stress, which may indicate the transition between a matrix cracking vs. fiber break dominated response. It is unclear whether this increase in frequency characteristics is due to increased signal attenuation with accumulated damage, or whether damage mechanisms at higher stresses (i.e. fiber breaks) have higher characteristic frequencies. This is because the frequency characteristics of an event, which are related to the stored strain energy released by its occurrence, may be mechanism independent. Let us consider the example of two fibers breaking at different strains that create equivalent surface areas. The fiber break at higher strains has more stored strain energy but its released signal is more damped than

the fiber break at lower strains, as its AE must propagate through a greater amount of accumulated damage. The degree to which these competing mechanisms offset or negate each other requires further study. However, their combined effect is likely minimized at lower strains, given the linear relationship between accumulated AE energy and damage area during the matrix cracking dominated response [34].

In this work signal attenuation was not measured, as this quantification typically relies on factors that are difficult to control (e.g. sensor coupling to specimens). Morscher et al. [79] used lead breaks to measure waveform propagation between sensors but found lead breaks to be inconsistent sources. Maillet et al. [102] studied variations in thousands of recorded waveforms in increments of time and space, in order to quantify the attenuation coefficient evolution. A method such as acousto-ultrasonics (AU), in which artificial sources produce waveforms, could be leveraged in-SEM to quantify the initial signal loss and measure progressive attenuation. This approach has previously been used in conjunction with AE to study damage modes in CMCs [23]. Another potential source of error is the AE transducer sensitivity. Recent work by Guel et al. [72] shows that AE transducers with overlapping broadband frequency ranges vary in sensitivity to certain frequencies. As such, AE data acquired using a single sensor type may be blind to certain frequencies (and thereby a portion of the total energy) of the originating damage sources, leading to an underestimation of the damage accumulation. In such a scenario, the error can be mitigated using a similar approach to Guel et al., wherein two sensor types with varying frequency sensitivities are used to assess the damage accumulation [72].

3.4 Summary

The relationship between damage sources and their corresponding AE events in SiC/SiC minicomposites was modeled using insights gained from combined in-SEM ten-

sile testing and AE measurements. Damage progression was estimated over two domains: Domain I, up to the matrix crack saturation; and Domain II, between matrix crack saturation and specimen failure. While prior efforts assumed that only dominant damage mechanisms (matrix cracking and fiber failure) can be captured by AE, as they have higher strain energy rates than secondary mechanisms such as fiber debonding and sliding, it was found that secondary mechanisms are also captured by AE.

We analyze Domain I using a lower and upper bound assumption: the lower bound assumes that AE is only sensitive to capturing matrix cracking, while the upper bound assumed that AE can capture the near-simultaneous occurrence of matrix cracking, fiber debonding, and fiber sliding in the vicinity of the crack plane. The lower bound resulted in unrealistically small crack areas in both LFC and HFC specimens, where the smallest AE events were on the order of the fracture surface area of a few fibers. It was hypothesized that the smallest (lowest energy) AE events were likely the result of non-dominant mechanisms, which had lower strain energy release rates than the SiC cracking. The upper bound likely overestimated the areas created, in part due to the potential for overestimating the slip zone area and the energy contribution of debonding relative to matrix cracking.

In Domain II, the number of fiber breaks per AE event between matrix crack saturation and failure were estimated by the following conditions: (i) where AE was only sensitive to the SiC fiber fracture mechanism (based on the lower bound in Domain I); and (ii) where AE was sensitive to the combined mechanism of fiber fracture and subsequent fiber sliding (based on the upper bound in Domain I). For all specimens by both conditions at least one AE event (or several AE events occurring near-simultaneously) was found at failure stresses where the predicted number of fiber breaks exceeded the tow size. Condition 1 likely overestimated the fiber break evolution (with ≈8200 fiber breaks in LFC specimens and ≈7800 fiber breaks in HFC specimens), while values pre-

dicted by Condition 2 (≈5200 fiber breaks in LFC specimens and ≈5900 fiber breaks in HFC specimens) overlaid well with the expected number of fiber breaks predicted by [3]. Through in-SEM monitoring, tow rupture was accompanied by additional matrix cracking was observed at specimen failure, and was therefore assumed to be captured in AE in both conditions. As a result, Condition 2 may still slightly overestimate the fiber break evolution. The degree to which matrix cracking contributed to the AE accumulated beyond matrix crack saturation, and a more accurate characterization of the slip zone area created by secondary mechanisms in Domain II, requires further study. It is likely that the more representative model of damage accumulation in LFC and HFC specimens follows Scenario 2, where AE is sensitive to both dominant and non-dominant damage mechanisms. However, further work is needed to characterize the energy density contributions of the secondary mechanisms in order to more accurately map the damage accumulation.

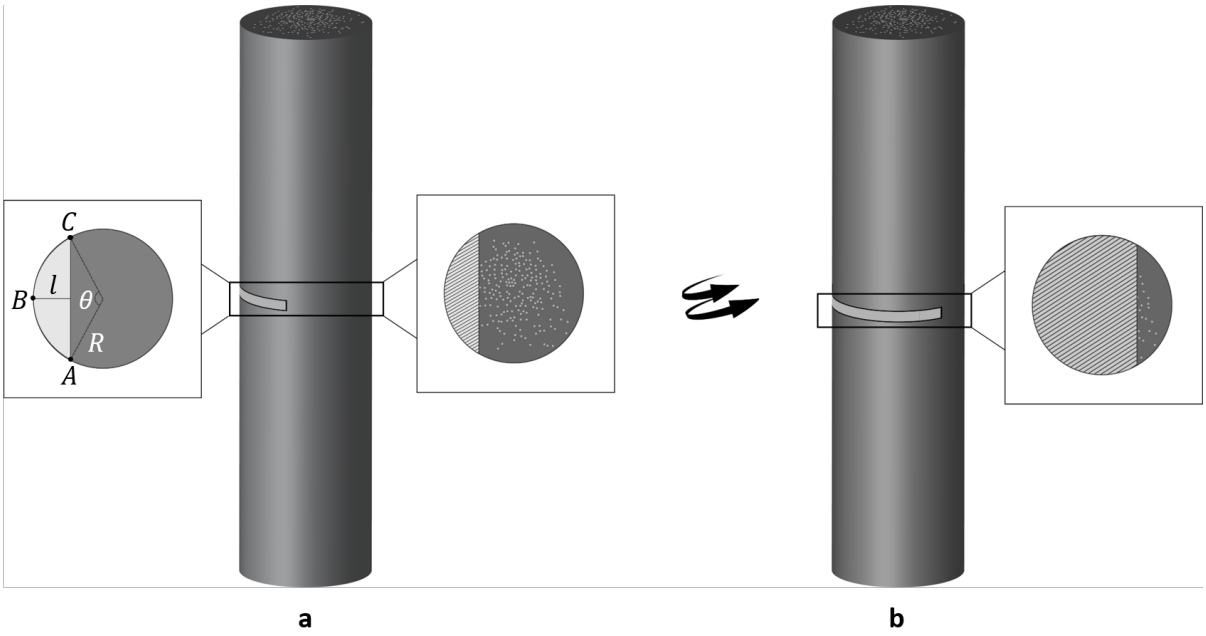

Figure 3.1: **a)** Schematic of the minicomposite cross-section showing a partial-width crack (Orientation 1). In **b)** the sample is rotated such that the partial-width crack appears as nearly through-width (Orientation 2)

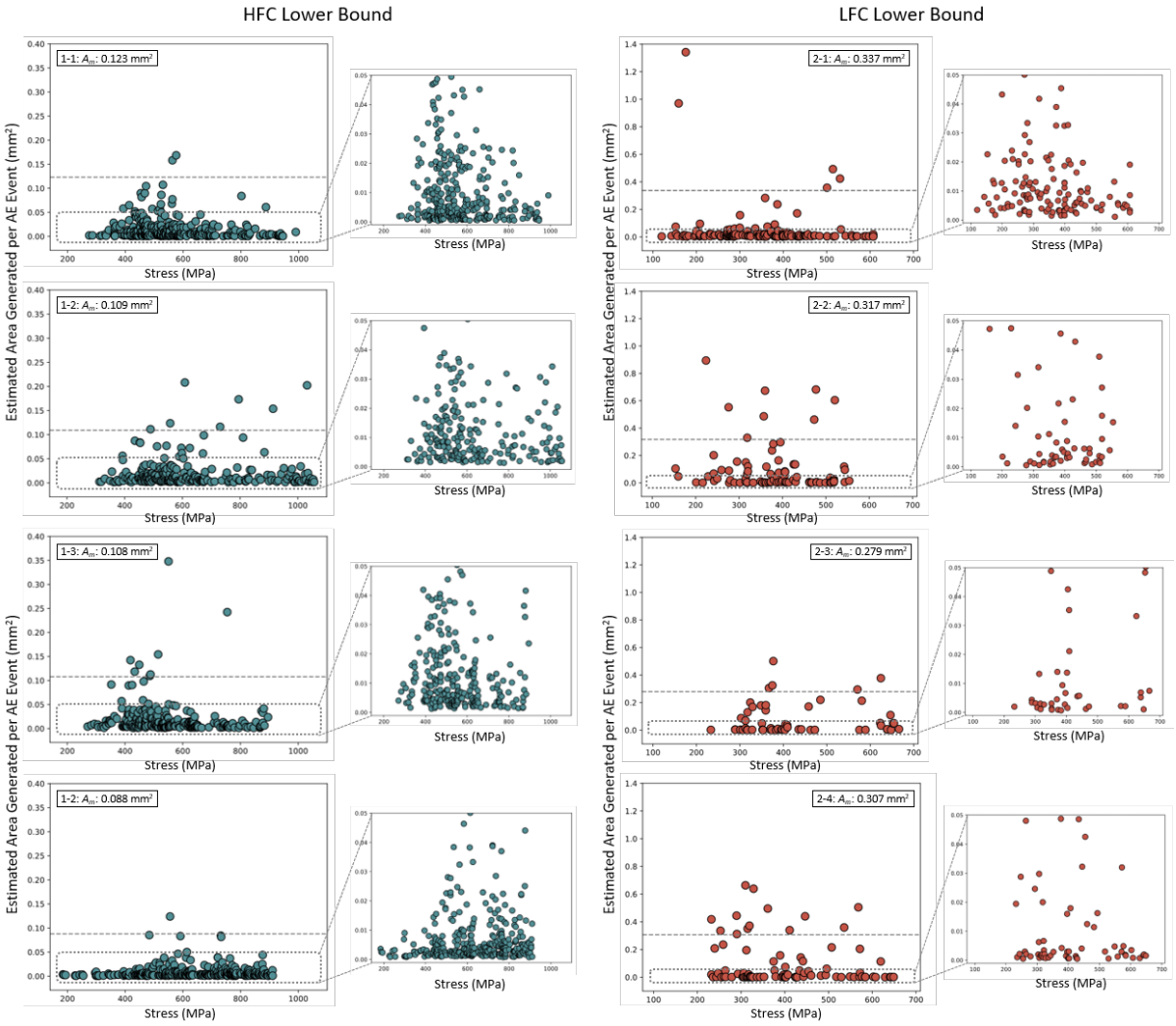

Figure 3.2: The distribution in surface areas created per AE event of four HFC and LFC specimens, mapped as a function of stress based on the lower boundary conditions, which under-represents the damage areas.

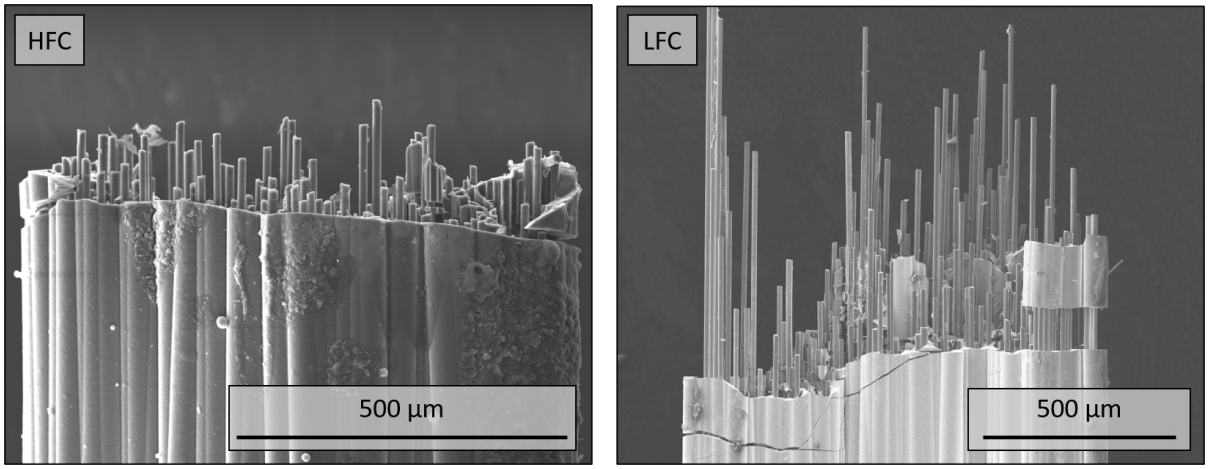

Figure 3.3: HFC and LFC specimen fracture surfaces showing fiber pullout.

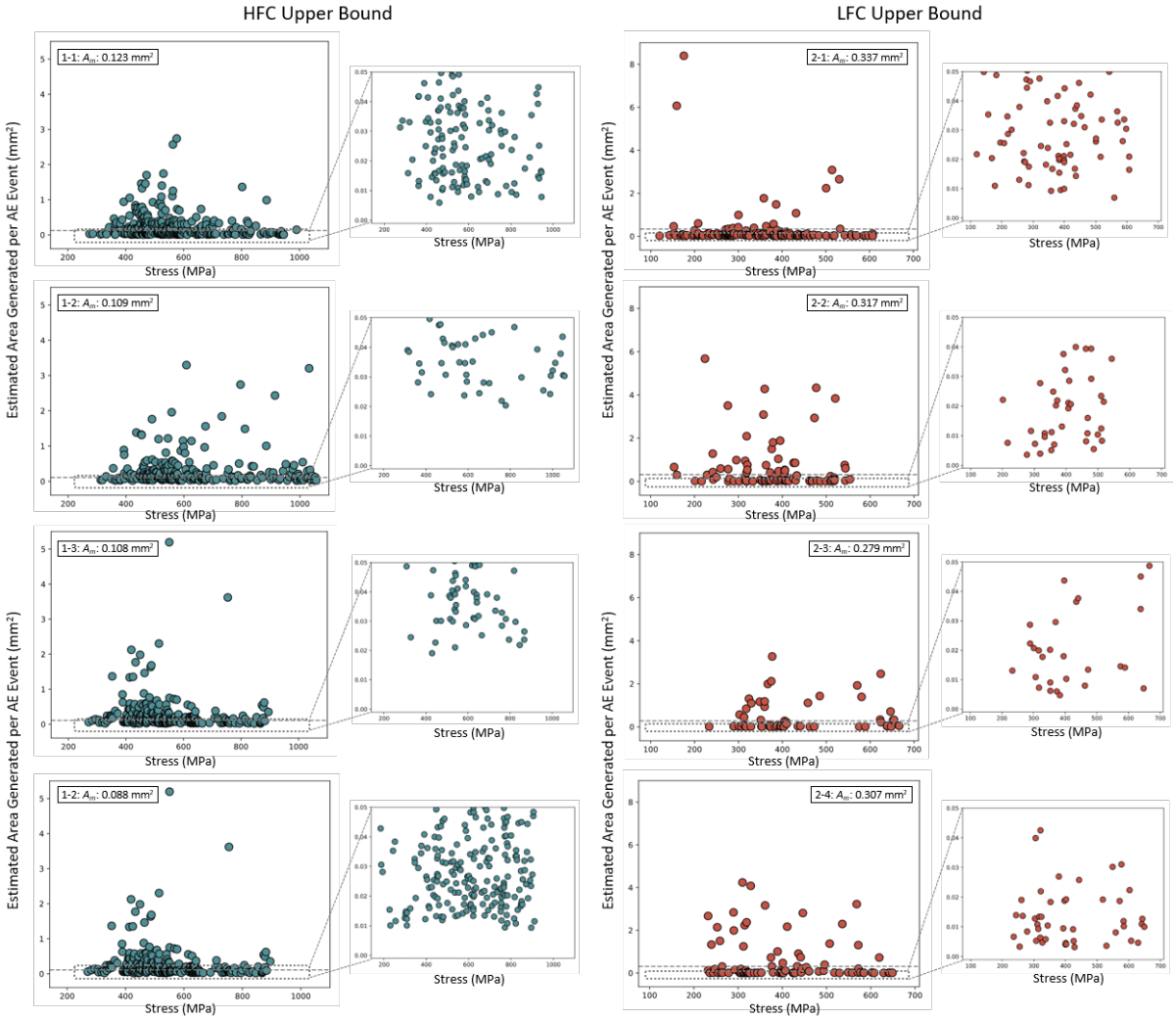

Figure 3.4: The distribution in surface areas created per AE event for four HFC and LFC specimens, mapped as a function of stress based on the upper boundary conditions, which likely overestimated the damage areas.

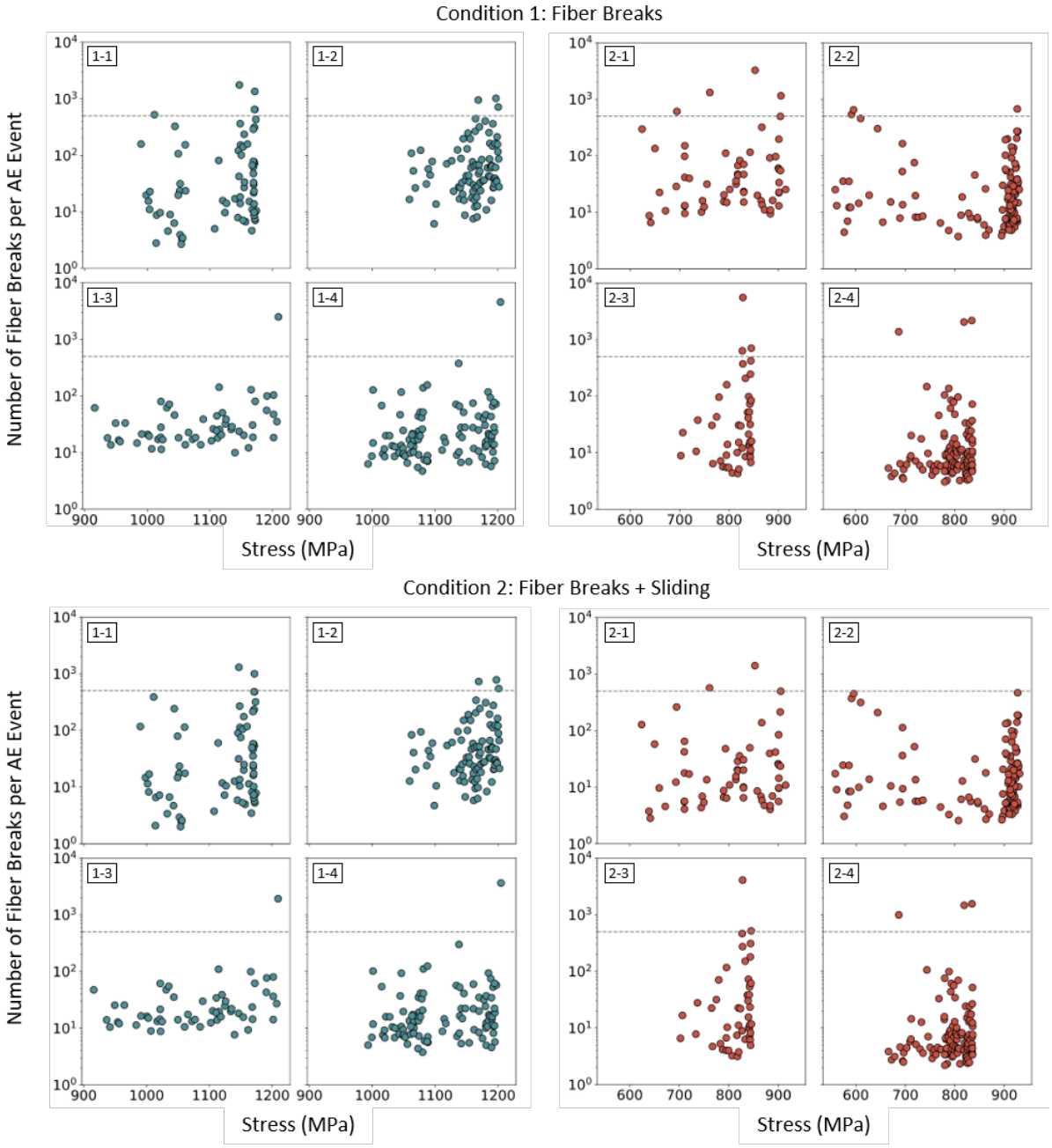

Figure 3.5: Estimated number of fiber breaks per AE event for all specimens at 2 conditions. The dashed horizontal line represents the fiber two size (500 fibers).

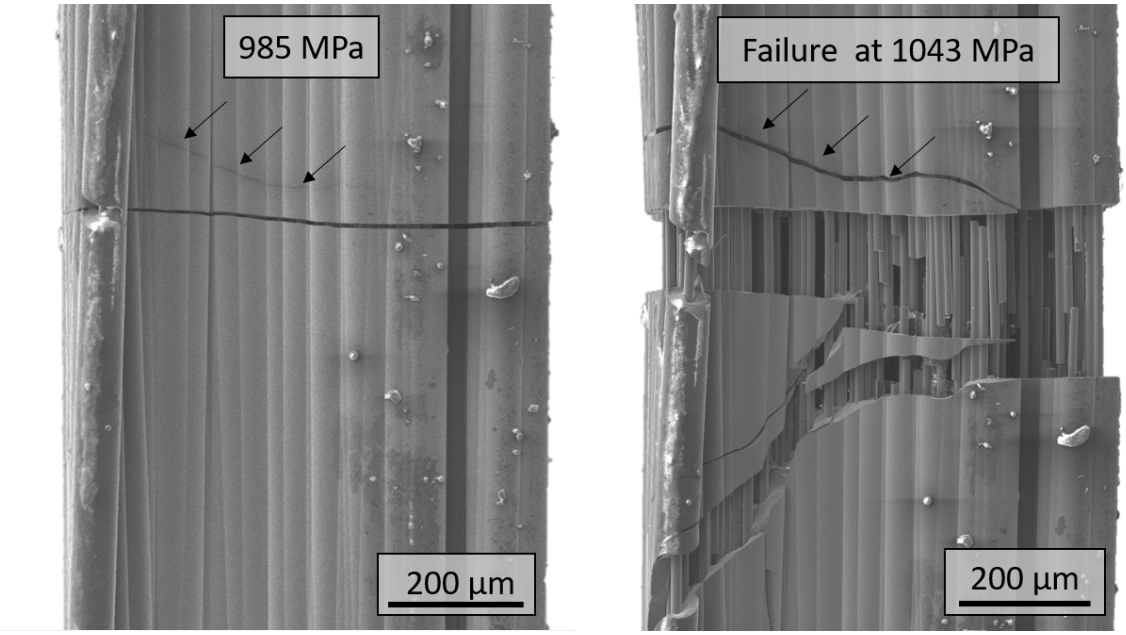

Figure 3.6: Mixed-mode fracture events occurred with fiber tow rupture. The surfaces created by these events contributed to the energy of the rupture AE event, but are infeasible to quantify.

Chapter 4

In-SEM Characterization of Crack Opening in SiC/SiC Minicomposites

4.1 Scope

In this chapter, transverse matrix crack opening displacements (CODs) in SiC/SiC minicomposites are characterized as a function of stress via tensile testing in-scanning electron microscope (SEM). The objective of the investigation described in this chapter was to: (i) understand the relationships between crack opening and microstructure; and (ii) evaluate the efficacy of well-established micromechanics-based models for representing the experimentally-captured crack opening behavior.

The degree of matrix crack opening is primarily dependent on constituent parameters and applied stresses. In the wake of a matrix crack, frictional forces exerted by the fibers on the matrix resist crack opening and crack extension [13, 66]. Under continued axial loading, cracks open when local stresses exceed these resisting interfacial debond and shear stresses. The relationships between constituent properties and stresses on the matrix crack opening behavior are explored in this chapter. Herein, the *in situ*

characterization of matrix crack opening is leveraged to explore the hypothesis that there are microstructural features existing from the onset of loading that drive damage accumulation and failure.

Experimentally-obtained CODs were compared to CODs of two models: (i) the seminal model of Marshall et al. [66, 1], which provides a theoretical framework that describes the evolution of crack openings based on traction laws, and is used for order of magnitude estimates of CODs; and (ii) a newer model by Yang et al. [2] in which COD is based on Hutchinson and Jensen [16] with an additional accounting of the effect of an initially-bonded interface and the thermal residual stresses in the fiber. How well models predicted crack opening behavior was found to depend principally on two elements: the (i) consideration of the progressive nature of fiber failure prior to specimen failure and (ii) variations between the initial crack opening rate (upon matrix crack formation) and the subsequent crack opening rate (upon continued axial loading). These findings motivated the evaluation of a third model, from Chateau et al. [4], that accounts for element (ii) and was found to produce significantly closer COD estimates. The findings of this chapter support the improvement and validation of predictive models in which matrix crack opening is a key feature.

4.2 Methods

4.2.1 COD Measurements via Image Processing

Incremental tensile loading in-SEM (described in Section 2.2) was used to capture the evolution of matrix crack opening at a statistically significant number of cracks across several load states. An example of an evolving crack captured in-SEM is shown in Figure 4.1. Such high-resolution micrographs can be used to measure CODs manually, but this

is prohibitively time consuming; furthermore, without a precise method to document crack opening measurements at the same positions along the crack length at each load state, the resulting CODs may not accurately reflect the average behavior of a crack. Here, an automated approach is presented to expedite this process and provide resolved COD measurements along the crack length across load states.

To computationally identify and measure the distances between the two faces of a crack (shown in Figure 4.2a), an edge detection approach from [103] was adapted. A median filter of kernel size 3 was applied to an SEM micrograph and normalized using the median pixel value of the blurred image. A Sobel convolution in the y-direction was performed on the blurred and normalized image. The median normalized pixel value along the scan line (Figure 4.2b) and the median normalized image gradient along the same scan line (Figure 4.2c) were plotted. If at any point the normalized pixel value was lower than a set threshold (shown by the line in Figure 4.2b) and the normalized image gradient exceeded the set upper and lower thresholds (shown by the two lines in Figure 4.2c), then the top edge of the crack was measured as the location at which the image gradient was at a maximum and the bottom edge was determined as the location at which the image gradient was at a minimum.

Scan-lines were taken in the y-direction of the micrograph for every column of pixels. Each scan-line was divided into 100-pixel length scan segments (e.g. for a 4096 x 2048 field of view 4096 scan lines were taken across the sample length with (4096/100) x 2048 equal to 83,800 scan segments for that micrograph). This scan segment length was selected such that only a single crack, if at all, appeared in each scan segment. This approach was applied to a training data set of micrographs, where crack locations were known, to optimize upper and lower thresholds to minimize false positives (i.e. the mis-identification of a non-crack feature). For this, the algorithm was run with varying thresholds on an array of frames, to determine the existence and location of a crack in

each frame.

The spatial resolution of the crack width (detection of the crack edges) by this method was on the order of 350 nm (nearest-pixel resolution), binning crack widths into discrete multiples of the pixel resolution. To achieve a more continuous measure of the crack width, an interpolation method described in [104] was used. For a single scan segment (such as that shown in Figure 4.2b), two quadratic polynomials were fit to the pixel gradient value (shown for six data points in Figure 4.2c). The first was fit to the negative pixel gradient values, including the minimum of the pixel gradient, and the other was fit to the positive pixel gradient values, including the maximum of the pixel gradient. The extrema of each quadratic polynomial was found, and these defined the top and bottom edge of the crack for that scan segment, respectively. As only one crack was captured in each scan segment, only a single maximum and minimum was found. The extrema of each scan segment were logged as potential candidates for the bottom and top edges of a crack.

False positives were largely a result of the SiC matrix surface texture, which was observed as darkened areas during beam rastering. Outliers were infrequent (with fewer than 0.5% of all points identified by the algorithm) and were easy to identify as they were spatially isolated from true positives, such that they usually occurred far away from neighboring cracks. True cracks measured were typically through-width (minicomposite sample widths of 800-1200 µm). In contrast, outliers were short (typically smaller than 300 µm) and did not grow with increased globally applied stress, making them further discernible. Crack splitting from a primary matrix crack was also observed in both systems of minicomposites. In such instances, the split area of the crack was ignored in the consideration of COD, and only the crack opening at the transverse portion of the through-thickness matrix crack was measured. Examples of such outliers are shown in Figure 4.3.

An efficient and robust solution to filter noise (e.g. due to false positives, split cracks, or other irregularities) was to implement a novel algorithm allowing for rapid but manual crack verification and adjustment. As each crack was detected and its opening measured, it was plotted and displayed with its measured opening. A command line interface allowed the user to approve, adjust, or reject each crack in order to manually filter noise on the basis of a visual inspection of the plot, and/or the measured opening. This allowed for rapid noise filtering while preserving a large degree of automation; this functionality can be disabled if desired.

To group the points representing the crack faces to correspond to individual cracks, a k-means algorithm was used to cluster the points based on y-position. An optimal number of clusters (k) was chosen based on the number of cracks observed in each micrograph panorama generated in-SEM (in Figure 4.4, k=*2* at load state 1, k=*7* at load state 2, etc.), based on minimization of the Davies-Bouldin Index [105]. This clustering method enabled the conversion of a point cloud of crack opening measurements for a single micrograph panorama into a set of labeled COD data associated with individual cracks. Points which fell beyond 1.5x the interquartile range of all crack face distances from the crack centroid value were then removed as outliers.

At the final step, each automatically identified crack was tracked across load states using a rapid process incorporating visual confirmation, as follows. The end result of this identification is schematically shown in Figure 4.4. At each given load state, cracks were automatically identified, and each assigned a unique identifier label (i.e. Crack 1, Crack 2, etc.). These automatically identified cracks were then mapped from one load state to the next based on their centroid positions (such that Crack 1 in load state 1 was identified as Crack 4 in load state 2, if numbered from the top of the micrograph panorama). If a crack was found to be in close proximity to the centroid value in a previous load state and of similar shape to a previously-identified crack, its identifier numbers were linked. If

a crack centroid value did not correspond to those of any identified cracks in the previous load state, it was identified as a new crack and given a new identifier number. This process was carried out across all imaged load states. The reason that this process could not be automated is due to issues in the automated identification of a crack across load states, which mainly stemmed from the automated stitching feature of the MAIA3 SEM, where a crack was sometimes obstructed through edge distortions; such cracks were excluded once detected. Both the horizontal and vertical position of a crack changed across load states as a result of strain accumulation in the material, variations in the measurement resolution, and image stitching; these issues prevented unsupervised clustering of crack centroid values across load states. However, these were largely mitigated by the forward crack identification method described here, as the spacing between crack centroids were fairly consistent across load states even when the absolute values of these centroids were not. Repeat measurements performed on multiple cracks resulted in small deviations in COD measurements ($<0.1\%$).

There were limitations on the size of cracks that could be measured by this algorithm. Some observed cracks in HFC and LFC specimens formed with initial crack openings near the size of the pixel resolution. The majority of such cracks formed near the ends of the gage, and typically did not open at higher stresses (these could be thought of as hairline cracks in the matrix). Some cracks nearer to the gage center also formed with small CODs, typically at the earliest load states. Though these CODs could not be accurately resolved by the algorithm at their emergence, they were measurable at higher load states. For measurement consistency, these cracks were not included in the present analysis. The CODs measured by this automated framework were compared with manually measured CODs using the imageJ software package for cracks in an HFC and LFC specimen. Approximately 30 point measurements of the crack opening across the crack length was captured for each crack measured by the algorithm. These measurements correlated with

$r = 0.97$.

4.3 Results

4.3.1 COD Measurements from in-SEM Observations

Using the edge detection and clustering approach described in Section 4.2, crack opening displacements (CODs) were measured for observable matrix cracks in the LFC and HFC specimens. As shown in Figure 4.5, the earliest quantified CODs were 800 nm in LFC specimens and 600 nm in HFC specimens. One explanation is that LFC specimens exhibited a higher initial crack opening rate due to lower fiber volume fractions and reduced ability to apply bridging tractions to larger evolving cracks. Additionally, the lower debond toughness found in LFC specimens ($\Gamma = 1.2 \pm 0.5$ J/m^2) versus HFC specimens ($\Gamma = 5.5 \pm 3.9$ J/m^2) [61] corresponded to larger predicted debond lengths in LFC specimens. In HFC specimens, this value for Γ was approximately half of the fiber fracture toughness (10.2 J/m^2 based on [97]). He et al. [106] found that the likelihood of crack deflection decreases as the ratio between the fracture energies of the interface and fiber exceed $\approx 1/4$, inhibiting debonding and promoting early fiber fracture. The reduction in debond lengths in HFC specimens based on [106] given a tough interface (which is also estimated by models in Chapter 3), likely prevented crack opening to the degree seen in LFC specimens, where crack deflection and debonding were promoted by a weak and compliant interface. This was further evidenced by larger matrix fragment lengths (lower crack density) quantified throughout the stress response of LFC specimens compared to HFC specimens [61]. Though smaller cracks than those presented in Figure 4.5 were observed in both systems, these cracks did not grow once formed and were rarely the positions where the specimen failed. Cracks on the order of the pixel resolution more

commonly formed near the grips.

A distribution in CODs was observed in both systems (Figure 4.5), in agreement with previous work by Sevener et al. [22], due to local stresses, microstructural characteristics (e.g. local distribution of fibers and corresponding bridging capability), and constituent property effects (e.g. variations in sliding stress). In comparison to HFC specimens, LFC specimens exhibited a broader distribution of CODs, which widened over the loading profile up to the failure stress. After the onset of major matrix cracking, this trend was likely due to increased debonding and sliding in the matrix crack wake due to globally lower interfacial properties in LFC specimens.

In LFC specimens, the improved ability to activate non-dominant mechanisms (Chapter 2) mitigated premature fiber failure, allowing for larger cracks to accommodate locally higher stresses. More compliant BN interphases facilitated more effective load transfer between the fibers and matrix. Once matrix cracks propagated across the specimen cross-section to through-thickness, these cracks opened under an axial load leading to strained fibers in the crack wake. Debonding was required to accommodate the crack opening and mitigate locally high stresses on fibers, thereby reducing the risk of premature fiber failure. One observation from these experiments is that the eventual failure crack initiated relatively early in the damage response of material, in conjunction with the formation of significant matrix cracking at stresses above the material PL. Once formed, these matrix cracks accumulated more underlying damage and evolved to become more probabilistic locations for failure. Further study is needed to understand this phenomenon. It was also observed that the cracks with the largest openings (including the failure crack), occurred relatively far from their neighboring cracks (between 500 and 700 μm) compared to the average crack spacing at matrix crack saturation ($\approx 400\mu m$) [61]. This observation is consistent with findings reported for minicomposites by Chateau et al. [4], who hypothesized that these largest cracks behaved analogous to isolated cracks.

In LFC specimens, significant fiber failure likely only occurred when secondary mechanisms such as debonding were exhausted, which is supported by estimates of fully-debonded interfaces at matrix crack saturation in Chapter 3. Once broken, fibers were able to pull-out and recover a portion of their previously carried stress through fiber bridging, as was experimentally observed by Chateau et al. [4]; the stress due to an initial fiber break was redistributed to all intact fibers in the plane of the crack due to global load sharing. Based on our current understanding of how fiber bundles fail [83, 91], initial fiber breaks were a result of randomly distributed flaws within the fiber tow that reached a critical cracking stress. Based both on an observation of AE activity predominantly occurring in the plane of already formed cracks after matrix crack saturation (Figure **??** and high-energy AE activity occurring at the largest cracks, it is likely that most fiber breaks occurred in the vicinity of cracks with the largest openings, where the underlying fibers experienced the highest strain accumulation. Close to failure, fiber breaks coalesced at the dominant crack location, which is consistent with the AE observations of Chapter 2. As denoted in Figure 4.5, the failure crack in LFC specimens typically exhibited one of the largest CODs at failure.

In comparison, at elevated stresses the drivers of crack opening in specimens with a lower matrix content and a strongly-bonded interface (HFC) appear to be independently-occurring interfacial phenomena, rather than fiber breakage. As shown in Figure 4.5, a smaller distribution in CODs was observed in specimens with a lower matrix content and smaller cross-sectional area (HFC), which was the result of multiple, interconnected phenomena. First, a higher fiber content initially bridged smaller matrix cracks, preventing them from opening to the degree observed in LFC specimens (i.e. lower initial crack opening rate). Secondly, when initial fiber breaks occurred, there was an uneven redistribution of stress to intact fibers in the plane of the crack due local load sharing, which enabled continued crack bridging. This was made possible by a more hetero-

geneous distribution of fibers (Figure 2.1). Finally, when fibers broke, they could be reloaded through fiber bridging near the initial break, due to smaller sliding lengths resulting from higher interfacial parameters. At the failure location, the effects of these combined phenomena was a COD trend that was indistinct from the behavior of other evolving matrix cracks, unlike the failure crack trend observed in LFC specimens. While Figure **??** showed an uneven distribution of damage events (presumably, fiber breaks) at matrix crack locations beyond the matrix crack saturation stress from AE, the COD trends observed here did not appear to depend on where fibers began and continued to fail.

4.3.2 Modeling of CODs

The CODs of unidirectional CMCs (including minicomposites) subjected to tensile load have been previously modeled [2, 1, 16, 14, 87]. These models often make simplifying assumptions about the CMC architecture, including uniformly distributed fibers, thin interphases, and global load sharing. The first of these assumptions is broken by both LFC and HFC minicomposites (and, typically CMCs in general). The second is broken by HFC specimens, whose interphases exceed $2\mu m$ in thickness. The third constraint is also inconsistent with the investigated minicomposite microstructures; as shown in Figure 4.6 for both LFC and HFC specimens, fibers were not evenly distributed in the material cross-section. As a result, closely spaced groups of fibers shared interphase coatings, and some fibers were even in direct contact with one another. This heterogeneous distribution of fibers likely contributed to variations in load sharing within the material, which influenced crack opening trends [4].

In spite of these inconsistencies, it is worthwhile to evaluate the efficacy of models for representing the real damage behavior, as these models contribute to guidelines for use.

For this analysis, two models in the literature were first considered.

The model developed by Marshall et al. [1] was primarily focused on unbonded CMCs, where sliding of the matrix over fibers was *only* resisted by frictional forces at the interfaces. For a purely frictional fiber-matrix bond, the sliding distance was determined by the length over which the interfacial shear stresses exceeded the frictional stress τ. An estimate for the COD was given therein as:

$$\delta = \frac{r\sigma^2}{4\tau V_f^2 E_f (1 + \frac{E_f V_f}{E_m(1-V_f)})} \tag{4.1}$$

where σ was the closure pressure, and $\tau = 18.1 \pm 4.8$ MPa for LFC specimens and $\tau = 34.5 \pm 13.0$ MPa for HFC specimens. Though the minicomposite systems studied in this dissertation initially have a physical interphase, given the possibility of fully-debonded interphases at matrix crack saturation (or at any other point), continued crack opening at higher applied stresses would primarily be driven by overcoming the frictional resistance. This understanding motivated exploration of this model's predicted COD behavior. For LFC specimens, it was approximately true that $V_m \approx 1 - V_f$; for HFC specimens, this expression consolidated the interphase volume fraction into that of the matrix, as was done previously for modeling considerations in Chapter 3.

The second modeling approach from Yang et al. assumed that once matrix cracking initiated, there was concurrent interfacial debonding and sliding in the crack wake [2]. In the slip zone region flanking each crack plane, there was inconsistent matrix and fiber deformation. It was assumed that the matrix contracted along the fiber direction against the crack plane, while fibers extended as a result of continued axial loading. Therefore, the crack opening displacement was approximated as the sum of the displacements from

the matrix shrinkage and fiber extension given therein as:

$$\delta = \frac{r(1-V_f)E_m((\sigma+\sigma_{th})^2-\sigma_d^2)}{2\tau V_f^2 E_f E_c} \tag{4.2}$$

where σ was the applied stress and σ_d was the critical debond stress, which was estimated by Budiansky et al. [27, 85] as:

$$\sigma_d = 2V_f\sqrt{\frac{E_f E_c \Gamma}{(1-V_f)E_m r}} \tag{4.3}$$

where Γ was the debond toughness.

In Eq. 4.2, the thermal residual stress (σ_{th}) was estimated following the method developed by Chulya et al. [93]:

$$\sigma_{th} = \frac{-(1-V_f)}{V_f}\left[\left(E_m\frac{\Phi_2}{\Phi_1}\right)\left(\frac{E_f}{E_c}\right)\left(\frac{V_f}{1-\nu}\right)(\alpha_f-\alpha_m)\Delta T\right] \tag{4.4}$$

$$\Phi_1 = 1-\frac{1}{2}\left(\frac{1-2\nu}{1-\nu}\right)\left(1-\frac{E_c}{E_f}\right) \tag{4.5}$$

$$\Phi_2 = \frac{1}{2}\left(1+\frac{E_c}{E_f}\right) \tag{4.6}$$

where the Poisson's ratio $\nu \approx 0.2$ [92], and α_m and α_f were the coefficients of thermal expansion of the matrix ($4.6 \cdot 10^{-6}\ ^\circ C^{-1}$ [86]) and fibers ($4.5 \cdot 10^{-6}\ ^\circ C^{-1}$ [94]). The temperature difference during cooling (ΔT) $\approx 1000^\circ C$ [5]. Elastic parameters Φ_1 and Φ_2 were obtained from [93].

In the model of Yang et al. [2], the interfacial debonding was characterized by considering a cylindrical fiber embedded in a region of matrix, with negligible interfacial volume fraction. In both HFC and LFC specimens, differences in interphase thickness

did not fundamentally change the progression of the matrix cracking and subsequent debonding, which predominantly occurred at the fiber-interphase surface even in regions with thicker coatings (detailed in Section 2.2.2). A rule of mixtures calculation was used to estimate the composite modulus, with $E_m = 415$ GPa and $E_f = 400$ GPa for SiC fibers and matrix, respectively [88, 5]. Values for the fiber and matrix volume fractions for LFC and HFC specimens are given in Table 2.1. The fiber radius $r \approx 6.5\mu m$ based on cross-section imaging from Figure 2.1, and interfacial parameters from Table 2.2 were used. In the experimental configuration used, the force was constant along the axial direction. To estimate the applied stress for each model (which is infeasible to quantify directly), two conditions were considered: (i) where the applied load was assumed to be exerted only over the cross-sectional area of fibers in the crack wake; and (ii) where the applied load was assumed to be exerted over the entire specimen cross-section.

In Figure 4.7, averaged COD trends from the models described in Eqs. 4.1 and 4.2 [1, 2] for both stress conditions were overlaid onto the experimentally-captured COD trends (which were also modified to consider each stress condition). When the stresses were considered to be the applied loads over the fiber tow area (condition 1), models for both minicomposite systems overestimated the crack opening behavior; this was more exaggerated for the LFC system. By the second stress condition, where the local stress was assumed to be equal to the globally-applied stress, both models better reflected the COD behavior in the smaller cracks seen in the LFC system. However, models slightly under-predicted the COD trends in the HFC system. It is worth nothing, however, that some cracks likely exhibited the predicted COD behavior in HFC specimens. Near the grip ends, matrix cracks formed which, while visually observable, initiated below the pixel resolution and did not apparently grow under continued loading; these hairline cracks, which rarely generated AE once formed, may have had similar crack opening trends to those predicted by models. Overall, the entirety of the active cracks tracked

(i.e. those that produced AE throughout the specimen lifetime) in the HFC specimen and the majority of the active cracks tracked in the LFC specimen existed in the envelope of the predicted COD behaviors between these stress conditions.

It is also important to couch these trends within the context that models for estimating CODs in unidirectional CMCs typically consider the stress distribution in the fiber and the matrix around an *isolated* crack (i.e no overlapping damaged lengths of neighboring cracks). Chateau et al. [4] predicted that matrix cracks with the largest openings behaved similarly to isolated cracks, for minicomposites similar to the LFC system. This may explain why the most representative COD model behavior was in the LFC system, in which the largest cracks were >2x the crack opening width of the average matrix crack and exhibited larger crack spacing to their nearest neighbors.

For the HFC system, neither stress-model scenario represented the COD behavior of active cracks, which was expected as both models considered weakly-bonded interphases of negligible volume fraction. Instead, when the interfacial parameters were high, the predicted critical debond toughness far exceeded that estimated for the compliant interphase 530 MPa in the HFC system compared to 150 MPa in the LFC system by Eq. 4.3). Moreover, thick BN interphases may have contributed a larger compressive thermal residual stress than was predicted here [107]; this was not accounted for in the assumption of thin interphases leading to small thermal residual stresses based on the near-identical CTEs of the fiber and matrix. Rather, these modeling trends suggested that *neither* the assumption of load applied over the entire CMC cross-section (which was expected given that crack opening occurred only *after* some portion of the cross-section cracked) nor the assumption of only fully load-bearing fibers in the crack wake represented the real stress-condition in the crack plane. Contradiction of the second scenario was more significant, given that models for unidirectional CMCs typically considered that once a matrix crack formed, it propagated through the entirety of the cross-section. However,

both in-SEM observations in this dissertation (Figure 2.12) and previous investigations [25], have shown matrix cracking in unidirectional CMCs to be incremental. Specifically, these COD trends demonstrated that, even if the initial local stress under which a partially-propagated matrix crack opened lay between the earliest stress states estimated by these stress scenarios, whether the crack eventually propagated to through-thickness or not, its opening could never reach the COD predicted by the scenario of only intact fibers bearing load.

In the LFC system, the first stress condition was the poorest representation of the COD behavior. From the modeling inputs, this was primarily driven by an interfacial shear stress nearly half that of HFC specimens. These modeling results suggested that stresses in the crack plane were more similar to that estimated by the globally-applied stress. In the HFC system, the modeling trends flanked the experimental COD behavior, in a manner similar to upper and lower bounds, using the two stress scenarios. The slight overestimation by the first stress condition indicated that small regions of intact matrix in the plane of the crack carried some portion of the stress during loading (i.e fibers were not entirely responsible for bearing load after cracks initiated). The intermediate COD behavior may therefore be the result of the incremental matrix crack progression described in Chapter 2.

In [1], Marshall et al. distinguished between the crack openings resulting from the formation of large and small cracks. They ascribed that large cracks exhibited crack openings u that grew but could not exceed the equilibrium separation u_0 of the through-thickness failed matrix. This upper bound on the crack opening was approached when the crack length c exceeded a characteristic distance c_0 from the crack tip. Within this region, the bridging force of intact fibers offset the applied force. The crack tip stress concentration was exclusively induced over c_0, and the stress needed to propagate the crack was independent of the crack length c (i.e. steady-state crack growth). For short

cracks, where $c < c_0$, the entire length of the short crack added to the stress concentration, such that the stresses needed to propagate the crack were dependent on c.

Quantifying these characteristic crack tip distances and their effect on crack openings was motivated both by experimentally-observed variations in matrix cracking between LFC and HFC specimens (which are described in detail in Chapter 2). In LFC specimens, matrix cracks could propagate across the specimen cross-section in a single step due to the high degree of in-plane matrix content. It was therefore likely that these matrix cracks would satisfy the conditions of long cracks. Whereas, in HFC specimens, where matrix cracking was more stepped (Figure 2.12), and smaller cracks formed due to limited in-plane matrix, the possibility existed that some cracks exhibited crack opening behavior more typical of short cracks. The length of c_0 was calculated by [1] as:

$$c_o = \frac{\sigma_\infty^4}{\alpha^2 (K^L)^2} \tag{4.7}$$

where σ_∞^4 was the remote stress, K^L was the crack tip stress intensity factor, and α was related to the constituent properties, given by:

$$\alpha = 8(1-\nu^2)\tau V_f^2 E_f \frac{1+\eta}{E_c r\sqrt{\pi}} \tag{4.8}$$

where $\eta = \frac{E_f V_f}{E_m(1-V_f)}$. The K^L of a straight crack perpendicular to the loading direction in an infinite plane, having a uniform remote stress ($\sigma = \sigma_\infty$) is $= \sigma_\infty\sqrt{\pi a}$, for a crack of length a. When a $= c_0$ Eq. 4.7 simplified to:

$$c_0 = \frac{\sigma_\infty}{\alpha\sqrt{\pi}} \tag{4.9}$$

In Figure 4.8 the characteristic crack distance c_0 is plotted as a function of the globally-applied stress for an LFC and HFC specimen. The largest calculated characteris-

tic crack length was $\approx 620\mu m$ and $\approx 140\mu m$ for the LFC and HFC systems, respectively. The estimated values of c_0 were compared to the matrix crack behavior using the (i) cylindrical, fully densified geometry assumed in Chapter 3, and (ii) measurements of the micrograph cross-sections shown in Figure 2.1. From (i), the maximum crack length (i.e. the diameter of the cylinder) was approximately $\approx 540\mu m$ and $\approx 450\mu m$ in the LFC and HFC system, respectively. From the specimen cross-sections, the maximum crack length ranged from $580 - 950\mu m$ in the LFC system. In the HFC system, this matrix crack length was significantly smaller. Isolated areas of the cross-section (previously described as pillars in Chapter 2), led to a range of crack lengths as small as $65 - 130\mu m$ (which were smaller than c_0) and as large as $\approx 700\mu m$.

In a materials system with a thin, weakly-bonded interface of negligible volume fraction (e.g. LFC), the large crack assumption was best-suited for predicting crack opening behavior and the short crack assumption was shown to be insufficient, in that the estimated matrix crack lengths c exceeded the characteristic crack length c_0. This was not the case in the HFC system, where limited in-plane matrix content drove the stepped crack propagation behavior. In this architecture, matrix cracks that formed within pillars (likely accounting for the majority of cracking activity) had crack lengths $c< c_0$. As such, for a given through-thickness matrix crack, it was possible that a crack which initially exhibited short crack behavior (i.e. the length of the crack drove the stress concentration at the crack tip) transitioned into long crack behavior through crack propagation. This may explain why neither the remote stress (for long cracks), nor the local stress in the short crack wake, was representative of the averaged COD trends across a single crack in the HFC system.

For short cracks, such as those predicted in the HFC system, Marshall et al. [1]

modeled the variation in crack opening as a function of distance from the crack tip as:

$$\delta(x) = \frac{2(1-\nu^2)K^L c^{1/2}(1-\frac{x^2}{c^2})^{1/2}}{E_c \pi^{1/2}} \tag{4.10}$$

where x was the position along the crack and c was the length of the short crack. For ease, $\sigma\sqrt{\pi c}$ was substituted here for K^L, by which Eq. 4.10 simplified to:

$$\delta(x) = \frac{2(1-\nu^2)\sigma\sqrt{c^2-x^2}}{E_c} \tag{4.11}$$

Using the short crack assumption resulted in overlap between the modeled COD predictions and the smallest experimentally-measured CODs in the HFC system. This trend indicates that the short crack model was only applicable to the earliest stages of matrix cracking in the low matrix content architecture, where cracking was incremental across pillars and bridged at each stage by the remaining intact portions of the cross-section.

In Figure 4.9, the distribution of CODs for short cracks (c $< c_0$) of varying lengths (c = 65 μm, 90 μm, 115 μm, and 130 μm) are shown as a function of the fiber stress. These crack lengths were the measured lengths of pillars in the HFC cross-section in Figure 2.1. The stresses were estimated using the area of the fiber tow, assuming an approximately equivalent distribution of stress across the cross-section. To compute the transmission crack length for each of these pillar lengths, Eq. 4.7 was modified such that $K_L = \sigma\sqrt{\pi c}$, by which:

$$c_0 = \frac{\sigma_\infty^2}{\alpha^2 \pi c} \tag{4.12}$$

In this calculation of the maximum characteristic crack length, σ_∞ was assumed to be equivalent to σ_{sat}, the matrix crack saturation stress for the HFC specimen (approximately 850 MPa). As a result, for cracks of lengths c = 65 μm, 90 μm, 115 μm and

130 μm, the characteristic crack length was c_0 = 140 μm, 100 μm, 80 μm, and 70 μm, respectively.

Only limited portions of the envelope of CODs predicted using the short crack model reflected the experimentally-observed crack opening behavior (Figure 4.9), demonstrating that the short crack model was not readily applicable for predicting CODs in unidirectional CMCs. Furthermore, as the fiber stress was used here in lieu of the remote stress, use of the remote stress would result in even larger underestimates of crack opening distributions for all values of c.

One possibility for this underestimation at both long and short cracks by models in [1] and at long cracks by [2], was that these models often considered the scenario of fully intact fibers in the crack wake. However, a portion of the fiber tow was broken at each matrix crack plane prior to rupture [4]. This was predicted by micromechanical models [3] and has been demonstrated in recent experimental work [60] for the LFC system. For the HFC system, given that only partial debonding of the interface was predicted (Chapter 3) in conjunction with increased global AE activity (Chapter 2), early fiber failures were also expected.

The effect of these early fiber failures was increased fiber tractions $T(x)$, so that the closure pressure in the plane of the crack continued to balance the remote applied stress ($p(x) = \sigma_\infty$). This was described in Marshall et al. [1], where the closure pressure of fibers to bridge cracks as a function of the position along the crack surface was given as $p(x) = T(x)V_f$.

An envelope of COD trends across the stress profile, shown in Figure 4.11, was created as follows. By taking into account the progressive decrease in the fiber volume fraction due to gradual fiber failure (and the relative increase in the non-fiber volume fraction), estimates of the crack opening exceeded the cases shown in Figure 4.7 using Eqs. 4.1 and 4.2. In Chapter 3, the portion of the fiber tow broken in the vicinity of a matrix crack

prior to rupture was estimated by [3] in the range of q = 22%-31%. The relative fiber volume fraction after some quantity of fiber breaks occurred could then estimated by:

$$V_f = \frac{(1-q)\cdot n_{FT}\cdot \pi r^2}{A_c - (qn_{FT}\cdot \pi r^2)} \tag{4.13}$$

where the numerator represented the cross-sectional area of intact fibers after some portion of the tow q was broken, and the denominator represented the initial specimen cross-sectional area A_c minus the area of the broken fibers. For crack openings at the last loading increments, a range of openings were predicted by considering $q = 0.22-0.31$. At the earliest loading increment, $q = 0$, as it was assumed that no fibers were broken at this point. Recent work by Hilmas et al. [62], showed that the fiber break accumulation followed an approximately linear trend. In accordance with their findings, the approximated portion of the fibers broken at each crack as a function of the globally-applied stress was determined using a linear interpolation between two sets of points: (i) $q = 0$ at the first load state and $q = 0.22$ at the final load state; and (ii) q 0 at the first load state and $q = 0.31$ at the final load state.

For the LFC system, accounting for the progressive fiber failure considerably improved modeling predictions, such that models were able to resolve some of the larger crack openings that were underestimated when considering $q = 0$. For the HFC system, this consideration allowed for overlap between modeling estimates of COD with experimental measurements, but only at the later loading stages. Thus, it can be assumed that this predicted range of q was better suited for the LFC system, whose architecture was more representative of the modeling constraints of [3].

Instead, it was likely that a greater portion of the tow was broken in the crack wake in the HFC system than the predicted range of q = 0.22 - 0.31, which was for an ideal unidirectional CMC. Given higher interfacial parameters that obstructed debonding and

sliding, the stress in the crack wake was likely higher in the HFC system. Furthermore, modeling predictions described in Chapter 3 estimated a higher number of total fiber failures in the HFC system.

It was found that both models required unrealistically large inputs of q to output the largest experimentally-measured CODs, as they predicted steady crack opening with convergence to approximately 0 μm as the matrix cracking stress was approached. For the LFC system, $q = 0.48$ for the Marshall model and $q = 0.29$ for the Yang model, only the latter of which fell between the range predicted by [3]. For the HFC system, q exceeded half of the fiber tow, with $q = 0.70$ for the Marshall model and $q = 0.55$ for the Yang model. Such large values of q were physically unlikely, given that the composite continued to bear load beyond where these final COD measurements were taken.

Rather, the experimental findings of Figure 4.11 instead showed that the initial matrix crack opening rate (dδ/dN) was substantially higher than the continued crack opening rate. One explanation for this was given in Chateau et al [4], based on the model of interface debonding with constant friction developed by Hutchinson and Jensen [16]. They hypothesized that the initial crack opening rate was predicated by the stress needed to overcome *both* the frictional resistance and the critical debond stress, whereas the continued crack opening rate was predicated only on overcoming frictional resistance, consistent with [108]. They gave this relationship between crack opening and the applied load F as:

$$\delta = \lambda_2 F^2 + \lambda_0 \tag{4.14}$$

where λ_0 was related to the critical debond stress σ_d and the interfacial shear stress τ:

$$\lambda_0 = \frac{\sigma_d^2 r(b_2 + b_3)}{2\tau E_m} \tag{4.15}$$

and λ_2 was related to only the interfacial shear stress τ. This term was modified here as:

$$\lambda_2 = \frac{(b_2 + b_3)r}{2\tau E_m} \left(\frac{1 - \frac{E_f}{E_c} V_f}{500\pi r^2 - q \cdot 500\pi r^2} \right) \tag{4.16}$$

where the term $500\pi r^2 - q \cdot 500\pi r^2$ refers to the fiber tow area (originally presented as A_f in [4]). When $q = 0$, this term simplified to the full tow size, and accounted for the progressive reduction in the fiber area as q increased.

In Eqs. 4.15 and 4.16, constants b_2 and b_3 were non-dimensional constants given in Hutchinson and Jensen [16] as combinations of the elastic parameters (using type II boundary conditions having zero shear traction with constrained normal displacement); the composite modulus was approximated using a rule of mixtures estimate. In [16], b_2 was given as:

$$b_2 = \frac{(1+\nu)E_m \cdot [2(1-\nu)^2 E_f + (1-2\nu)[1-\nu+V_f(1+\nu)](E_m - E_f)]}{(1-\nu)(1-V_f) \cdot [(1+\nu)E_c + (1-\nu)E_m]} \tag{4.17}$$

and b_3 was given as:

$$b_3 = \frac{V_f(1+\nu) \cdot [(1-V_f)(1+\nu)(1-2\nu)(E_f - E_m) + 2(1-\nu)^2 E_m]}{(1-\nu)(1-V_f) \cdot [(1+\nu)E_c + (1-\nu)E_m]} \tag{4.18}$$

For this model, the evolution of the fiber failure given by similar linear interpolations used in Figure 4.11 affected the estimate of the fiber volume fraction (V_f) at each load state; in turn, this change consequently influenced values for parameters b_2 and b_3. In Figure 4.12, the crack openings predicted by Eq. 4.14 as a function of the globally-applied stress are shown for the HFC and LFC system. Again, the COD evolution considered $q = 0$, the linear interpolation up to $q = 0.22$, and the linear interpolation up to the maximum value of q needed to capture the largest experimentally-measured CODs.

A significant improvement in modeling prediction accuracy was observed in Figure

4.12. In the LFC system, the portion of the tow broken to output the largest CODs was $q = 0.32$, just slightly beyond the range predicted by [3]. In the HFC system, this same measure was $q = 0.38$, a more reasonable estimate of the portion of the tow broken than the values obtained in Figure 4.11. An interesting observation from Figure 4.12 was that while the COD predictions using $q = 0$ was suitable for some active cracks in the LFC system, this trend remained an underestimate of COD behavior even in the improved model. One possibility was that this behavior was driven by continued underestimation of the initial crack opening rate, based on the λ_0 and λ_2 terms; this may have come from the chosen input parameters (i.e. use of an averaged interfacial shear stress τ from push-in testing, which exceeded a more accurate value). Another possibility exists that this underestimate, which was more significant at the earliest load states, suggested that fiber failure may have occurred earlier than previously thought. In that scenario, premature fiber breaks would have occurred in conjunction with the early matrix crack formation in the pillars, and may have contributed to the higher degree of initial crack opening, such that $q \neq 0$ at the earliest load states. Further work is needed to confirm this hypothesis.

4.4 Summary

In this chapter, *in situ* matrix crack opening displacements (CODs) were characterized for two systems of SiC/SiC minicomposites. Variations in COD trends were related to microstructural differences within specimens and across systems. In the system with thin, compliant interphases (LFC), a higher initial crack opening rate was found due to the lower fiber volume fraction and reduced ability to apply bridging tractions to larger evolving cracks. After the onset of major matrix cracking, a broader distribution CODs was found, likely due to increased debonding and sliding in the crack wake due to globally lower interfacial properties. The improved ability to activate these non-dominant mech-

anisms also mitigated premature fiber failure, allowing for larger cracks to accommodate locally high stresses. Conversely, in the system with strongly-bonded interphases and low matrix content (HFC), the decreased likelihood of crack deflection inhibited debonding, preventing cracks from opening to the degree seen in the LFC system. In this system, higher fiber content initially bridged smaller matrix cracks (resulting from incremental cracking of the cross-section), leading lower initial crack opening rates. Then, when fibers broke, there was an uneven redistribution of stress to intact fibers in the plane of the crack due local load sharing, which enabled continued crack bridging. These broken fibers could be reloaded through fiber bridging near the initial break, due to smaller sliding lengths resulting from higher interfacial parameters. At the failure location, the effect of these combined phenomena was a COD trend that was indistinct from the behavior of other evolving matrix cracks, unlike the failure crack trend observed in LFC specimens. While an uneven distribution of damage events (presumably, fiber breaks) was observed beyond the matrix crack saturation stress from AE, the COD trends observed herein did not appear to depend on where fibers began and continued to fail.

These experimental results were compared to modeling trends, first from two models from [1, 2]. It was found from these models, that the more COD predictions mandated use of the remote stress rather than the fiber stress; however, preliminary COD predictions often underestimated the experimentally-observed behavior for two reasons: (i) in these models, the progressive fiber failure after the onset of matrix cracking was not considered, and (ii) the variation in the initial crack opening rate (upon crack formation) and the subsequent crack opening rate (upon continued axial loading) was neglected, as these models converged to COD predictions near 0 μm as the matrix cracking stress was approached. These findings motivated the exploration of a third model from [4] based on [108], which was modified herein to include the progressive fiber failure. The COD predictions of this model were demonstrated to be in good accordance with the experimentally-characterized

CODs in the LFC system. Although this model also demonstrated significant improvement in COD predictions in the HFC system, further work is needed to understand the still underestimated initial crack opening rate.

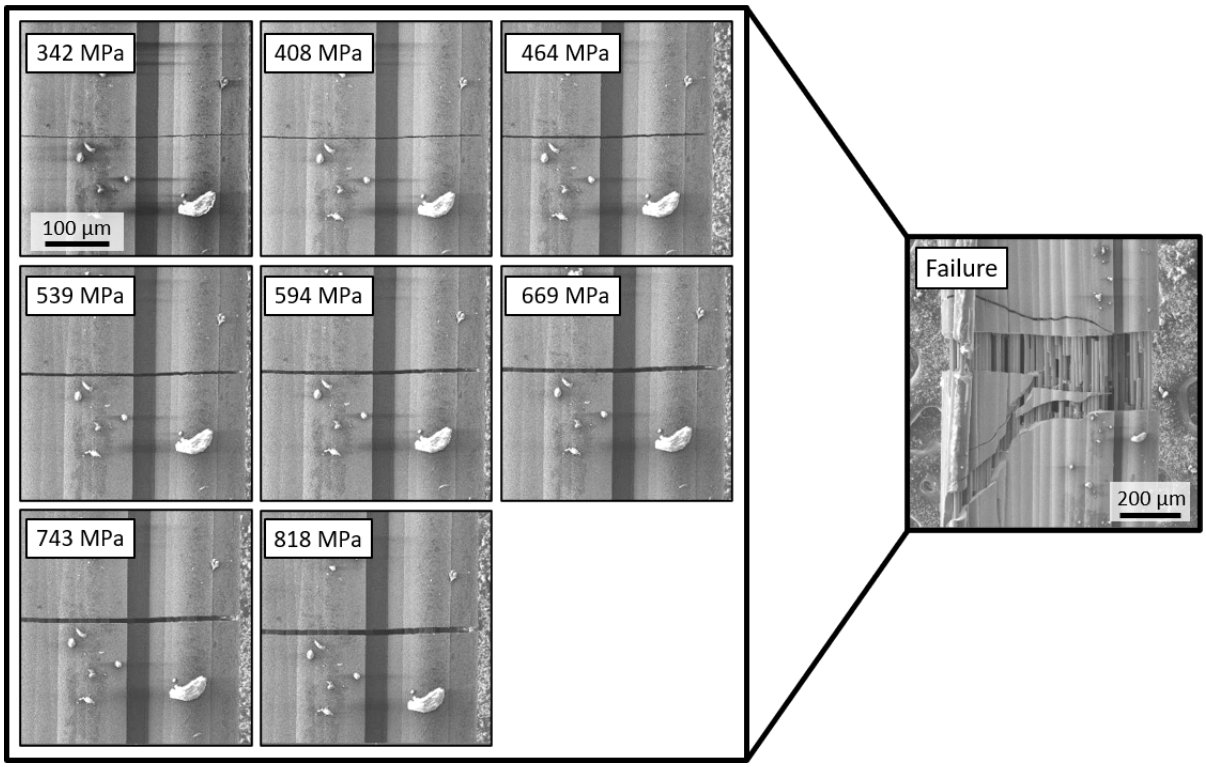

Figure 4.1: The progressive crack opening behavior at the crack that eventually becomes the failure location is shown. By high-resolution SEM, the *in situ* behavior of these CODs can be measured, which has the potential to advance understanding of why some cracks evolve to become more probabilistic locations for failure than other cracks.

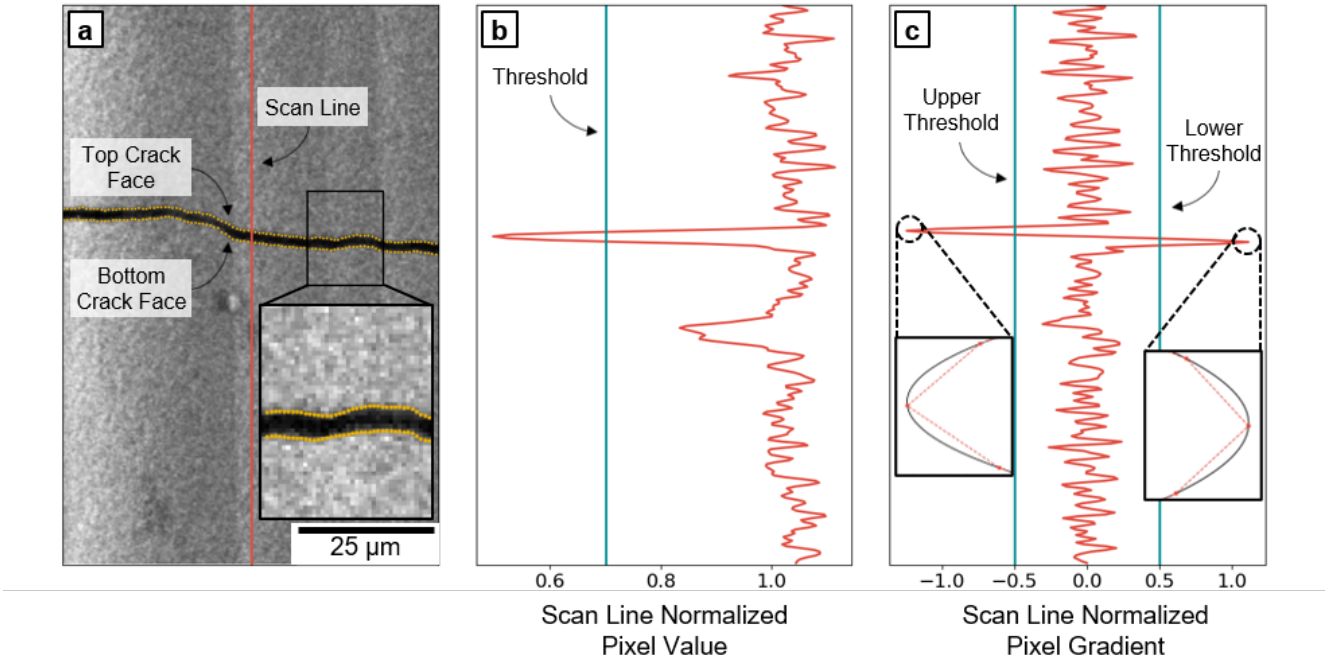

Figure 4.2: An algorithm for measuring crack opening displacement: **a**) a Gaussian blur was applied to a micrograph. In **b**) the median normalized pixel value was plotted along the single scan line identified in (a). In **c**) the median normalized pixel gradient was plotted along the same scan line. As the normalized pixel value for this scan line at the crack location exceeded the set threshold (shown by the line in (b)), the algorithm determined that there was a crack along the scan line. The algorithm measured the top and bottom of that crack along the scan line where the normalized image gradient at the crack location exceeded the set upper and lower thresholds (shown by the two lines in (c)).

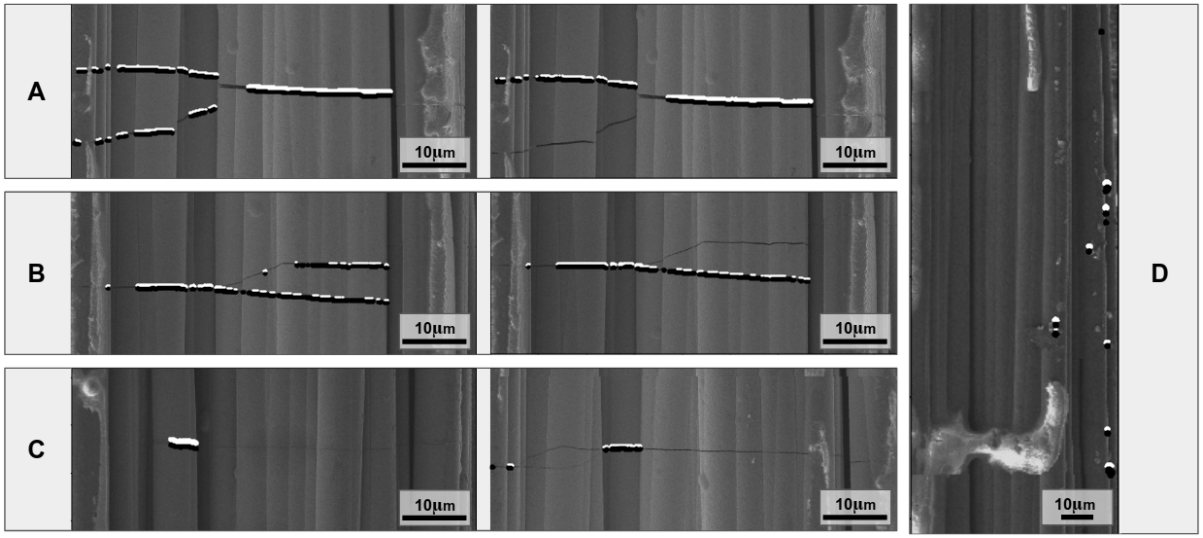

Figure 4.3: Example images of crack verification system. **a**) One example of a split crack. In this case, the lower fork was not measured due to being a branch of the main crack. In **b**, there is another example of a split crack where in this case the top fork was neglected due to being a branch of the main crack. In **c** there are two examples of cracks that could not be accurately resolved due to being too thin to be accurately detected. In these cases, a threshold must be selected or more measurements taken manually to accurately measure the crack. Finally, **d** demonstrates a common failure mode of the algorithm in treating artifacts as cracks and trying to measure them thus necessitating the use of some sort of crack verification algorithm.

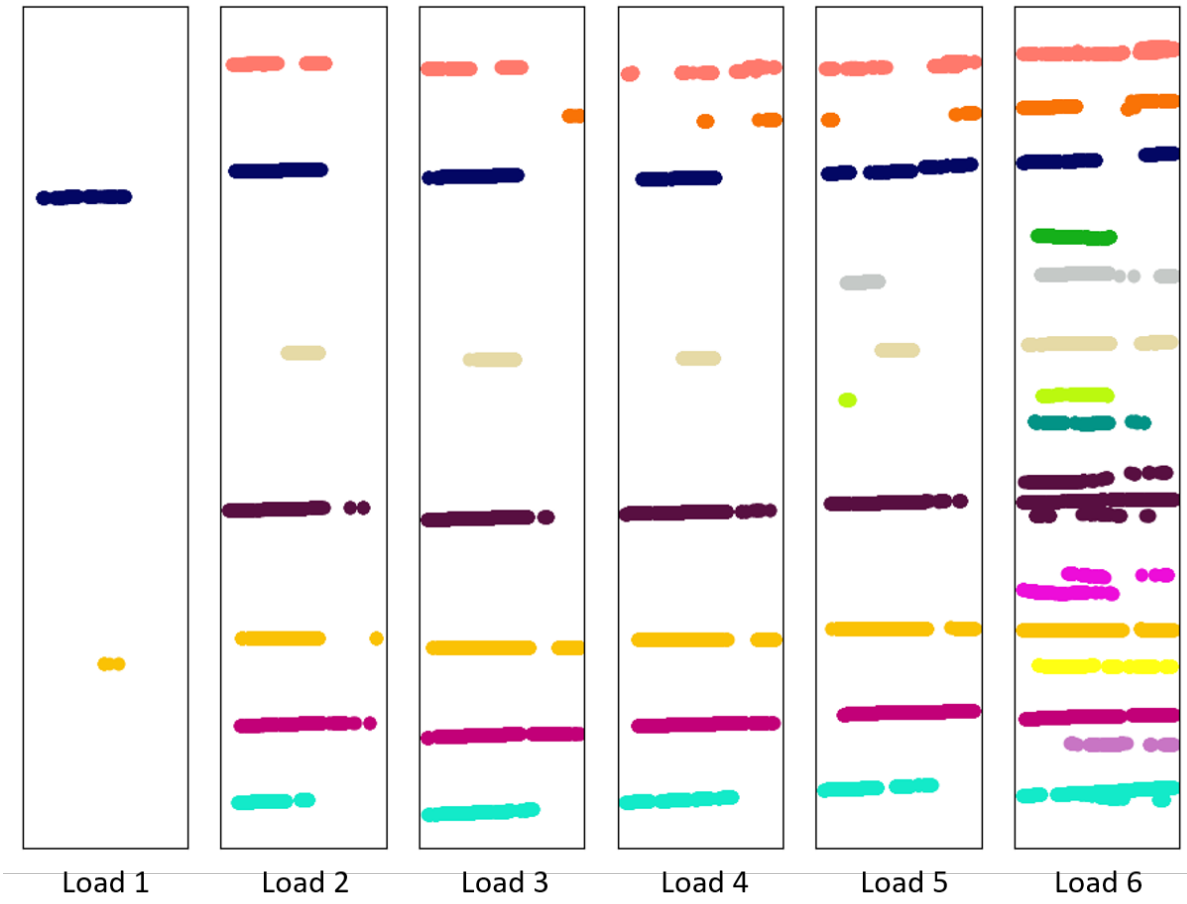

Figure 4.4: An algorithm was used to distinguish and identify cracks in micrograph panoramas across load states, allowing for COD measurement as a function of globally applied stress. Using k-means clustering, CODs were labeled to their affiliate crack (shown by colors), converting a point cloud of crack opening measurements into a series of CODs measured along the length of a given crack at single load state. To group CODs for a given across load states, a manual method was used to group CODs by crack centroid information, identified as the same color across micrographs.

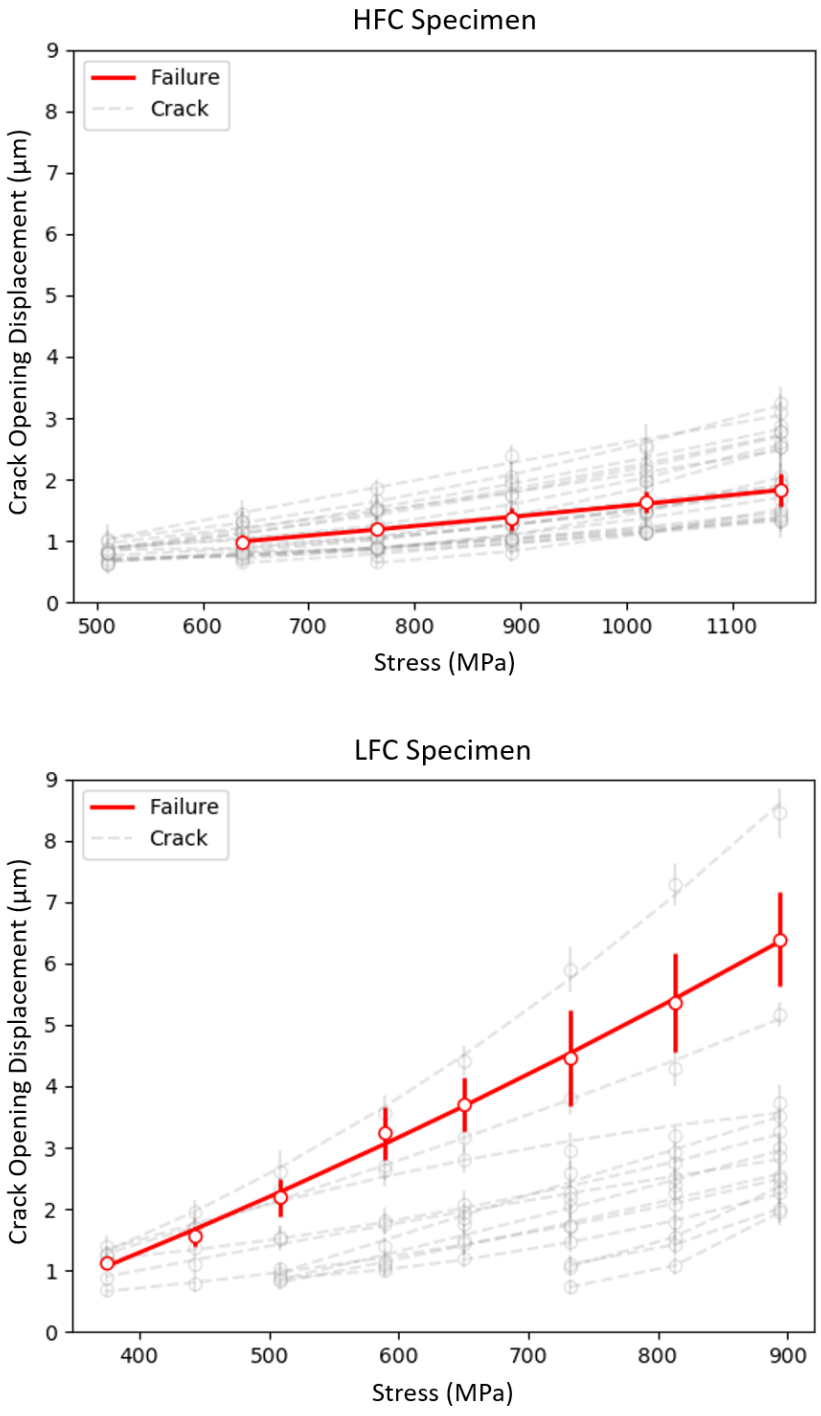

Figure 4.5: A narrower COD distribution was observed in the (a) HFC system versus (b) LFC system, driven by microstructural effects. including variations in matrix content (which promoted differences in matrix cracking behavior) and interfacial properties (which affected crack deflection capabilities and subsequent debond lengths).

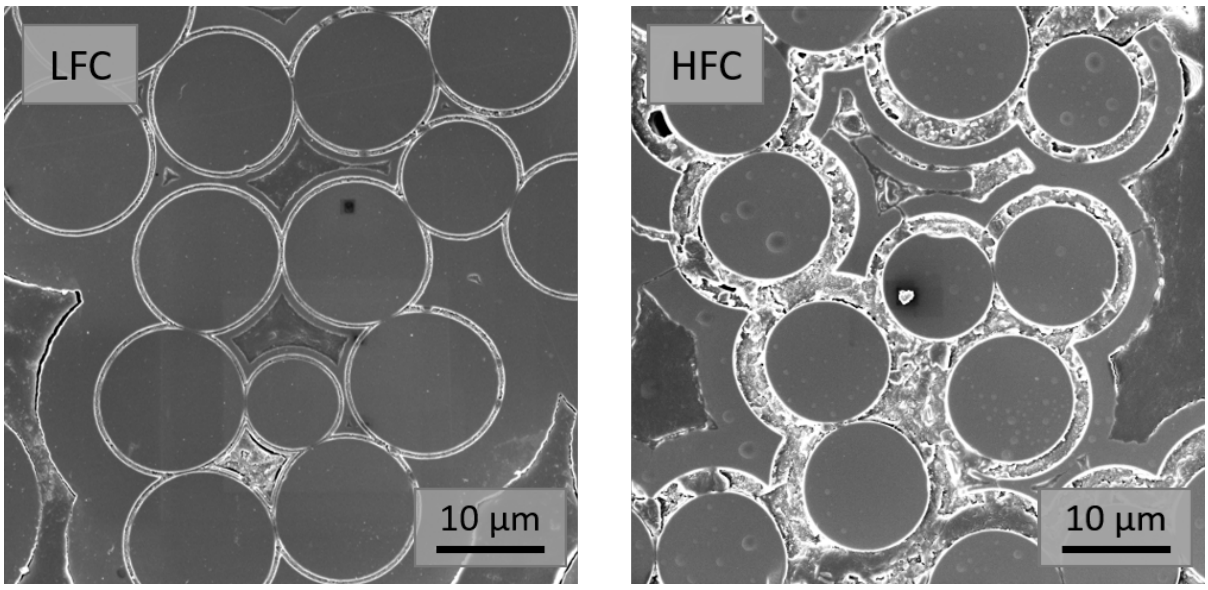

Figure 4.6: Fiber distribution in LFC and HFC specimens is heterogeneous, in contrast to fundamental modeling assumptions. In these systems, closely spaced regions of fibers result in uneven interphase deposition.

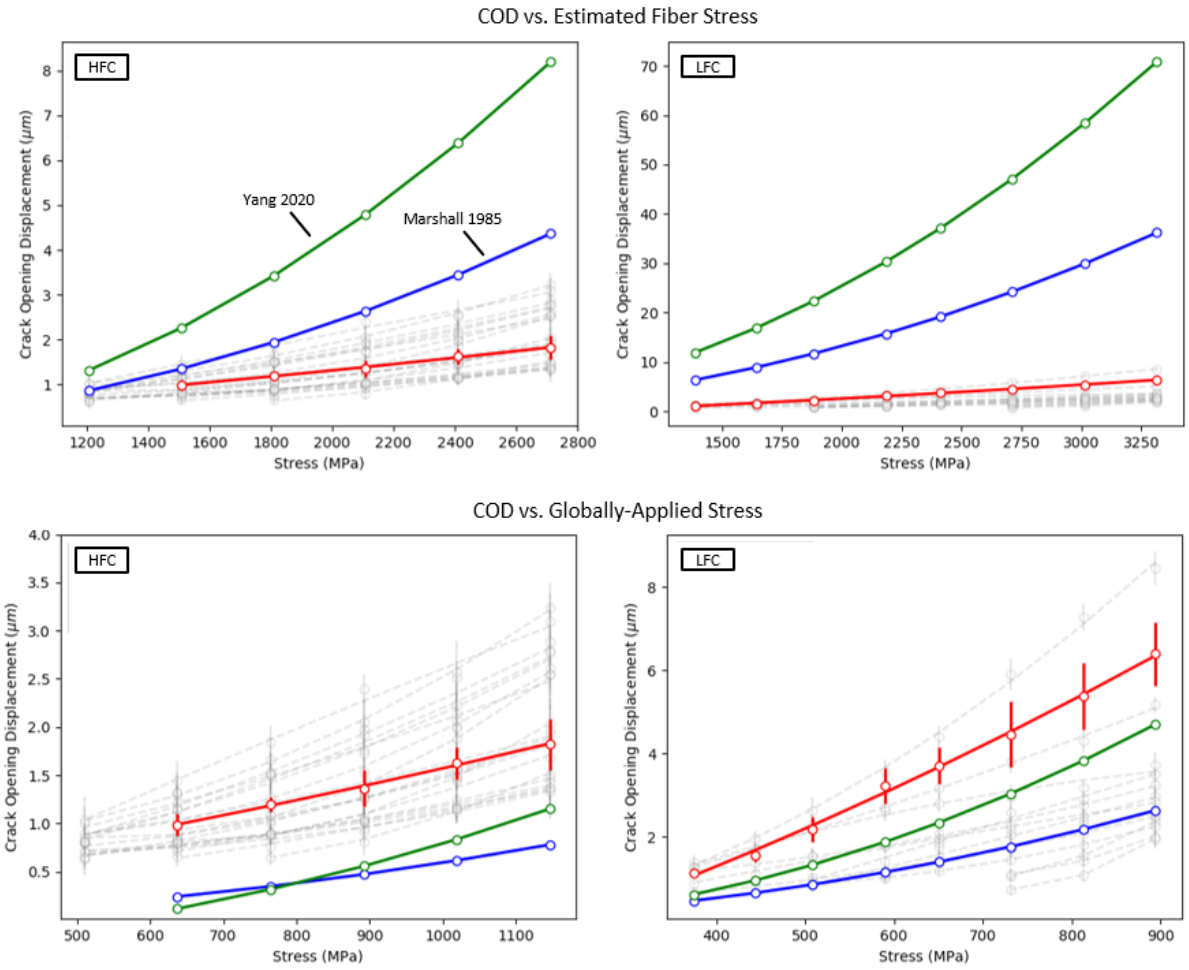

Figure 4.7: Modeling predictions of COD based on [1, 2] demonstrated that the local stresses in the plane of the crack are more consistent with the remote stress. Furthermore, these trends indicated that even if the stresses in the plane of a crack exceeded the globally-applied stress at the same load state when that crack propagated to through-thickness, its opening could never reach the COD predicted by the scenario of only intact fibers bearing load.

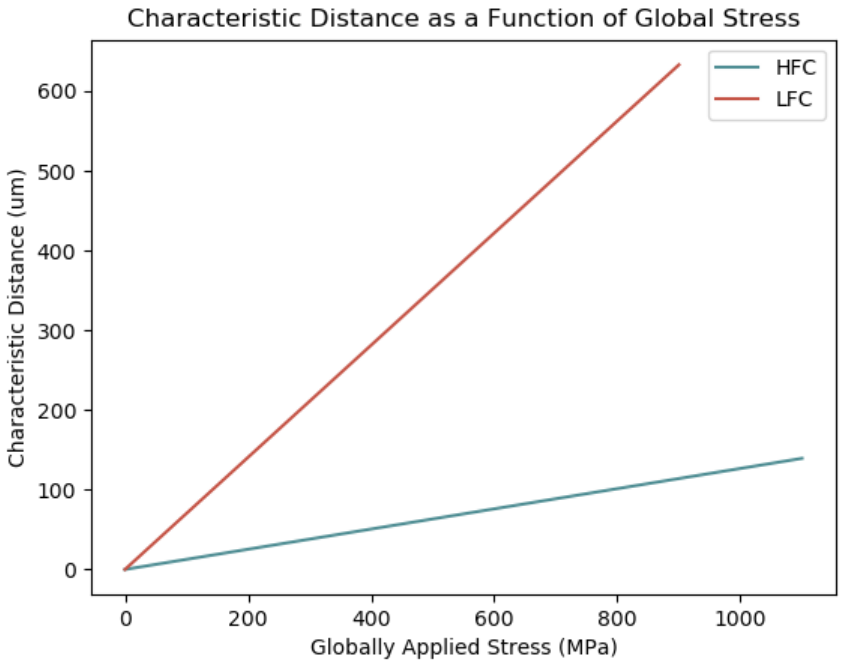

Figure 4.8: Quantifying the characteristic crack tip length c_0 verified that the long crack assumption was appropriate for the LFC system, whose architecture better reflected modeling assumptions. For HFC specimens, where a single through-thickness crack formed over several stages, these predictions suggest that early crack stages behave like short cracks and then transition into exhibiting long crack behavior.

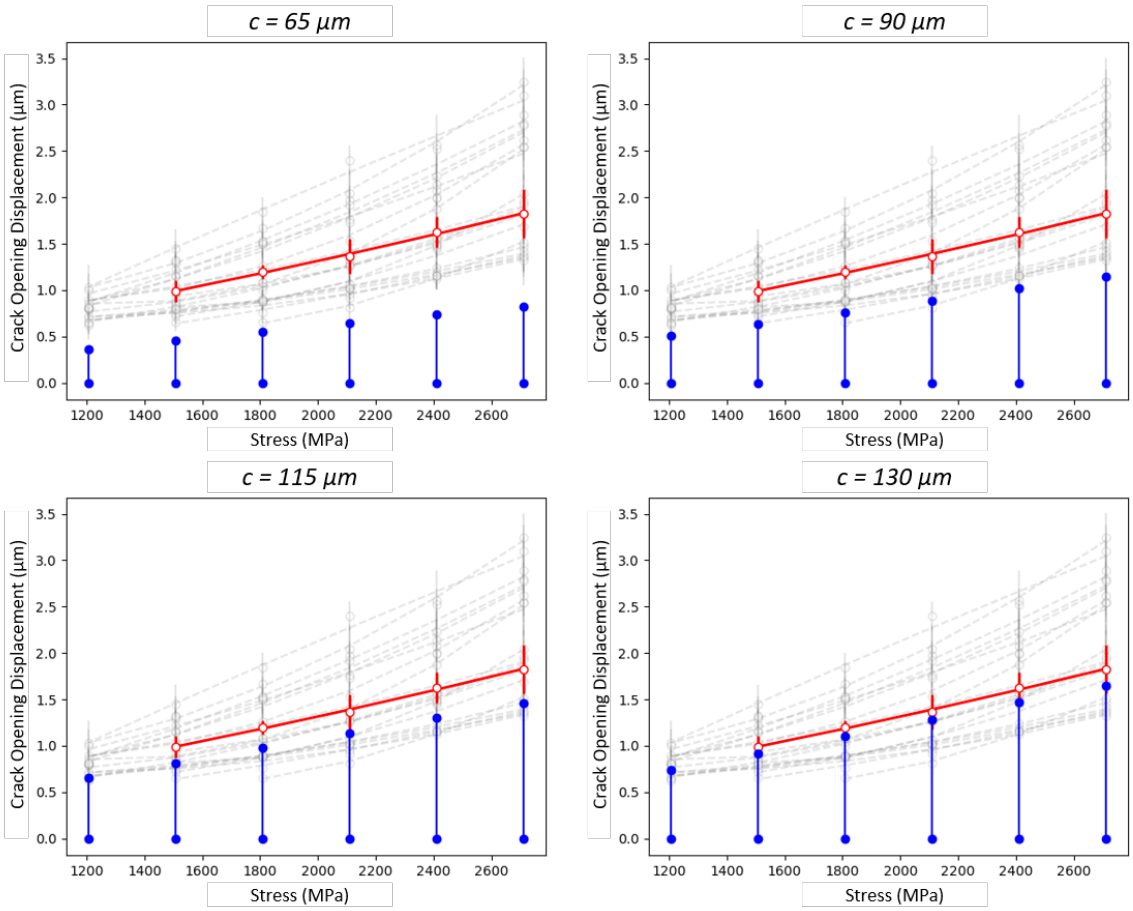

Figure 4.9: Limited portions of the envelop of CODs predicted using the short crack model reflected the experimentally-observed COD behavior, demonstrating that the short crack crack model was not readily applicable for predicting averaged CODs in unidirectional CODs.

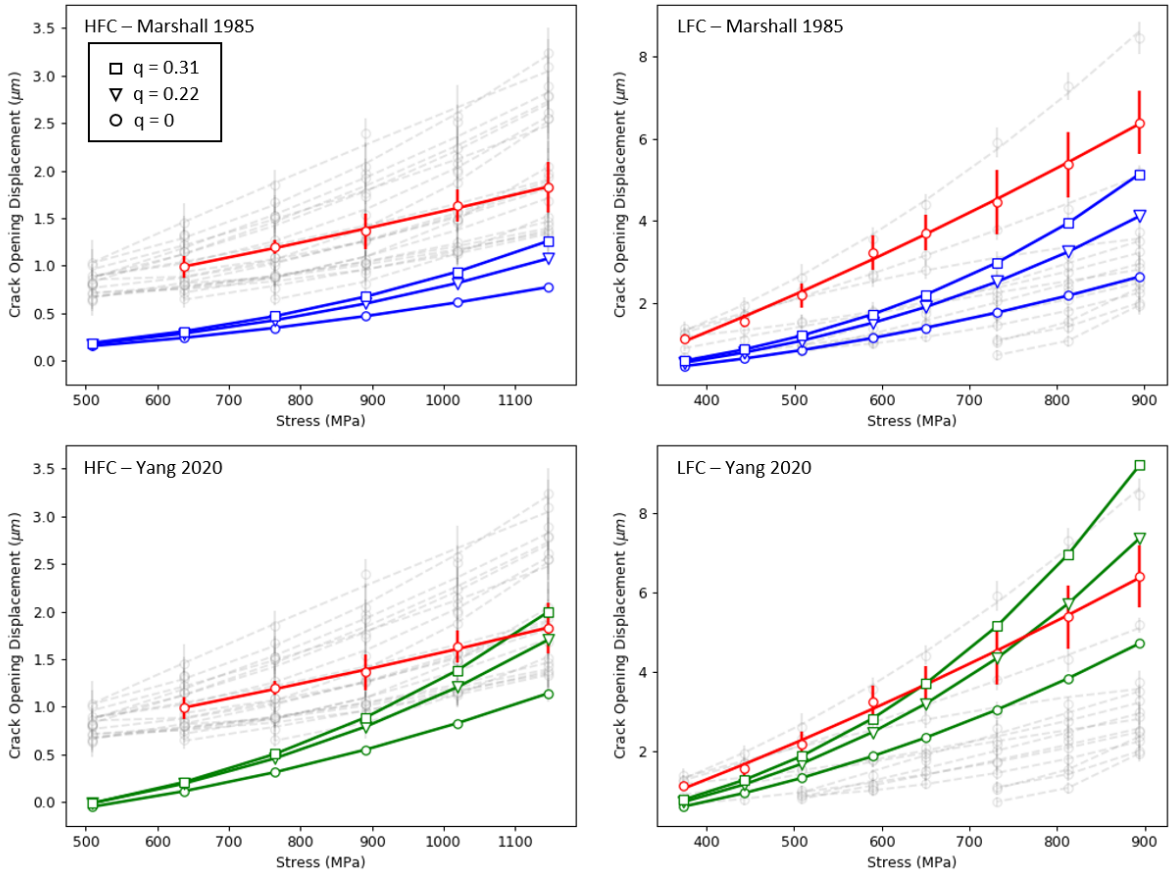

Figure 4.10: By accounting for the progressive fiber failure up to the range of $q = 0.22$ - 0.31 predicted by [3], a range of modeled CODs in agreement experimentally-obtained measurements was found in the LFC system. This demonstrated the general suitability for models in the literature to characterize CODs in the more representative CMC material system. In the HFC system, even in accounting for this range, modeled COD data only represented the experimentally-obtained behavior at the largest load states. One possibility for this behavior was that a greater portion of the tow failed prior to specimen rupture than was predicted by [3].

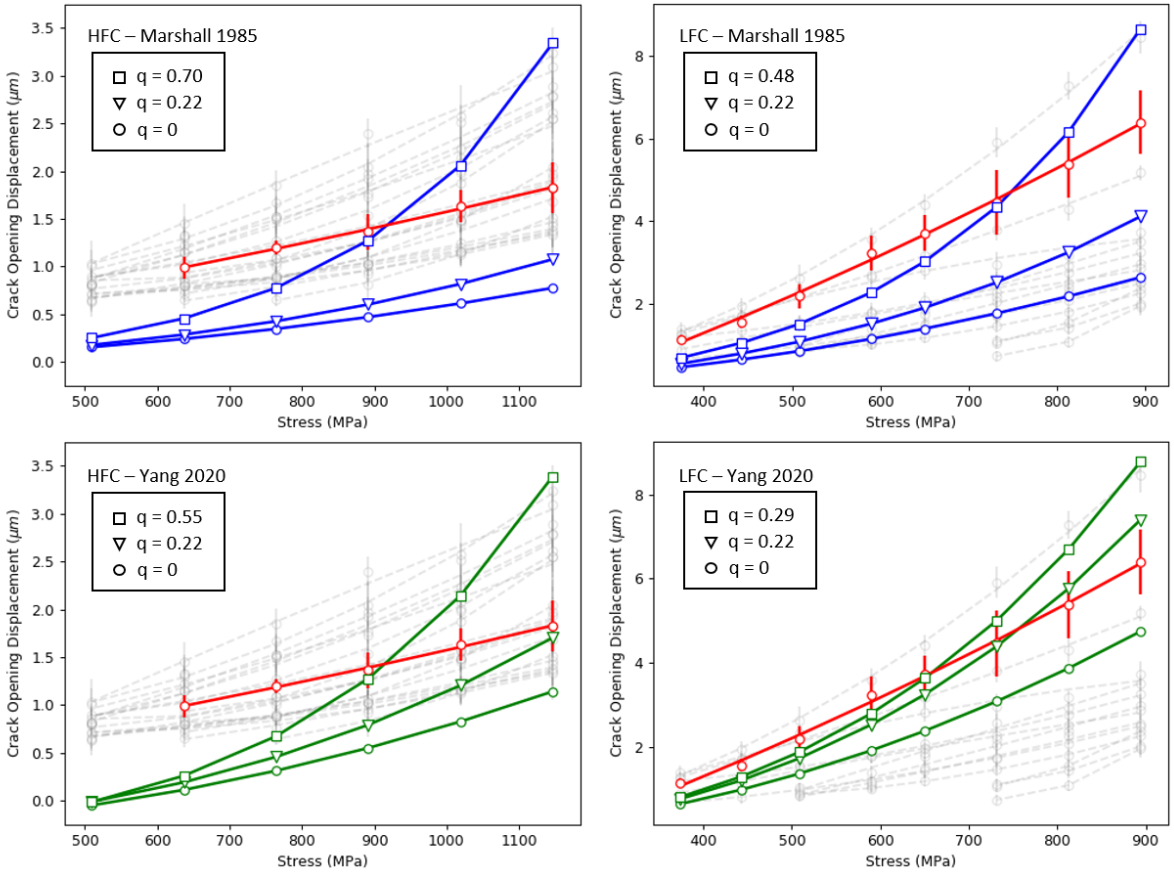

Figure 4.11: The largest values of q needed to output the largest measured CODs were physically unrealistic and far exceeded the ranges of q predicted via [3]. It was apparent that while the curve fits of models were fair representations of the real crack opening behavior, the most significant discrepancy was at the earliest load state, wherein the initial matrix crack opening far exceeded the crack opening predicted by [1, 2].

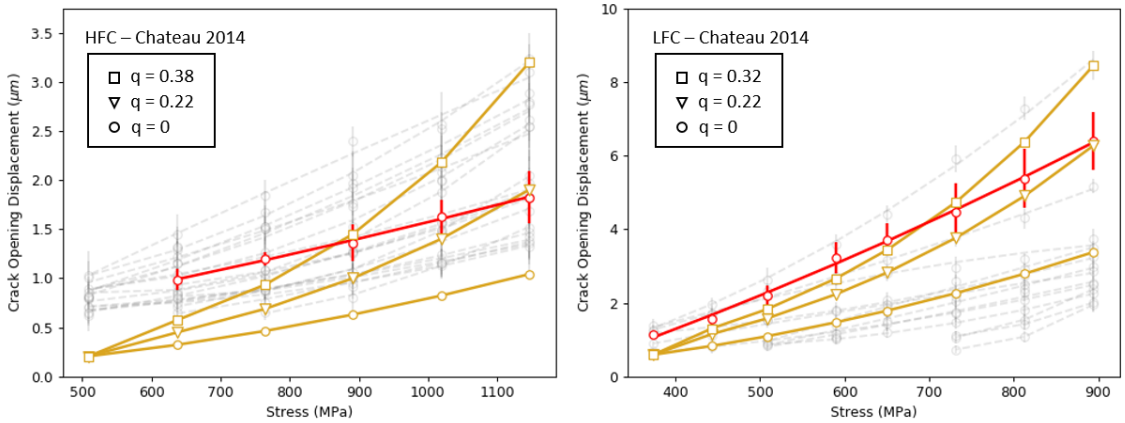

Figure 4.12: Inclusion of both the progressive decrease in volume fraction and the consideration of variation between the initial crack opening rate (at matrix crack initiation) and subsequent crack opening rate (upon continued crack opening) facilitated more accurate modeling predictions based on [4]. By these considerations, the portions of fibers broken in the crack wake (q) to produce the maximum measured CODs were much closer to the range predicted by [3].

Chapter 5

Conclusions and Recommendations

5.1 General Conclusions and Impact

SiC/SiC CMCs are high performance materials that are currently employed in high temperature and extreme environment applications. Though these composites have been investigated for decades, it is a relatively recent development that powerful approaches can resolve *in situ* damage at the length scale on which it occurs. Characterization of damage phenomena is critical to improving modeling efforts that aim to relate stress, time, damage, and environment. Towards that goal, this dissertation undertook an experimental investigation into damage accumulation in two systems of SiC/SiC minicomposites at room temperature.

First, a multi-modal approach which correlated bulk AE information with high-resolution surface-observed damage via in-SEM mechanical testing was created (Chapter 2), that demonstrates the accuracy and potential of AE for assessing the local evolution of damage. Using this approach, early surface microcracking was correlated with its resultant AE, and all observed surface damage in the area of interest was mapped onto its corresponding AE activity. It was found that LFC specimens generated fewer AE

events than similarly-sized HFC specimens, primarily as a result of fewer transverse matrix cracks, each of which propagated to through-thickness in fewer steps. The AE-SEM approach enabled comparison of the AE-estimated transverse matrix crack density evolution (CDE) and the experimentally-observed CDE; it was found that the AE-estimated CDE was more accurate in HFC specimens where non-cracking mechanisms were likely less active than in LFC specimens. In both systems, the highest density of AE events was generated near the failure location throughout loading by one or more evolving cracks, demonstrating that clustered local damage activity strongly correlated with failure. After the onset of observable matrix cracking in both systems, low-energy AE was mostly generated in the vicinity of matrix cracks. In LFC specimens, such AE was likely the result of either independently-occurring interfacial activity or small crack formation/propagation; in HFC specimens, where interfacial phenomena were obstructed by high interfacial properties, low-energy AE likely resulted from stepped matrix crack propagation and early fiber failure. High-energy and ultra-high-energy AE in LFC and HFC specimens primarily occurred at either: (i) stresses near failure, where they were assumed to be the result of near-simultaneous, large quantity fiber failure, and (ii) at earlier stresses, where they were linked to large matrix crack initiation events. In both systems, there was a correlation between high-energy AE and the eventual failure location, suggesting that the generation of high-energy events indicated areas of concern early in the material loading.

Subsequently, the relationship between damage sources and their corresponding AE in these SiC/SiC systems was modeled using insights gained from mechanical testing combined with SEM-AE (Chapter 3). Damage areas accumulated up to the matrix crack saturation (Domain I), and between matrix crack saturation and failure (Domain II), were estimated using a set of boundary conditions. These conditions varied based on whether they considered *only* the AE activity of dominant damage mechanisms (matrix cracking and fiber failure), or considered that dominant mechanisms and simultaneously

occurring non-dominant mechanisms (interfacial debonding and fiber sliding) generated AE. While prior efforts have typically assumed that only the dominant damage mechanisms contribute AE energy, as they have significantly higher strain energy release rates than secondary mechanisms, it was found that secondary mechanisms were also captured in AE. This was based on multiple factors. Foremost, a progression of matrix cracking consistent with domain knowledge (described in Chapter 2) was only found when the AE contributions of non-dominant mechanisms were included. Furthermore, an estimated evolution of fiber breaks consistent with modeling from Curtin [83] was only found when accounting for the AE contribution of fiber sliding. Further work is needed to characterize the AE energy density contributions of non-dominant mechanisms in order to more accurately measure damage accumulation.

Finally, matrix crack opening displacement (COD) as a function of stress was quantified through the in-SEM capture of surface damage accumulation (Chapter 4). First, a modified edge-detection algorithm was created to accurately and efficiently measure CODs at hundreds of positions along the crack length of numerous active matrix cracks, including the failure location. These COD trends were related to key differences in microstructural features and constituent properties between the HFC and LFC systems. Then, the efficacy of models in the literature to represent the experimentally-captured COD behavior was investigated. Two models were first leveraged for this comparison [1, 2]. For these models, various stress conditions and the scenarios of long cracks versus short cracks were used to understand differences between the predicted and experimentally observed behavior. Two driving factors for model accuracy were determined: (i) consideration of the portion of fibers broken prior to rupture; and (ii) measurement of differences between the initial and subsequent rate of crack opening. While models typically do not account for (i), modeling predictions of the portion of the fiber tow broken from Curtin [3] were employed and estimated as a function of the stress. This inclusion

facilitated overlap between modeling predictions and experimentally-measured CODs in both LFC and HFC specimens. In regard to (ii), most models of the COD converge near 0 μm as a function of the applied stress [1] or sum of the stresses [2]. It was observed, especially in the HFC system, that the initial crack opening rate at matrix crack formation was much higher than the continued crack opening. Leveraging a third model from Chateau et al. [4], which separates these two opening rates, demonstrated marked improvement in modeling predictions.

The findings of this dissertation indicate that CMC damage mechanisms and the manner in which they evolve may be more amenable to prediction than previously thought. In the experiments described herein, early cracks formed as a result of preexisting flaws as predicted by [1]; subsequent transverse matrix crack locations were determined by the interactions of key microstructural and constituent features (in-plane matrix content, local stresses, interphase characteristics, etc.) and evolving local damage mechanisms with stress. These conclusions highlight a need to characterize the AE signatures generated by individual damage mechanisms and to create novel multi-modal approaches and statistical frameworks to understand the effects of surface and subsurface architecture on damage. These investigations are described in the following section on Future Work.

5.2 Recommendations for Future Work

Based on the key findings of this dissertation, there are four immediate and significant avenues for future investigations:

- Damage mechanism identification from AE waveforms
- Multi-modal high resolution *in situ* testing combined with AE measurements
- Testing of new and relevant SiC/SiC CMC microstructures and geometries

- Testing of environmental barrier coated SiC/SiC CMCs

5.2.1 Damage Mechanism Identification from AE Waveforms

While the AE approach has been extensively used both in this dissertation and in previous investigations to characterize damage accumulation in CMCs, the full range of its utility remains to be explored. One long-standing hypothesis in the AE community is that AE waveforms contain signal-specific features that can be used to identify the damage mechanism(s) that generated them [109, 110, 111, 112]. In CMCs, this would be analogous to linking an AE event to the matrix crack, interfacial phenomena, or fiber break(s) activity which generated it. Damage mechanism identification from AE waveform data has wide-spanning ramifications for both structural health monitoring and predictive modeling. Such a breakthrough would enable the *in situ* identification of damage sources in CMC components, providing a comprehensive picture of how and where certain kinds of damage accumulate in the CMC architecture. It would also allow for characterization of the relationship between damage accumulation and processing choices, towards improved manufacturing guidelines for CMCs. Damage mechanism identification would also permit researchers to bypass expensive, high-resolution methods such as SEM and XCT [61, 62, 34], and would produce rich datasets that would enable large-scale statistical analyses of the effects of small-scale damage mechanisms in CMC structures.

Assigning a damage mechanism to an AE waveform necessitates pattern identification across many features (i.e. the use of a high-dimensional representation). However, pattern identification is manually intractable and necessitates the use of machine learning, which is capable of finding structure in data sets where objects are described by high-dimensional features.

Preliminary efforts in building an AE-ML framework for damage mechanism identification in CMCs were described in [60]. While there historically has been a lack of discriminating power between the dominant damage modes of matrix cracking and fiber failure in SiC/SiC, researchers have explained this as the result of similar constituent elastic properties. Instead, recent work by Muir et al. [58, 60] rationalizes this issue as due to the AE waveform representation schemes and ML algorithm choice of previous AE-ML investigations. Earlier AE-ML frameworks often incorporated waveform representations in the time domain, though it was recently shown in [58] that when waveforms from SiC/SiC CMCs were encoded with time domain features [70], conventional frameworks assigned labels based on stochastic waveform distortions rather than the source damage mechanism. Furthermore, the majority of previous ML frameworks used k-means for clustering [113, 23, 114]. However, k-means can only find isotropic clusters, and for this reason is often outperformed by other algorithms [115, 59]. Rather, Muir et al. demonstrated that for SiC/SiC minicomposites, dominant damage mechanisms can be discriminated by using salient frequency-based representations combined with more versatile clustering algorithms [60]. This investigation marks a new path forward in the AE-ML space towards characterizing damage accumulation in more complex SiC/SiC geometries and testing conditions.

5.2.2 Advanced Multi-Modal High Resolution *in situ* Testing

Previous investigations of the damage evolution in CMCs were typically performed *ex situ* or at a free surface [22, 31, 21, 48]. *Ex situ* investigations have limited utility for drawing conclusions regarding the relationships between damage accumulation and CMC microstructure. Studies at free surfaces do not necessarily represent bulk behavior; the boundary conditions, and thereby the mechanical response of the free surface (plane

strain), differ from the response in the bulk (plane stress). For these reasons, more recent investigations use methods such as XCT to provide large fields of view in the material bulk and image damage as it occurs [34, 62, 116, 117]. However, XCT is limited by spatial resolution issues, as the typical voxel size is $\sim$0.65 μm^3. In contrast, crack opening displacements COD of matrix cracks in laminate CMCs can easily fall below 0.4 μm in plane strain conditions [22, 21]. These cracks are expected to be even smaller when the crack is present in the material bulk.

For the purposes of advancing findings through XCT methods, secondary characterization methods such as AE are well-suited. Using a multi-modal approach combining XCT and AE [34, 62], it is possible to detect damage initially below the resolution limitations of XCT, identify its location in the bulk by AE, and subsequently capture its evolution by XCT. The AE-XCT method [34, 62] could additionally leverage the AE-ML framework discussed in the previous subsection. On its own, AE cannot identify *and* verify source damage mechanisms. It is also possible that when damage mechanisms such as fiber breaks and interfacial phenomena occur and are captured as AE, they occur at a scale that is not initially identifiable via XCT. As such, *in situ* AE-XCT experiments will serve two purposes. They will: (i) validate and improve the developed AE-ML framework and (ii) produce high-fidelity datasets at room temperature that are necessary to quantify the effects of microstructural stress concentrations on early fiber breaks. These experiments will comprise the foundation for an analogous testing framework at elevated temperatures [116], towards understanding the effects of thermo-mechanical loading conditions on damage accumulation in SiC/SiC.

5.2.3 Testing of New SiC/SiC Microstructures and Geometries

The AE-SEM framework developed and utilized in this dissertation is extensible to the study of new SiC/SiC microstructures. Additional SiC/SiC microstructures are necessary for further investigation, given that the HFC system does not reflect standard constituent parameters for SiC/SiC CMCs. The study of new minicomposite microstructures will enable a more refined understanding of the relationships between processing, microstructure, and variations in how damage initiates and accumulates. There are currently specimens of two intermediate SiC/SiC minicomposite systems, whose constituent volume fractions exist between the LFC and HFC parameters. For these specimens, one of two quantities of additional CVI SiC matrix were deposited onto HFC minicomposites to reduce the volume fraction contribution of the interphase and fibers. Performing additional in-SEM tensile testing on these specimens will enable new characterization of the crack opening displacement, crack density evolution and matrix fragment length evolution, as well as enable comparative measurements of the interfacial parameters. Potential variations between these intermediate systems and the LFC and HFC specimens studied in this dissertation will enable new insights regarding the evolving role of the interphase (by considering changes in volume contribution, thickness, and interfacial parameters) on damage. Such insights will be useful for improving modeling efforts of damage accumulation in unidirectional SiC/SiC CMCs.

5.2.4 Testing of EB-Coated Minicomposites

SiC/SiC CMCs exhibit excellent oxidation resistance in dry oxygen atmospheres by forming a protective silica layer. However, in the presence of steam (a typical reaction product during combustion) or other corrosive species (such as calcium, magnesium, and alumino-silicate, termed CMAS), this protective silica layer experiences accelerated

degradation and compromises the structural integrity of the material. To combat the exacerbated corrosion observed in typical service conditions, environmental barrier coatings (EBCs) were developed [118]. As is the case for CMC systems, there are a number of suitable materials considered EBCs, with continued exploration for new, performance-optimized EBCs underway.

As an extension of the investigations described in this dissertation, future work will characterize the AE waveforms from damage in EB-coated SiC/SiC minicomposites. Based on recent work by Muir et al. [58, 59, 60] which shows the potential for discriminating between dominant damage modes in SiC/SiC minicomposites, an expanded AE-ML framework which can discriminate cracking of the EBC based on frequency characteristics would have ramifications in structural health monitoring of EB-coated CMCs under in-operando conditions.

Through preliminary in-SEM mechanical testing of an EB-coated LFC SiC/SiC minicomposite, it was observed that cracking of the EBC typically occurs at loads prior to major matrix cracking. AE monitoring during this experiment (using S9225 sensors) also captured a much smaller quantity of AE as compared to the bare specimen (<30% of the AE produced by LFC specimens). One possibility is that this is an artifact of the experimental configuration, where cracking of the EBC in conjunction with AE sensors placed without direct contact to the SiC material inhibits underlying CMC damage sources from being captured by AE. Recent work by Guel et al. [72] showed that AE transducers with overlapping broadband frequency ranges vary in sensitivity to certain frequencies. As such, the AE data acquired using a single sensor type may be blind to certain frequency characteristics (and thereby, a portion of the total energy) of the originating damage sources. With increased waveform attenuation through the EBC, if damage sources present with energies below the sensitivity threshold of the sensors, sensors may not trigger. This issue can be alleviated by use of AE transducers with increased

ranges of broadband frequencies, or in a similar to Guel et al. [72], wherein two sensor types with varying frequency sensitivities are used to assess the damage accumulation for clustering purposes. An interesting possibility is that the source of this reduced AE quantity in EB-coated minicomposites is due to changes to the nature of damage evolution because of the EBC. For instance, the crack density in the EBC (<1 crack/mm) is significantly lower than that in uncoated LFC specimens (Figure 2.13) at rupture, as shown in Figure 5.1. In addition, the matrix crack density in the EB-coated specimen near the rupture zone *also* appears to be lower than the matrix cracking density in the uncoated specimen. Though further experiments are needed, the possibility exists that the EBC reduces how much damage activity accumulates in the CMC prior to rupture, given that the coated specimen failed at similar loads to the uncoated LFC specimens.

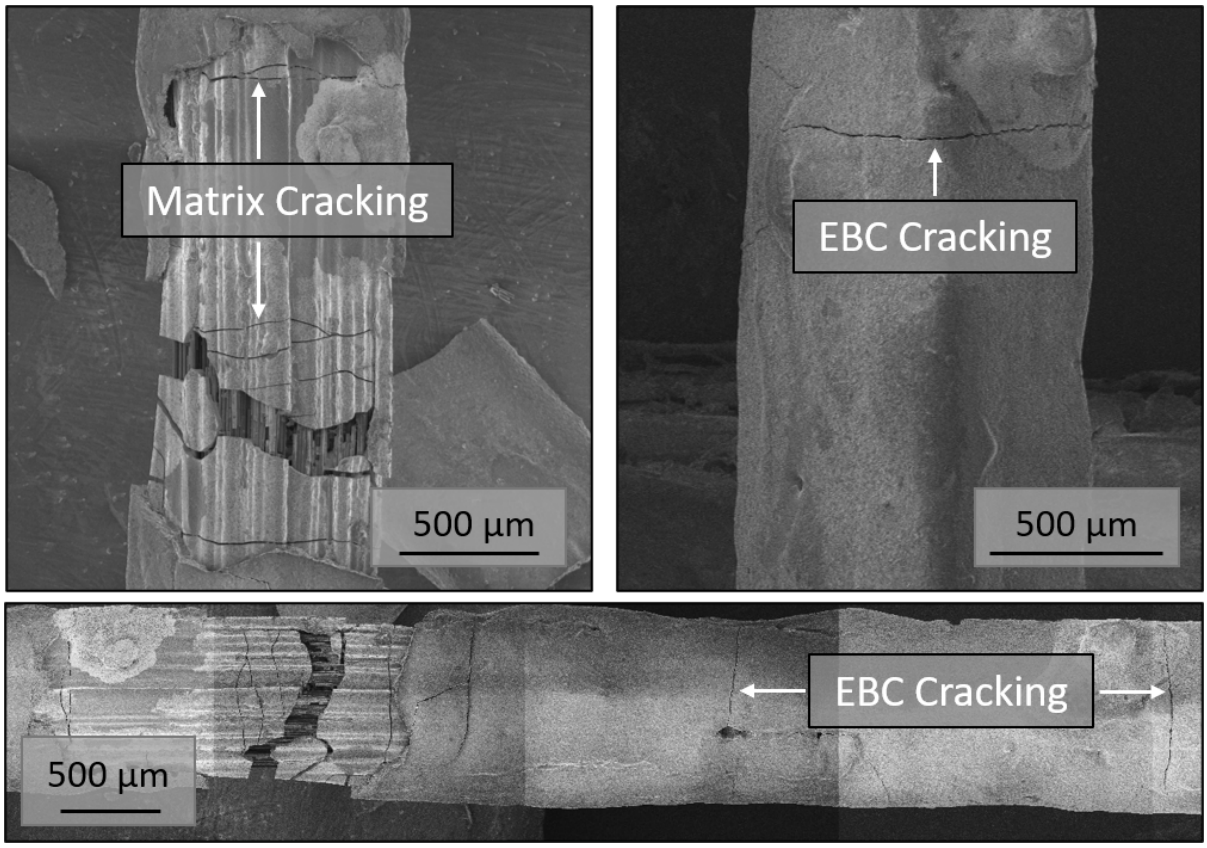

Figure 5.1: Cracking in an EB-coated LFC minicomposite showing: **top left** matrix cracking in the rupture zone at failure, **top right** cracking in the EBC, and **bottom** variation in crack density between the EBC and SiC matrix.

Bibliography

[1] B. N. Marshall, D. B.; Cox and A. Evans, *The Mechanics of Matrix Cracking in Brittle-Matrix Fiber Composites*, *Acta Materialia* **33** (1985), no. 11 2013–2021.

[2] C. P. Yang and F. Jia, *Crack opening model for unidirectional ceramic matrix composites at elevated temperature*, *Ceramics International* **44** (oct, 2018) 17167–17173.

[3] W. A. Curtin, *Theory of Mechanical Properties of Ceramic-Matrix Composites*, *Journal of the American Ceramic Society* **74** (nov, 1991) 2837–2845.

[4] C. Chateau, L. Gélébart, M. Bornert, J. Crépin, D. Caldemaison, and C. Sauder, *Modeling of Damage in Unidirectional Ceramic Matrix Composites and Multi-Scale Experimental Validation on Third Generation SiC/SiC Minicomposites*, *Journal of the Mechanics and Physics of Solids* **63** (2014), no. 1 298–319.

[5] A. Almansour, E. Maillet, S. Ramasamy, and G. N. Morscher, *Effect of Fiber Content on Single Tow SiC Minicomposite Mechanical and Damage Properties using Acoustic Emission*, *Journal of the European Ceramic Society* **35** (2015), no. 13 3389–3399.

[6] F. W. Zok, *Ceramic-matrix composites enable revolutionary gains in turbine engine efficiency*, *Journal of the American Ceramic Society* **95** (2016), no. 5 22–28.

[7] G. N. Morscher, *Fiber-Reinforced Ceramic Matrix Composites for Aero Engines*, 2010.

[8] M. C. Halbig, M. H. Jaskowiak, J. D. Kiser, and D. Zhu, *Evaluation of ceramic matrix composite technology for aircraft turbine engine applications*, *51st AIAA Aerospace Sciences Meeting including the New Horizons Forum and Aerospace Exposition 2013* (2013).

[9] J. Steibel, *Ceramic matrix composites taking flight at GE Aviation*, *American Ceramic Society Bulletin* **98** (2019), no. 3 30–33.

[10] W. E. Lee, M. Gilbert, S. T. Murphy, and R. W. Grimes, *Opportunities for advanced ceramics and composites in the nuclear sector*, *Journal of the American Ceramic Society* **96** (2013), no. 7 2005–2030.

[11] W. Krenkel, ed., *Ceramic Matrix Composites: Fiber Reinforced Ceramics and Their Applications*. Wiley, 2008.

[12] N. P. Bansal and J. Lamon, *Ceramic matrix composites: materials, modeling and technology*. John Wiley & Sons, nov, 2014.

[13] A. Evans and D. Marshall, *The Mechanical Behavior of Ceramic Matrix Composites*, in *Proceedings of The 7th International Conference On Fracture (ICF7)*, pp. 3593–3641, Pergamon, jan, 1989.

[14] J.-M. Domergue, E. Vagaggini, and A. G. Evans, *Relationships between Hysteresis Measurements and the Constituent Properties of Ceramic Matrix Composites: II, Experimental Studies on Unidirectional Materials*, *Journal of the American Ceramic Society* **78** (oct, 1995) 2721–2731.

[15] R. J. Kerans, R. Hay, N. J. Pagano, and T. A. Parthasarathy, *Role of the Fiber-Matrix Interface in Ceramic Composites*, *American Ceramic Society Bulletin* **68** (1989), no. 2 429–442.

[16] J. W. Hutchinson and H. M. Jensen, *Models of fiber debonding and pullout in brittle composites with friction*, sep, 1990.

[17] D. S. Beyerle, S. M. Spearing, F. W. Zok, and A. G. Evans, *Damage and Failure in Unidirectional Ceramic-Matrix Composites*, *Journal of the American Ceramic Society* **75** (1992), no. 10 2719–2725.

[18] J. Lamon, *A Micromechanics-Based Approach to the Mechanical Behavior of Brittle-Matrix Composites*, *Composites Science and Technology* **61** (2001), no. 15 2259–2272.

[19] J. Aveston and A. Kelly, *Theory of Multiple Fractures of Fibrous Composites*, *Journal of Materials Science* **8** (1973), no. 3 352–362.

[20] R. Davidge, *The Mechanical Properties and Fracture Behaviour of Ceramic-Matrix Composites (CMC) Reinforced With Continuous Fibres*, *Composite Materials Series* **6** (jan, 1989) 547–569.

[21] J. Tracy, S. Daly, and K. Sevener, *Multiscale Damage Characterization in Continuous Fiber Ceramic Matrix Composites using Digital Image Correlation*, *Journal of Materials Science* **50** (2015), no. 15 5286–5299.

[22] K. M. Sevener, J. M. Tracy, Z. Chen, J. D. Kiser, and S. Daly, *Crack Opening Behavior in Ceramic Matrix Composites*, *Journal of the American Ceramic Society* **100** (2017), no. 10 4734–4747, [0608246v3].

[23] E. Maillet, N. Godin, M. R'Mili, P. Reynaud, G. Fantozzi, and J. Lamon, *Damage monitoring and identification in SiC/SiC minicomposites using combined acousto-ultrasonics and acoustic emission*, *Composites Part A: Applied Science and Manufacturing* **57** (2014) 8–15.

[24] C. Chateau, L. Gélébart, M. Bornert, J. Crépin, D. Caldemaison, E. Boller, C. Sauder, M. Langer, W. Ludwig, J. Crepin, D. Caldemaison, E. Boller, C. Sauder, M. Langer, and W. Ludwig, *Experimental characterisation of damage in SiC/SiC minicomposites*, *EPJ Web of Conferences* **6** (2010).

[25] C. Chateau, L. Gélébart, M. Bornert, J. Crépin, E. Boller, C. Sauder, and W. Ludwig, *In Situ X-Ray Microtomography Characterization of Damage in SiC_f/SiC Minicomposites*, *Composites Science and Technology* **71** (apr, 2011) 916–924.

[26] J. Aveston, G. Cooper, and A. Kelly, *The Properties of Fiber Composites: Single and Multiple Fracture*, in *Proceedings of the The properties of the fibre composites*, pp. 15–26, 1971.

[27] B. B. Budiansky, J. W. Hutchinson, and A. G. Evans, *Matrix Fracture in Fiber-Reinforced Ceramics*, *Journal of the Mechanics and Physics of Solids* **34** (jan, 1986) 167–189.

[28] W. A. Curtin, B. K. Ahn, and N. Takeda, *Modeling brittle and tough stress-strain behavior in unidirectional ceramic matrix composites*, *Acta Materialia* **46** (1998), no. 10 3409–3420.

[29] B. F. Sorenson and R. Talreja, *Analysis of Damage in a Ceramic Matrix Composite*, *International Journal of Damage Mechanics* **2** (1993), no. 3 246–271.

[30] W. Curtin, *Stress–Strain Behavior of Brittle Matrix Composites*, *Comprehensive Composite Materials* (2000) 47–76.

[31] J. Tracy and S. Daly, *Statistical Analysis of the Influence of Microstructure on Damage in Fibrous Ceramic Matrix Composites*, *International Journal of Applied Ceramic Technology* **14** (2017), no. 3 354–366, [NIHMS150003].

[32] T. A. Parthasarathy, B. Cox, O. Sudre, C. Przybyla, and M. K. Cinibulk, *Modeling Environmentally Induced Property Degradation of SiC/BN/SiC Ceramic Matrix Composites*, *Journal of the American Ceramic Society* **101** (mar, 2018) 973–997.

[33] L. Saucedo-Mora and T. J. Marrow, *Multi-Scale Damage Modelling in a Ceramic Matrix Composite using a Finite-Element Microstructure Meshfree Methodology*, *Philosophical transactions. Series A, Mathematical, physical, and engineering sciences* **374** (jul, 2016) 20150276.

[34] E. Maillet, A. Singhal, A. Hilmas, Y. Gao, Y. Zhou, G. Henson, and G. Wilson, *Combining in-situ synchrotron X-ray microtomography and acoustic emission to characterize damage evolution in ceramic matrix composites*, *Journal of the European Ceramic Society* **39** (oct, 2019) 3546–3556.

[35] A. Shojaei, G. Li, J. Fish, and P. Tan, *Multi-Scale Constitutive Modeling of Ceramic Matrix Composites by Continuum Damage Mechanics*, *International Journal of Solids and Structures* **51** (nov, 2014) 4068–4081.

[36] L. Borkowski and A. Chattopadhyay, *Multiscale Model of Woven Ceramic Matrix Composites Considering Manufacturing Induced Damage*, *Composite Structures* **126** (aug, 2015) 62–71.

[37] J. Kim and P. K. Liaw, *The Nondestructive Evaluation of Advanced Ceramics and Ceramic-Matrix Composites*, *Journal of Materials* **50** (nov, 1998).

[38] C. Smith and A. Gyekenyesi, *Detecting cracks in ceramic matrix composites by electrical resistance*, *Nondestructive Characterization for Composite Materials, Aerospace Engineering, Civil Infrastructure, and Homeland Security 2011* **7983** (2011) 79830N.

[39] M. R. Gorman and S. M. Ziola, *Plate waves produced by transverse matrix cracking*, *Ultrasonics* **29** (1991), no. 3 245–251.

[40] B. Audoin and S. Baste, *Ultrasonic evaluation of stiffness tensor changes and associated anisotropic damage in a ceramic matrix composite*, .

[41] G. N. Morscher, *Modal Acoustic Emission of Damage Accumulation in Woven SiC/SiC at Elevated Temperatures*, in *Review of Progress in Quantitative Nondestructive Evaluation* (D. Thompson and D. Chimenti, eds.), vol. 59, pp. 419–426. Springer US, Boston, MA, 19 ed., 1999.

[42] E. Maillet, C. Baker, G. N. Morscher, V. V. Pujar, and J. R. Lemanski, *Feasibility and limitations of damage identification in composite materials using acoustic emission*, *Composites Part A: Applied Science and Manufacturing* **75** (aug, 2015) 77–83.

[43] G. N. Morscher, J. Hurst, and D. Brewer, *Intermediate-Temperature Stress Rupture of a Woven Hi-Nicalon, BN-Interphase , SiC-Matrix Composite in Air*, *Journal of the American Ceramic Society* **83** (2000), no. 6 1441–1449.

[44] E. Maillet, N. Godin, M. R'Mili, P. Reynaud, J. Lamon, and G. Fantozzi, *Analysis of Acoustic Emission Energy Release during Static Fatigue Tests at Intermediate Temperatures on Ceramic Matrix Composites: Towards Rupture Time Prediction*, *Composites Science and Technology* **72** (2012), no. 9 1001–1007.

[45] S. Momon, M. Moevus, N. Godin, M. R'Mili, P. Reynaud, G. Fantozzi, and G. Fayolle, *Acoustic Emission and Lifetime Prediction during Static Fatigue Tests on Ceramic-Matrix-Composite at High Temperature under Air*, *Composites Part A: Applied Science and Manufacturing* **41** (jul, 2010) 913–918.

[46] G. N. Morscher, *Modal acoustic emission of damage accumulation in a woven SiC/SiC composite*, *Composites Science and Technology* **59** (1999), no. 5 687–697.

[47] J. Martıinez-Fernandez and G. Morscher, *Room and Elevated Temperature Tensile Properties of Single Tow Hi-Nicalon, Carbon Interphase, CVI SiC Matrix Minicomposites*, *Journal of the European Ceramic Society* **20** (dec, 2000) 2627–2636.

[48] T. Whitlow, E. Jones, and C. Przybyla, *In-situ damage monitoring of a SiC/SiC ceramic matrix composite using acoustic emission and digital image correlation*, *Composite Structures* **158** (dec, 2016) 245–251.

[49] G. N. Morscher, H. M. Yun, and J. A. DiCarlo, *Matrix Cracking in 3D Orthogonal Melt-Infiltrated SiC/SiC Composites with Various Z-Fiber Types*, *Journal of the American Ceramic Society* **88** (dec, 2004) 146–153.

[50] F. Breede, D. Koch, E. Maillet, and G. N. Morscher, *Modal acoustic emission of damage accumulation in C/C-SiC composites with different fiber architectures*, *Ceramics International* **41** (2015).

[51] G. N. Morscher, H. M. Yun, and J. A. DiCarlo, *In-Plane Cracking Behavior and Ultimate Strength for 2D Woven and Braided Melt-Infiltrated SiC/SiC Composites Tensile Loaded in Off-Axis Fiber Directions*, *Journal of the American Ceramic Society* **90** (oct, 2007) 3185–3193.

[52] R. Y. Kim and N. J. Pagano, *Crack Initiation in Unidirectional Brittle-Matrix Composites*, *Journal of the American Ceramic Society* **74** (may, 1991) 1082–1090.

[53] J.-J. Luo, S.-C. Wooh, and I. M. Daniel, *Acoustic Emission Study of Failure Mechanisms in Ceramic Matrix Composite under Longitudinal Tensile Loading*, *Journal of Composite Materials* **29** (oct, 1995) 1946–1961.

[54] M. Surgeon, E. Vanswijgenhoven, M. Wevers, and O. Van Der Biest, *Acoustic emission during tensile testing of SiC-fibre-reinforced BMAS glass-ceramic composites*, *Composites Part A: Applied Science and Manufacturing* **28** (jan, 1997) 473–480.

[55] M. Sause, A. Gribov, A. Unwin, and S. Horn, *Pattern Recognition Approach to Identify Natural Clusters of Acoustic Emission Signals*, *Pattern Recognition Letters* **33** (jan, 2012) 17–23.

[56] R. Gutkin, C. Green, S. Vangrattanachai, S. Pinho, P. Robinson, and P. Curtis, *On Acoustic Emission for Failure Investigation in CFRP: Pattern Recognition and Peak Frequency Analyses*, *Mechanical Systems and Signal Processing* **25** (may, 2011) 1393–1407.

[57] E. Maillet, C. Baker, G. N. Morscher, V. V. Pujar, and J. R. Lemanski, *Feasibility and limitations of damage identification in composite materials using acoustic emission*, *Composites Part A: Applied Science and Manufacturing* **75** (aug, 2015) 77–83.

[58] C. Muir, B. Swaminathan, N. Mccarthy, A. Musaffar, A. S. Almansour, M. J. Presby, C. E. Smith, K. Sevener, J. Kiser, and S. Daly, *Large scale statistical methods to evaluate damage accumulation in SiC / SiC composites*, in *SEM Annual 2020 Virtual XIV International Congress*, 2020.

[59] C. Muir, B. Swaminathan, A. S. Almansour, K. Sevener, C. Smith, M. Presby, J. D. Kiser, T. M. Pollock, and S. Daly, *Damage Mechanism Identification in Composites via Machine Learning and Acoustic Emission*, *npj Computational Materials* (June, 2021).

[60] C. Muir, B. Swaminathan, K. Fields, A. S. Almansour, K. Sevener, C. Smith, M. Presby, J. D. Kiser, T. M. Pollock, and S. Daly, *Machine learning for acoustic emission: damage mechanism identification in ceramic matrix composites*, *In review* (2021).

[61] B. Swaminathan, N. R. McCarthy, A. S. Almansour, K. Sevener, T. M. Pollock, J. D. Kiser, and S. Daly, *Microscale Characterization of Damage Accumulation in CMCs*, *Journal of the European Ceramic Society* (2020).

[62] A. M. Hilmas, K. M. Sevener, and J. W. Halloran, *Damage evolution in SiC/SiC unidirectional composites by X-ray tomography*, *Journal of the American Ceramic Society* **103** (2020), no. 5 3436–3447.

[63] G. N. Morscher, G. Ojard, R. Miller, Y. Gowayed, U. Santhosh, J. Ahmad, and R. John, *Tensile creep and fatigue of Sylramic-iBN melt-infiltrated SiC matrix composites: Retained properties, damage development, and failure mechanisms*, *Composites Science and Technology* **68** (dec, 2008) 3305–3313.

[64] G. Grathwohl, A. Hähnel, B. Meier, E. Pippel, G. Richter, and J. Woltersdorf, *Fibre-Reinforced SiC-Matrix Composites: Microstructure, Interfaces and Mechanical Properties*, *Journal of the European Ceramic Society* **10** (jan, 1992) 1–12.

[65] J. Tracy, A. Waas, and S. Daly, *A new experimental approach for in situ damage assessment in fibrous ceramic matrix composites at high temperature*, *Journal of the American Ceramic Society* **98** (2015), no. 6 1898–1906.

[66] D. B. Marshall and A. G. Evans, *Failure Mechanisms in Ceramic-Fiber / Ceramic-Matrix Composites*, *Journal of the American Ceramic Society* **68** (1985), no. 5 225–231.

[67] G. N. Morscher and N. Godin, *Use of Acoustic Emission for Ceramic Matrix Composites*, in *Ceramic Matrix Composites: Materials, Modeling, and Technology* (N. P. Bansal and J. Lamon, eds.), ch. IV: Nondes, pp. 571–590. John Wiley & Sons, Inc., 1 ed., 2014.

[68] D. G. Aggelis, K. G. Dassios, E. Z. Kordatos, and T. E. Matikas, *Damage accumulation in cyclically-loaded glass-ceramic matrix composites monitored by acoustic emission.*, *TheScientificWorldJournal* **2013** (nov, 2013) 869467.

[69] E. Racle, N. Godin, P. Reynaud, and G. Fantozzi, *Fatigue Lifetime of Ceramic Matrix Composites at Intermediate Temperature by Acoustic Emission.*, *Materials (Basel, Switzerland)* **10** (jun, 2017).

[70] M. Moevus, N. Godin, M. R'Mili, D. Rouby, P. Reynaud, G. Fantozzi, and G. Farizy, *Analysis of damage mechanisms and associated acoustic emission in two SiC f /[Si – B – C] composites exhibiting different tensile behaviours . Part II : Unsupervised acoustic emission data clustering*, *Composites Science and Technology* **68** (may, 2008) 1258–1265.

[71] N. Godin, P. Reynaud, and G. Fantozzi, *Challenges and limitations in the identification of acoustic emission signature of damage mechanisms in composites materials*, *Applied Sciences (Switzerland)* **8** (2018), no. 8.

[72] N. Guel, Z. Hamam, N. Godin, P. Reynaud, O. Caty, F. Bouillon, and A. Paillassa, *Data merging of ae sensors with different frequency resolution for the detection and identification of damage in oxide-based ceramic matrix composites*, *Materials* **13** (2020), no. 20 1–22.

[73] J. H. Weaver, J. Rannou, M. A. Mattoni, and F. W. Zok, *Interface Properties in a Porous-Matrix Oxide Composite*, *Journal of the American Ceramic Society* **89** (2006), no. 9 2869–2873.

[74] D. B. Marshall and W. C. Oliver, *Measurement of Interfacial Mechanical Properties in Fiber-Reinforced Ceramic Composites*, *Journal of the American Ceramic Society* **70** (aug, 1987) 542–548.

[75] E. Callaway, P. Christodoulou, and F. Zok, *Deformation, rupture and sliding of fiber coatings in ceramic composites*, *Journal of the Mechanics and Physics of Solids* **132** (nov, 2019).

[76] J. Lamon, F. Rebillat, and A. G. Evans, *Microcomposite Test Procedure for Evaluating the Interface Properties of Ceramic Matrix Composites*, *Journal of the American Ceramic Society* **78** (feb, 1995) 401–405.

[77] J. Douglas Kiser, K. E. David, C. Davies, R. Andrulonis, and C. Ashforth, *Updating composite materials handbook-17 volume 5— ceramic matrix composites*, in *Ceramic Transactions*, vol. 263, pp. 413–423. SAE Intenational on behalf of CMH-17, a division of Wichita State University, 2018.

[78] K. Ono, *Through-Transmission Characteristics of AE Sensor Couplants*, *J. Acoustic Emission* **34** (2017) 1.

[79] G. N. Morscher and A. L. Gyekenyesi, *The velocity and attenuation of acoustic emission waves in SiC/SiC composites loaded in tension*, *Composites Science and Technology* **62** (2002), no. 9 1171–1180.

[80] M. Sause, *Investigation of pencil-lead breaks as acoustic emission sources*, 2011.

[81] M. Shigeishi, S. Colombo, K. J. Broughton, H. Rutledge, A. J. Batchelor, and M. C. Forde, *Acoustic emission to assess and monitor the integrity of bridges*, *Construction and Building Materials* **15** (feb, 2001) 35–49.

[82] OpenStax College, "Energy in Waves: Intensity."

[83] W. A. Curtin, *Exact Theory of Fibre Fragmentation in a Single-Filament Composite*, *Journal of Materials Science* **26** (1991), no. 19 5239–5253.

[84] J. M. Neumeister, *A Constitutive Law for Continuous Fiber Reinforced Brittle Matrix Composites with Fiber Fragmentation and Stress Recovery*, *Journal of the Mechanics and Physics of Solids* **41** (aug, 1993) 1383–1404.

[85] B. Budiansky, A. G. Evans, and J. W. Hutchinson, *Fiber-Matrix Debonding Effects on Cracking in Aligned Fiber Ceramic Composites*, *International Journal of Solids and Structures* **32** (1994) 315–328.

[86] S. Bertrand, P. Forio, R. Pailler, and J. Lamon, *Hi-Nicalon/SiC Minicomposites with (Pyrocarbon/SiC)$_n$ Nanoscale Multilayered Interphases*, *Journal of the American Ceramic Society* **82** (sep, 1999) 2465–2473.

[87] N. Lissart and J. Lamon, *Damage and Failure in Ceramic Matrix Minicomposites: Experimental Study and Model*, *Acta Materialia* **45** (mar, 1997) 1025–1044.

[88] G. N. Morscher, *Modeling the elastic modulus of 2D woven CVI SiC composites*, *Composites Science and Technology* **66** (dec, 2006) 2804–2814.

[89] E. B. Callaway and F. W. Zok, *Tensile response of unidirectional ceramic minicomposites*, *Journal of the Mechanics and Physics of Solids* **138** (2020).

[90] G. N. Morscher and J. D. Cawley, *Intermediate temperature strength degradation in SiC/SiC composites*, *Journal of the European Ceramic Society* **22** (jan, 2002) 2777–2787.

[91] W. A. Curtin, *Fiber pull-out and strain localization in ceramic matrix composites*, *Journal of the Mechanics and Physics of Solids* **41** (1993), no. 1 35–53.

[92] R. S. Goldberg, A. S. Almansour, and R. M. Sullivan, "Analytical Simulation of Effects of Local Mechanisms on Tensile Response of Ceramic Matrix Minicomposites."

[93] A. Chulya, J. P. Gyekenyesi, and R. T. Bhatt, *Mechanical Behavior of Fiber Reinforced SiC/RBSN Ceramic Matrix Composites: Theory and Experiment*, in *36th International Gas Turbine and Aeroengine Congress and Exposition*, 1991.

[94] C. Sauder, A. Brusson, and J. Lamon, *Influence of Interface Characteristics on the Mechanical Properties of Hi-Nicalon Type-S or Tyranno-SA3 Fiber-Reinforced SiC/SiC Minicomposites*, *International Journal of Applied Ceramic Technology* **7** (feb, 2010) 291–303.

[95] S. E. Hamdi, A. Le Duff, L. Simon, G. Plantier, A. Sourice, and M. Feuilloy, *Acoustic emission pattern recognition approach based on Hilbert-Huang transform for structural health monitoring in polymer-composite materials*, *Applied Acoustics* **74** (2013), no. 5 746–757.

[96] S. Momon, N. Godin, P. Reynaud, M. R'Mili, and G. Fantozzi, *Unsupervised and supervised classification of AE data collected during fatigue test on CMC at high temperature*, *Composites Part A: Applied Science and Manufacturing* **43** (2012), no. 2 254–260.

[97] S. Mazerat and R. Pailler, *Dataset on fractographic analysis of various SiC-based fibers*, *Data in Brief* **34** 106676.

[98] E. B. Callaway and F. W. Zok, *Strengths of ceramic fiber bundles: Theory and practice*, *Journal of the American Ceramic Society* **100** (2017), no. 11 5306–5317.

[99] J. Lamon, B. Thommeret, and C. Percevault, *Probabilistic-statistical approach to matrix damage and stress–strain behavior of 2-D woven SiC/SiC ceramic matrix composites*, *Journal of the European Ceramic Society* **18** (nov, 1998) 1797–1808.

[100] H. Serizawa, C. A. Lewinsohn, G. E. Youngblood, R. H. Jones, D. E. Johnston, and A. Kohyama, *Evaluation of advanced SiC fibers for reinforcement of CMC*, .

[101] S. Mazerat and R. Pailler, *Statistical data for the tensile properties and static fatigue of sic-based bundles*, *Data in Brief* **32** (oct, 2020) 106166.

[102] E. Maillet, N. Godin, M. R'Mili, P. Reynaud, G. Fantozzi, J. Lamon, M. R'Mili, P. Reynaud, G. Fantozzi, and J. Lamon, *Real-time evaluation of energy attenuation: A novel approach to acoustic emission analysis for damage monitoring of ceramic matrix composites*, *Journal of the European Ceramic Society* **34** (jul, 2014) 1673–1679.

[103] I. Abdel-Qader, O. Abudayyeh, and M. E. Kelly, *Analysis of Edge-Detection Techniques for Crack Identification in Bridges*, *Journal of Computing in Civil Engineering* **17** (oct, 2003) 255–263.

[104] A. G. Flesia, G. Ames, G. Bergues, L. C. Ciii, U. Regional, C. Córdoba, and C. Schurrer, *Sub-Pixel Straight Lines Detection for Measuring through Machine Vision*, in *IEEE International Instrumentation and Measurement Technology Conference*, 2014.

[105] J. C. Bezdek and N. R. Pal, *Some new indexes of cluster validity*, *IEEE Transactions on Systems, Man, and Cybernetics, Part B: Cybernetics* **28** (1998), no. 3 301–315.

[106] M. Y. He, A. G. Evans, and J. W. Hutchinson, *Crack deflection at an interface between dissimilar elastic materials: Role of residual stresses*, *International Journal of Solids and Structures* **31** (dec, 1994) 3443–3455.

[107] Q. Cai, D. Scullion, W. Gan, A. Falin, S. Zhang, K. Watanabe, T. Taniguchi, Y. Chen, E. J. Santos, and L. H. Li, *High thermal conductivity of high-quality monolayer boron nitride and its thermal expansion*, *Science Advances* **5** (jun, 2019) eaav0129.

[108] D. B. Marshall, *Analysis of fiber debonding and sliding experiments in brittle matrix composites*, *Acta Metallurgica Et Materialia* **40** (mar, 1992) 427–441.

[109] R. K. Elsley and L. J. Graham, *Pattern Recognition In Acoustic Emission Experiments*, in *Pattern Recognition and Acoustical Imaging*, vol. 0768, p. 285, 1987.

[110] P. J. de Groot, P. A. Wijnen, and R. B. Janssen, *Real-time frequency determination of acoustic emission for different fracture mechanisms in carbon/epoxy composites*, *Composites Science and Technology* **55** (1995), no. 4 405–412.

[111] M. Johnson and P. Gudmundson, *Broad-band transient recording and characterization of acoustic emission events in composite laminates*, *Composites Science and Technology* **60** (2000), no. 15 2803–2818.

[112] M. G. Sause, A. Gribov, A. R. Unwin, and S. Horn, *Pattern recognition approach to identify natural clusters of acoustic emission signals*, *Pattern Recognition Letters* **33** (2012), no. 1 17–23.

[113] V. Kostopoulos, T. Loutas, and K. Dassios, *Fracture behavior and damage mechanisms identification of SiC/glass ceramic composites using AE monitoring*, *Composites Science and Technology* **67** (2007), no. 7-8 1740–1746.

[114] S. K. Chelliah, P. Parameswaran, S. Ramasamy, A. Vellayaraj, and S. Subramanian, *Optimization of acoustic emission parameters to discriminate failure modes in glass–epoxy composite laminates using pattern recognition*, *Structural Health Monitoring* **18** (jul, 2019) 1253–1267.

[115] M. Z. Rodriguez, C. H. Comin, D. Casanova, O. M. Bruno, D. R. Amancio, L. d. F. Costa, and F. A. Rodrigues, *Clustering algorithms: A comparative approach*, *PLoS ONE* **14** (jan, 2019) e0210236, [arXiv:1612.0838].

[116] H. A. Bale, A. Haboub, A. A. Macdowell, J. R. Nasiatka, D. Y. Parkinson, B. N. Cox, D. B. Marshall, and R. O. Ritchie, *Real-time quantitative imaging of failure events in materials under load at temperatures above 1,600°C*, *Nature Materials* **12** (jan, 2013) 40–46.

[117] H. S. Barnard, A. A. MacDowell, D. Y. Parkinson, P. Mandal, M. Czabaj, Y. Gao, E. Maillet, B. Blank, N. M. Larson, R. O. Ritchie, B. Gludovatz, C. Acevedo, and D. Liu, *Synchrotron X-ray micro-tomography at the Advanced Light Source: Developments in high-temperature in-situ mechanical testing*, in *Journal of Physics: Conference Series*, vol. 849, p. 012043, Institute of Physics Publishing, jun, 2017.

[118] D. Tejero-Martin, C. Bennett, and T. Hussain, *A review on environmental barrier coatings: History, current state of the art and future developments*, *Journal of the European Ceramic Society* **41** (mar, 2021) 1747–1768, [arXiv:2007.1491].